# CONTOURLET DOMAIN IMAGE MODELING AND ITS APPLICATIONS IN WATERMARKING AND DENOISING

Hamidreza Sadreazami

A Thesis

in

The Department

of

Electrical and Computer Engineering

Presented in Partial Fulfillment of the Requirements

for the Degree of Doctor of Philosophy at

Concordia University

Montreal, Quebec, Canada

April 2016

**CONCORDIA UNIVERSITY**

**SCHOOL OF GRADUATE STUDIES**

This is to certify that the thesis prepared

By: **Hamidreza Sadreazami**

Entitled: **Contourlet Domain Image Modeling and its Applications in Watermarking and Denoising**

and submitted in partial fulfillment of the requirements for the degree of

DOCTOR OF PHILOSOPHY (Electrical & Computer Engineering)

complies with the regulations of the University and meets the accepted standards with respect to originality and quality.

Signed by the final examining committee:

_____ Chair
Dr. A. Krzyzak

_____ External Examiner
Dr. O. A. Basir

_____ External to Program
Dr. T. Fancott

_____ Examiner
Dr. Y. R. Shayan

_____ Examiner
Dr. W. P. Zhu

_____ Thesis Co-Supervisor
Dr. M. O. Ahmad

_____ Thesis Co-Supervisor
Dr. M. N. S. Swamy

Approved by _____
Dr. A. R. Sebak

April 20, 2016 _____
Dr. W. E. Lynch

# ABSTRACT


## Contourlet Domain Image Modeling and its Applications in Watermarking and Denoising

Hamidreza Sadreazami, Ph. D.

Concordia University, 2016.

Statistical image modeling in sparse domain has recently attracted a great deal of research interest. Contourlet transform as a two-dimensional transform with multiscale and multi-directional properties is known to effectively capture the smooth contours and geometrical structures in images. The objective of this thesis is to study the statistical properties of the contourlet coefficients of images and develop statistically-based image denoising and watermarking schemes.

Through an experimental investigation, it is first established that the distributions of the contourlet subband coefficients of natural images are significantly non-Gaussian with heavy-tails and they can be best described by the heavy-tailed statistical distributions, such as the alpha-stable family of distributions. It is shown that the univariate members of this family are capable of accurately fitting the marginal distributions of the empirical data and that the bivariate members can accurately characterize the inter-scale dependencies of the contourlet coefficients of an image.

Based on the modeling results, a new method in image denoising in the contourlet domain is proposed. The Bayesian maximum *a posteriori* and minimum mean absolute

error estimators are developed to determine the noise-free contourlet coefficients of grayscale and color images. Extensive experiments are conducted using a wide variety of images from a number of databases to evaluate the performance of the proposed image denoising scheme and to compare it with that of other existing schemes. It is shown that the proposed denoising scheme based on the alpha-stable distributions outperforms these other methods in terms of the peak signal-to-noise ratio and mean structural similarity index, as well as in terms of visual quality of the denoised images.

The alpha-stable model is also used in developing new multiplicative watermark schemes for grayscale and color images. Closed-form expressions are derived for the log-likelihood-based multiplicative watermark detection algorithm for grayscale images using the univariate and bivariate Cauchy members of the alpha-stable family. A multiplicative multichannel watermark detector is also designed for color images using the multivariate Cauchy distribution. Simulation results demonstrate not only the effectiveness of the proposed image watermarking schemes in terms of the invisibility of the watermark, but also the superiority of the watermark detectors in providing detection rates higher than that of the state-of-the-art schemes even for the watermarked images undergone various kinds of attacks.

# ACKNOWLEDGEMENTS

This thesis is the outcome of a wonderful four-year working experience under the guidance of Dr. M. Omair Ahmad and Dr. M. N. S. Swamy, to whom I wish to express my sincere appreciation and gratitude. Their vision, patience, and enthusiasm have not just fueled this research but also have a lasting influence in my career as a role model.

My deepest gratitude goes to my wife Marzieh for her continued love, unlimited support and inspiration for completing this thesis. Finally, I would like to dedicate this work to my parents, whose constant support and encouragement have really brought me here.

# TABLE OF CONTENTS

**TABLE OF CONTENTS** ..... **vi**

**LIST OF FIGURES** ..... **ix**

**LIST OF TABLES** ..... **xv**

**LIST OF SYMBOLS** ..... **xvii**

**LIST OF ABBRIVIATIONS** ..... **xix**

**CHAPTER 1: Introduction** ..... **1**

1.1 General ..... 1

1.2 A Brief Literature Review on Image Denoising and Watermarking in the Contourlet Domain ..... 4

1.3 Objective and Organization of the Thesis ..... 6

**CHAPTER 2: Contourlet Transform and Statistical Modeling of its Coefficients** ..... **10**

2.1 Introduction ..... 10

2.2 Contourlet Transform ..... 12

2.2.1 Laplacian Pyramid ..... 12

2.2.2 Directional Filter Bank ..... 17

2.2.3 Pyramidal Directional Filter Bank ..... 18

2.3 Statistical Modeling of the Contourlet Coefficients ..... 21

2.3.1 Generalized Gaussian Distribution ..... 24

2.3.2 Alpha-Stable Family of Distributions ..... 25

2.4 Parameter Estimation of the Alpha-Stable Distribution ..... 29

2.4.1 Characteristic Function Method ..... 29

2.4.2 Moments Method ..... 30

2.4.3 Fractional Lower Order Moment Method ..... 31

2.5 Alpha-stable Modeling of the Contourlet Coefficients ..... 32

2.6 Summary ..... 38

**CHAPTER 3: Image Denoising in Contourlet Domain Using the Alpha-Stable Distribution ..... 39**

3.1 Introduction ..... 39

3.2 Denoising Scheme in the Contourlet Domain ..... 42

3.2.1 Bayesian MAP Estimator for Gaussian Noise ..... 47

3.2.2 Bayesian MAP Estimator for Non-Gaussian Noise ..... 50

3.2.3 Bayesian MMAE Estimator ..... 52

3.2.4 Parameter Estimation ..... 54

3.3 Experimental Results ..... 57

3.3.1 Extension to Color Image Denoising ..... 73

3.3 Summary ..... 80

**CHAPTER 4: Despeckling of the Synthetic Aperture Radar Images in Contourlet Domain Using the Alpha-Stable Distribution ..... 81**

4.1 Introduction ..... 81

4.2 Bayesian MAP Estimator ..... 82

4.3 Experimental Results ..... 86

4.4 Summary ..... 89

**CHAPTER 5: Multiplicative Watermark Detection in Contourlet Domain Using the Alpha-Stable Distribution ..... 90**

5.1 Introduction ..... 90

5.2 Watermarking ..... 92

5.2.1 Watermark Embedding ..... 93

5.2.2 Watermark Detection ..... 95

5.2.3 Detector Based on the Univariate Alpha-Stable Distribution ..... 100

5.2.4 Detector Based on the Bivariate Alpha-Stable Distribution ..... 104

5.3 Experimental Results ..... 107

5.4 Summary ..... 117

**CHAPTER 6: Multiplicative Watermark Detector for Color Images in Contourlet Domain ..... 118**

6.1 Introduction ..... 118

6.2 Watermarking Scheme ..... 119

6.3 Experimental Results ..... 126

6.4 Summary ..... 135

**CHAPTER 7: Conclusion ..... 136**

7.1 Concluding Remarks ..... 136

7.2 Contributions ..... 138

7.3 Scope for Future Work ..... 140

**REFERENCES ..... 141**

# List of Figures

Figure 2.1: a) Analysis part of the Laplacian pyramid; the outputs are a coarse approximation and a residual between the original image and the prediction. b) Synthesis part of the Laplacian pyramid .....14

Figure 2.2: Five levels of decomposition using the Laplacian pyramid. In each level, there is a lowpass and a bandpass part. .....15

Figure 2.3: An example of possible frequency partitioning by the contourlet transform. .....17

Figure 2.4: Block diagram of the contourlet filter bank structure. a) Analysis part, b) Synthesis part. .....19

Figure 2.5: Contourlet representation of the *Barbara* image. The original image is first decomposed into two pyramidal levels followed by eight and four directional subbands.....20

Figure 2.6: Histograms of the contourlet coefficients of two finest scales for *Barbara* image. The kurtosis value $k$ shows the degree of the non-Gaussianity for the coefficients of each subband. a) Finest scale and b) Second finest scale.....22

Figure 2.7: Normal probability plot of the *Barbara* image. The empirical data does not follow a straight line showing that the data is not Gaussian. .....23

Figure 2.8: Average kurtosis values of contourlet subband coefficients for various values of the number of subbands $S$ .....23

Figure 2.9: a) PDFs and b) CDFs of $S\alpha S$ distributions for different values of the characteristic exponent $\alpha$ . .....28

Figure 2.10: Log-scale PDFs of empirical data as well as the alpha-stable, Cauchy, GG and Laplacian distributions for two of the test images. a) *Barbara* $\alpha = 0.8$. b) *Baboon* $\alpha = 1.31$. .....35

Figure 2.11: APD curves of the empirical data as well as the alpha-stable, Cauchy, GG and Laplacian distributions for two of the test images. a) *Barbara* and b) *Baboon*. .....37

Figure 3.1: Parent-children relationship for a three-scale contourlet decomposition with eight directions in each scale. .....44

Figure 3.2: (a) Empirical joint child-parent histogram across two scales of the contourlet coefficients for the fourth direction of the *Barbara* image. b) The configuration of the bivariate $S\alpha S$ distribution. .....45

Figure 3.3: Distribution of the contourlet coefficients (vertical axis) conditioned on the corresponding coarser-scale coefficient, i.e., parent coefficient (horizontal axis), in the four directional subbands of the *Barbara* image; A normalized pair of parent and child coefficients is considered.....46

Figure 3.4: Block diagram of the proposed denoising algorithm in the contourlet domain.....56

Figure 3.5: Top-left: original *Boat* image. Top-right: Noisy image with $\sigma$=30. Bottom-left: Denoised using BM3D. Bottom-right: Denoised using the proposed method.....66

Figure 3.6: Top-left: original *Barbara* image. Top-right: Noisy image with $\sigma$=30. Bottom-left: Denoised using BM3D. Bottom-right: Denoised using the proposed method.....67

Figure 3.7: Top-left: original *Lena* image. Top-right: Noisy image with $\sigma_\eta$=30. Bottom-left: Denoised using BM3D. Bottom-right: Denoised using the proposed method. .....68

Figure 3.8: (a) Noisy *Lena* image by the Maxwell noise with σ = 5, (b) Denoised image obtained using BM3D method, RMSE=0:0945, and (c) Denoised image obtained using the proposed method, RMSE = 0.0883.....72

Figure 3.9: Noisy *Lena* image by the Rayleigh noise with σ = 5, (b) Denoised image obtained using BM3D method, RMSE = 0.0051, and (c) Denoised image obtained using the proposed method, RMSE = 0.0023. .....72

Figure 3.10: Contourlet domain decomposition of the RGB channels for color images. Each subband coefficients $X_1$ are highly dependent to the same-oriented subband coefficients of two other channels, namely, $X_2$ and $X_3$. .....73

Figure 3.11: Color image denoising; (a) Cropped noisy *Lena* image with $\sigma$=20, PSNR=18.60 dB as well as the corresponding denoised images obtained using (b) CBM3D, PSNR=31.59 dB and (c) the proposed CT-Tri-$S\alpha S$-MMAE, PSNR=31.33 dB.. .....78

Figure 3.12: Color image denoising; (a) Cropped noisy *Lena* image with $\sigma$=30, PSNR=18.61 dB as well as the corresponding denoised images obtained using (b) CBM3D, PSNR=31.78 dB and (c) the proposed CT-Tri-$S\alpha S$-MMAE, PSNR=31.90 dB. .....78

Figure 3.13: Color image denoising; (a) Cropped noisy *Lena* image with $\sigma$=30, PSNR=18.61 dB as well as the corresponding denoised images obtained

using (b) CBM3D, PSNR=31.61 dB and (c) the proposed CT-Tri-$S\alpha S$-MMAE, PSNR=31.42 dB. .....79

Figure 4.1: Block diagram of the proposed algorithm for speckle reduction.....85

Figure 4.2: (a) *Ajkwa* image. Obtained despeckled images by using various methods, namely, (b) WIN-SAR, (c) NCST, and (d) the proposed method. .....88

Figure 5.1: Block diagram of the watermark embedding procedure.....94

Figure 5.2: Block diagram of the watermark detection procedure.....95

Figure 5.3: ROC curves for the alpha-stable, Cauchy and GG distributions .....103

Figure 5.4: ROC curves for the bivariate alpha-stable (bi-alpha-stable), univariate alpha-stable, bivariate Cauchy (bi-Cauchy), Cauchy and GG distributions, (a)WDR= - 38 dB, (b) WDR= - 40 dB. .....106

Figure 5.5: Original (a-e) and watermarked with WDR = - 40 dB (f-j) images of *Lena* PSNR = 58.42, *Barbara* PSNR = 52.19, *Peppers* PSNR = 60.20, *Airplane* PSNR = 56.85 and *Baboon* PSNR=53.35. No visual difference can be realized.....108

Figure 5.6: ROC curves for contourlet, curvelet, wavelet and dual-tree complex wavelet (DTCW) transforms.....110

Figure 5.7: Theoretical and experimental ROC curves for the bivariate Cauchy and GG detectors .....111

Figure 5.8: Probability of detection for watermarks of varying strength parametrized by the WDR (dB) for various detectors .....111

Figure 5.9: Probability of false alarm for watermarks of varying strength parametrized by WDR (dB) for various detectors .....113

Figure 5.10: ROC curves for various detectors when the AWGN with various standard deviations is added to the watermarked images.....113

Figure 5.11: Detector response for the (a) bivariate alpha-stable, (b) bivariate Cauchy, (c) univariate Cauchy and (d) GG distributions when the *Lena* image is JPEG-compressed with different quality factors varying from 1 to 100, WDR=-38 dB.....115

Figure 5.12: Detector response for the (a) bivariate alpha-stable, (b) bivariate Cauchy, (c) univariate Cauchy and (d) GG distributions when the *Lena* image is under median filtering with windows of size of 3×3, 5×5 and 7×7;WDR = -38 dB.....116

Figure 6.1: (a) Original and (b) watermarked Kodak images, from left to right: *Girl*, *Headlight*, *Window* and *Parrots* with PSNR values 68.08, 64.16, 63.45 and 69.57 dB, respectively.....127

Figure 6.2: Detector response of the proposed watermark detection scheme for some of the test images, namely, (a) *Parrots* (b) *Girl* (c) *Headlight* and (d) *Lena*. .....128

Figure 6.3: The experimental (dashed) and theoretical (solid) ROC curves averaged over a set of color images obtained using the proposed detector .....130

Figure 6.4: ROC curve obtained using the proposed detector (multiplicative and additive) as well as that of the RGB-joint correlator [1], luminance-GG/Cauchy [9] and RGB-MPE [10].....130

Figure 6.5: ROC curves obtained using the proposed detector averaged over a set of color images when the watermarked images are JPEG-compressed with various QFs .....132

Figure 6.6: ROC curves obtained using the proposed detector averaged over a set of color images when Gaussian noise with various $\sigma_\eta$ is added to the watermarked images .....132

Figure 6.7: ROC curves obtained using the proposed detector averaged over a set of color images when the watermarked images are under median filter with different mask sizes.....133

Figure 6.8: ROC curves obtained using the proposed detector averaged over a set of color images when the watermarked images are under Gaussian filter with various mask sizes.....133

Figure 6.9: ROC curves obtained using the proposed detector averaged over a set of color images when the watermarked images are under salt and pepper noise with various probability of noisy pixels. *p* denotes the percentage of corrupted pixels.....134

# List of Tables

Table 2.1: The values of the characteristic exponent $\alpha$, for the contourlet subband coefficients of various test images. Deviation from $\alpha = 2$ reveals the degree of non-Gaussianity. .....34

Table 2.2: Averaged KSD values of the alpha-stable, Cauchy, GG, Laplacian and Levy distributions in modeling the contourlet coefficients over 1000 images, $S_{ij}$ denoting the subband in scale i and direction j. .....36

Table 3.1: PSNR values obtained using denoising methods employing the alpha-stable family of distributions in wavelet (WT) and contourlet (CT) domains for *Barbara* image .....59

Table 3.2: PSNR values obtained using denoising methods employing the alpha-stable family of distributions in wavelet (WT) and contourlet (CT) domains for *Peppers* image .....60

Table 3.3: PSNR values obtained using the proposed denoising method with different priors for two of the test images, *Barbara* and *Peppers*, when $\sigma_\eta$=10...61

Table 3.4: Averaged PSNR values obtained using the proposed denoising method over 60 textured images [99], when $\sigma_\eta$=20 .....61

Table 3.5: PSNR values obtained using the ML method and the proposed parameter estimation method for various noise levels.....63

Table 3.6: PSNR values obtained using denoising methods with various windows and image sizes .....63

Table 3.7: PSNR values obtained using various denoising methods for three of the test images, *Barbara*, *Boat* and *Lena* .....64

Table 3.8: Averaged PSNR values obtained using various denoising methods over 1000 images .....69

Table 3.9: MSSIM values obtained using proposed denoising method and some of the other existing methods for three of the test images, *Barbara*, *Boat* and *Lena*.....70

Table 3.10: Averaged RMSE values obtained for the MAP and MMAE estimators using the alpha-stable family of distributions over a number of test images corrupted by the Maxwell and Rayleigh noises with $\sigma = 5$ .....71

Table 3.11: PSNR values obtained using various denoising methods for two of the color images, *Lena* and P*eppers* .....77

Table 3.12: Averaged PSNR (in dB) values obtained using various denoising methods on the Kodak dataset.....79

Table 4.1: PSNR values obtained using different despeckling methods for synthetically-speckled *Boat* and *Lena* images .....87

Table 5.1: The computational complexity of the detectors based on the $S\alpha S$ , Cauchy and GG distributions.....106

Table 5.2: The computational complexity of the detectors based on the univariate Cauchy distribution using the contourlet and curvelet transforms .....110

# List of Symbols

| | |
|---|---|
| $H_1$ | Alternative hypothesis |
| $b_i$ | Binary sequence |
| $\alpha$ | Characteristic exponent of the alpha-stable distribution |
| $\phi(\omega)$ | Characteristic function |
| $\rho$ | Correlation coefficient |
| $\Sigma$ | Covariance matrix |
| $S_{m,n}$ | Cycle-spinning operator |
| $n$ | Dimensionality |
| $d$ | Direction number |
| $\gamma$ | Dispersion parameter of the alpha-stable distribution |
| $F$ | Fast Fourier transform |
| $p$ | Fractional lower order moment term |
| $\omega$ | Frequency |
| $\Gamma$ | Gamma function |
| $F^{-1}$ | Inverse fast Fourier transform |
| $k_x$ | Kurtosis value of the subband $x$ |
| $\Lambda$ | Likelihood ratio |
| $N$ | Number of coefficients in a subband |
| $\sigma_\eta$ | Noise standard deviation |
| $\eta$ | Noise term |
| $y$ | Noisy subband coefficients |

| | |
|---|---|
| $H_0$ | Null hypothesis |
| $D$ | Number of directions |
| $L$ | Number of look |
| $J$ | Number of scales |
| $\mu$ | Mean value |
| $\psi$ | Polygamma function |
| $P_f(f)$ | Probability density function |
| $P_{\text{det}}$ | Probability of detection |
| $P_{fa}$ | Probability of false alarm |
| $P_m$ | Probability of miss |
| $j$ | Scale number |
| $\beta$ | Shape parameter of the generalized Gaussian distribution |
| $s$ | Square-shaped window |
| $\sigma_x$ | Standard deviation of the subband $x$ |
| $\tau$ | Threshold |
| $\xi$ | Watermarking strength factor |
| $W$ | Watermark |
| $l$ | Widow size |

# List of Abbreviations

| | |
|---|---|
| AWGN | Additive white Gaussian noise |
| APD | Amplitude probability density |
| Bi | Bivariate |
| CT | Contourlet transform |
| DFB | Directional filter bank |
| DCT | Discrete cosine transform |
| DFT | Discrete Fourier transform |
| ENL | Equivalent number of looks |
| FFT | Fast Fourier transform |
| FLOM | Fractional lower order moment |
| GG | Generalized Gaussian |
| ICT | Inverse contourlet transform |
| IID | Independent and identically distributed |
| KSD | Kolmogorov-Smirnov distance |
| NLM | Non-local means |
| MAP | Maximum *a posteriori* |
| ML | Maximum likelihood |
| MSSIM | Mean structural similarity |
| MAD | Median absolute deviation |
| MMAE | Minimum mean amplitude error |
| MMSE | Minimum mean squared error |
| MPE | Multivariate power exponential |

| | |
|---|---|
| PSNR | Peak signal-to-noise-ratio |
| PDF | Probability density function |
| PDFB | Pyramidal directional filter bank |
| ROC | Receiver operating characteristics |
| RMSE | Root mean squared error |
| SAR | Synthetic aperture radar |
| SαS | Symmetric alpha-stable |
| Tri | Trivariate |
| 2-D | Two dimensional |
| WDR | Watermark to document ratio |
| WT | Wavelet transform |

# CHAPTER 1

# Introduction

## 1.1 General

Multiscale image analysis is known to be useful and indispensable to the field of image processing [1]. Depending on the requirements of an application, a variety of multiscale and multi-resolution transforms have been used. Signals can be effectively projected using these transforms. The wavelet transform is by far the most prevalent transformation in signal processing offering a multiscale and multi-resolution signal representation. In many applications such as classification, denoising, texture retrieval, restoration and watermarking, it has led to the development of very efficient algorithms, for instance, those in JPEG 2000 and video codecs [2]. This transform also offers sparsity and localization features to the transformed signals. However, the wavelet transform provides an optimal representation only to one-dimensional (1-D) piecewise smooth signals [3]. A direct extension of wavelets to higher dimensions by the tensor product of 1-D wavelets does not provide an optimal representation to multidimensional signals such as images. This is because of the intrinsic geometrical structure of typical natural images [3], [4]. In other words, the separable wavelets are optimal only in representing point discontinuities in two-dimensional (2-D) signals, but not optimal in capturing line discontinuities, which correspond to directional information in images. This is in view of the fact that 2-D wavelet transforms provide a limited number of directions resulting in capturing only partial directional information from images. In order to overcome this deficiency of the wavelet transform for 2-D signals, the contourlet transform has been proposed in [4] as a

new image decomposition scheme that provides an efficient representation for 2-D signals with smooth contours. The contourlet transform not only has the multiscale and time-frequency localization features of the wavelet transform, but it offers a higher degree of directionality with better sparseness, and as such, outperforms the wavelet transform [4]. The contourlet transform also recognizes the smoothness of the contour in images. There are a number of other multiscale representations such as the dual-tree complex wavelet transform [5], ridgelet transform [6] and curvelet transform [7]-[9] that also provide multiscale and directional image representation. However, the contourlet transform can provide a flexible number of directions in each subband, and in this regard, this transform is superior to the complex wavelet transforms. Compared to the curvelet transform, the contourlet transform is preferred, since it is defined on rectangular grids and offers a seamless translation to the discrete world [4]. Moreover, the contourlet transform has a 2-D frequency partitioning on concentric rectangles rather than on concentric circles as in the case of the curvelet, and hence, overcomes the blocking artifact deficiency of the curvelet transform. Further, due to the use of iterated filter banks, the contourlet transform is computationally more efficient than the curvelet transform. In view of the above properties, the contourlet transform has become a suitable candidate in many image processing applications.

Images are often corrupted by noise during the acquisition and transmission processes, leading to significant degradation of image quality for the human interpretation and post-processing tasks. Therefore, denoising is essential for images not only to improve the image quality, but also to proceed with further data analysis. It is required to preprocess images and remove the noise while retaining as much as possible the important image

features. Therefore, finding a better image denoising algorithm is of the utmost importance. In view of the properties of the contourlet transform, an image denoising problem can be effectively addressed in the contourlet domain.

With the huge amount of transferred data over the internet, the duplication of digital images has created a new set of challenging problems in digital world. Watermarking is regarded an indispensable requirement for copyright protection, authentication and ownership verification of all kinds of data especially images which is more prone to be copied, counterfeited and shared. Through invisible insertion of an auxiliary signal in digital images, one can potentially solve the piracy and ownership problems. This auxiliary signal should remain intact under any intentional or unintentional distortions, allowing us to protect the ownership rights in digital images. Therefore, finding a robust watermarking scheme is desirable. In view of the above-mentioned properties of the contourlet transform, a watermarking scheme in the contourlet domain can be a good solution for the robustness problem.

Many problems in image processing require a prior probability model of images. This is true for a wide range of applications in which measurements and observations are regarded as stochastic processes. In these applications, the theoretical limits of an algorithm can be overcome by a prior model of the underlying signal. For images, a statistical model is considered as a particular prior probability model for the underlying frequency domain coefficients for capturing certain characteristics of an image in a small number of parameters so that they can be used as prior information in image processing tasks [10]. Statistical modeling of images in the transform domain has recently attracted

much research interests, since understanding the statistical properties of transform domain coefficients may result in developing new algorithms for image processing tasks.

This thesis is concerned with the modeling of the contourlet coefficients of images and its application in on image denoising and image watermarking.

## 1.2 A Brief Literature Review on Image Denoising and Watermarking in the Contourlet Domain

Many image denoising and watermarking schemes have been recently investigated in the contourlet domain.

In image denoising applications, it has been shown that the removal of the noise performed in the contourlet domain is superior to those conducted in the wavelet domain [11], [12]. Most of the image denoising algorithms in the contourlet domain have been developed based on the thresholding or shrinkage functions [11] in which the coefficients with small magnitudes are simply set to zero, while the rest are kept unchanged in the case of hard-thresholding, and shrunk in the case of soft-thresholding. In recent years, statistical models have been adopted for the transform domain coefficients in which the image and noise are modeled as random fields and Bayesian methods are employed to develop shrinkage functions for the estimation of the noise-free coefficients from the noisy observations [12]. It is to be noted that the prior distributions for the original image and the noise have considerable effect on the performance of the denoising algorithm. Several prior distributions have been employed to characterize the transformed coefficients of images [15]-[21]. The contourlet transform has been considered to be a

decorrelator for images, and thus the transform domain coefficients have been assumed to be independent and modeled by using marginal statistics such as the generalized Gaussian (GG) distribution [3]. However, these distributions are not capable of accurately capturing the peak and tails of the empirical distribution [15]. Moreover, the contourlet coefficients of an image have been shown to have across scale dependencies with their parents and children [3]. Therefore, it is necessary to consider the inter-scale dependencies of the contourlet coefficients in order not only to capture the heavy tails of the distribution of the contourlet coefficients, but also to take into account the contourlet coefficient dependencies across the scales. The Bayesian estimators utilizing such priors can then be developed for denoising purposes.

In watermarking applications, there exist several studies in which embedding procedure is performed in a transform domain such as in the discrete Fourier transform (DFT) [22], [23] discrete cosine transform (DCT) [24]-[26] and discrete wavelet transform (DWT) [27]-[29]. Recently, a number of watermarking schemes have been proposed, wherein the watermark is embedded into the contourlet coefficients of the image [14]. In view of the above-mentioned properties of the contourlet transform, several algorithms have been developed suggesting that the performance of the contourlet-domain watermarking algorithms is superior to those based on other frequency-domain watermarking algorithms in terms of their resilience to common image processing attacks and the invisibility of the embedded watermark [14], [30]-[35]. The most commonly used detector for the frequency domain watermarking schemes is the correlation-based detector, which is optimal only if the data samples follow the Gaussian distribution function [37]. If these data samples are not Gaussian, optimal or sub-optimal detectors

are developed by modeling the frequency domain coefficients using non-Gaussian probability density functions (PDF), such as the Laplacian [28] Student-t [36], and GG distributions [13], [24], [37], [38].

Since the distribution of the contourlet domain coefficients of images have large peaks around zero and tails heavier than that of a Gaussian PDF, an appropriate choice of the distribution to model the statistics of the contourlet coefficients would be the one having a heavy-tailed PDF. For this purpose, in [13], an attempt has been made to model the contourlet coefficients using the GG distribution. However, this PDF still cannot provide an accurate fit to the empirical density function of the images in the transformed domain [15] and thus, the performance of image denoising and watermarking schemes based on the GG PDF is not sufficiently satisfactory [14].

## 1.3 Objective and Organization of the Thesis

The objective of this thesis is to study the properties of the contourlet subband coefficients of images through their suitable statistical modeling and apply this model in developing efficient algorithms for image denoising and watermarking.

Various existing distributions are examined from the viewpoint of their suitability to model the contourlet image coefficients. It is shown that the distribution of the contourlet subband coefficients of images is highly non-Gaussian, i.e., the tails of the distribution are heavier and the peak is sharper than a Gaussian PDF. This non-Gaussian behavior of the distribution of the contourlet coefficients of images and its comparison with various other PDFs, leads to the modeling of the contourlet coefficients of images using the alpha-stable family of distributions in this investigation. It is established that the

univariate members of this family are capable of accurately fitting the marginal distribution of the empirical data and that the bivariate members accurately characterize the inter-scale dependencies of the contourlet coefficients of an image. Based on these modeling results, statistical estimation and detection techniques are developed for image denoising and watermarking applications. The Bayesian maximum *a posteriori* and minimum mean absolute error based denoising algorithms are developed to obtain the noise-free contourlet coefficients of grayscale and color images as well as synthetic aperture radar images. A spatially-adaptive method using the fractional lower order moments is proposed to estimate the parameters of the model. Next, blind watermark detectors in the contourlet domain are designed by using the univariate and bivariate alpha-stable distributions. The closed-form expressions are derived for the log-likelihood-based multiplicative watermark detection algorithm for grayscale images using the univariate and bivariate Cauchy members of the alpha-stable family. A multiplicative multichannel watermark detector is also designed for color images using the multivariate Cauchy distribution.

The thesis is organized as follows.

In Chapter 2, a brief introduction of the contourlet transform is presented. It is shown that a number of advantages can be drawn from the use of the contourlet transform over that achieved using other multi-scale and multi-dimensional transforms. The statistical properties of the contourlet coefficients of images are studied showing that the contourlet coefficients follow a non-Gaussian distribution with heavy tails. The alpha-stable family of distributions provides a more accurate fit to the empirical data than that provided by other non-Gaussian distributions.

Based on the modeling results, a novel image denoising scheme in contourlet domain is proposed in Chapter 3 by using the alpha-stable family of distributions. Both the univariate and bivariate distributions are considered for the contourlet coefficients in order to remove the noise from images. In order to estimate the noise-free contourlet coefficients, Bayesian MAP and MMAE estimators are developed. To estimate the unknown parameters of the alpha-stable distribution more accurately, a new parameter estimation method based on the fractional lower order moments of the empirical data is proposed. An extension of the proposed denoising scheme to color images, is also carried out by taking into account the dependencies between the RGB color channels. The proposed denoising scheme based on the alpha-stable distribution is compared to other existing methods in terms of the peak signal-to-noise ratio and mean structural similarity index, as well as in terms of the visual quality of the denoised images.

In Chapter 4, despeckling of SAR images in the contourlet domain is studied. In order to remove the multiplicative speckle noise from SAR images, a homomorphic filtering-based method is proposed wherein the alpha-stable PDF is used as a prior for describing the log-transformed contourlet coefficients. A Bayesian MAP estimator using the symmetric alpha-stable distribution is designed to estimate the noise-free coefficients. Simulations are conducted using synthetically-speckled and real SAR images, and the performance of the proposed method using the MAP estimator is evaluated.

In Chapter 5, a novel blind image watermarking scheme in the contourlet domain is proposed. Watermark detectors in the contourlet domain using the univariate and bivariate alpha-stable distributions are designed. Watermark detectors based specifically on the univariate and bivariate Cauchy members of the alpha-stable family, which lead to

closed-form expressions for the test statistics, are also designed. The detectors based on the alpha-stable distribution and its Cauchy member are then evaluated against various kinds of attacks and compared to that of the GG-based detector.

In Chapter 6, a new color image watermarking scheme is presented and a multichannel multiplicative watermark detector for color images in the contourlet domain is designed. In order to take into account the cross-correlation that exist between the coefficients of the color bands, a statistical model based on the multivariate Cauchy distribution is presented. The performance of the multivariate Cauchy-based detector is evaluated by conducting several experiments and the results are compared to that of the other existing detectors for color images.

Finally, some concluding remarks and scope for further research are presented in Chapter 7.

# CHAPTER 2

# Contourlet Transform of Images and Modeling of its Coefficients

## 2.1 Introduction

Wavelet transform has been established as a tool for generating efficient representations for piecewise continuous 1-D signals. Natural images consist of 1-D piecewise smooth lines as well as many discontinuity points along smooth contours. However, separable wavelets cannot efficiently capture directional information in 2-D signals. To overcome this deficiency, many directional image representations have been proposed to find new two-dimensional transforms such as steerable pyramid [39], brushlets [40], complex wavelets [5], and curvelet [8], that can better capture the geometrical structures of edges. Candes and Donoho initially developed the curvelet transform [7] in the continuous domain via multiscale filtering followed by applying the ridgelet transform on each bandpass image. These authors later proposed a second generation of the curvelet transform [8] that was defined through frequency partitioning without employing the ridgelet transform. Both the curvelet constructions are established on a 2-D frequency partitioning based on the polar coordinates. This converts the curvelet transform simple to the continuous domain, but causes the implementation for discrete images, sampled on a rectangular grid, to be very challenging. In particular, achieving critical sampling is difficult in such a discretized construction. Inspired by the curvelets, the contourlet

transform has been developed by Do and Vetterli [4] directly in the discrete domain by employing non-separable filter banks. This transform is defined on a rectangular grid, and thus it has 2-D frequency partitioning on concentric squares, rather than on concentric circles as in the case of the curvelet. Contourlet transform not only possesses the main features of wavelets, such as time-frequency localization, but also offers a richer degree of directionality and anisotropy [4]. The difference between the contourlet transform and other multiscale directional transforms is that the contourlet transform allows a flexible number of directions at each scale. The contourlet transform can effectively capture smooth curves and contours that are the main features in natural images. This transform consists of two stages: the Laplacian pyramid filters are used as the first stage and directional filter banks as the second one.

In view of the appealing characteristics of the contourlet transform in capturing both the geometric structures and smooth contours in images, it has received considerable attention in recent years and has been regarded an alternative to other multi-resolution transforms in many image processing applications such as feature extraction, text retrieval, image denoising, image watermarking and feature extraction [13], [41], [42]. In view of this, in this chapter, first a brief introduction of the contourlet transform is given and then the statistical characteristics of the contourlet subband coefficients of images are comprehensively studied [15], [43]. The contourlet coefficients within a subband is shown to have highly non-Gaussian properties. In view of this, in order to model the distribution contourlet coefficients of images, we propose using the alpha-stable family of distributions. The modeling performance of this distribution is then investigated in details and compared to that of the previously-used models in the contourlet domain.

## 2.2 Contourlet Transform

### 2.2.1 Laplacian Pyramid

Multiscale data representation is known to be a powerful tool in many applications. It can capture data in a hierarchical manner where each level corresponds to a lower resolution approximation. One way of achieving a multiscale decomposition for images is to use a Laplacian pyramid [44] which has been used in many applications. It is known that the major feature of the Laplacian pyramid representation is that, it is oversampled or redundant, i.e., there are more coefficients after the Laplacian pyramid analysis than the pixels in the input image. This feature is desirable in many applications such as image denoising and watermarking, and undesirable in image compression.

The Laplacian pyramid has analysis and synthesis processes. The Laplacian pyramid decomposition at each level generates a sampled lowpass version of the input image of a certain size and the difference between the input and the prediction, resulting in residual signal, i.e., the prediction error. The process may be iterated on the coarse version. A lowpass compression filter is employed to obtain the coarse coefficients that approximate the original image and a lowpass prediction filter is used to predict the input image from the coarse coefficients. Typically, for reconstruction, the image is obtained by adding back the difference to the prediction from the coarse image. Analysis and synthesis parts of the Laplacian pyramid are shown in Figure 2.1(a) and Figure 2.1(b), respectively. The Laplacian pyramid decomposition at each step generates a sampled lowpass version of the original and the difference between the original and the prediction, resulting in a bandpass image. An example of applying the Laplacian pyramid to the *Barbara* image is shown in Figure 2.2. In this figure five scales are considered in which there is one

lowpass and one bandpass image. A drawback of the Laplacian pyramid is the inherent oversampling, i.e., the number of coefficients after applying the Laplacian pyramid is greater than the number of pixels of the original image which means the Laplacian pyramid is a redundant image representation [45]. Despite this redundancy, Laplacian pyramid is preferred over critically sampled wavelet scheme for some primary reasons. First, it is simpler as it requires only a pair of lowpass filters. Second, the Laplacian pyramid has the distinctive feature that each pyramid level generates only a bandpass image, which does not have “scrambled” frequencies [4].

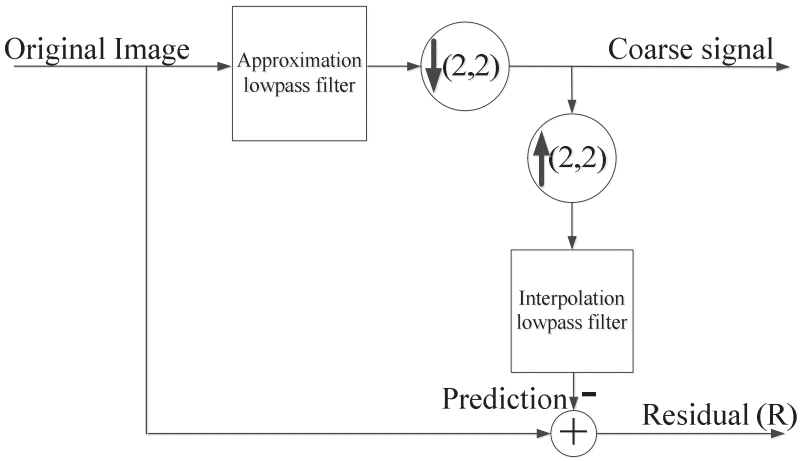


(a)

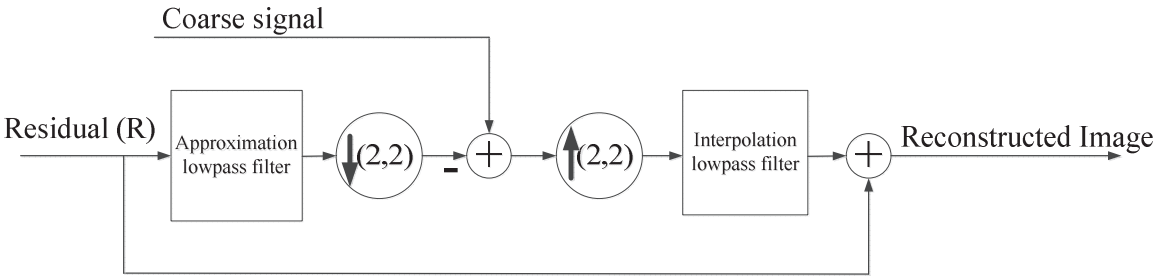


(b)

Figure 2.1. a) Analysis part of the Laplacian pyramid; the outputs are a coarse approximation and a residual between the original image and the prediction. b) Synthesis part of the Laplacian pyramid.

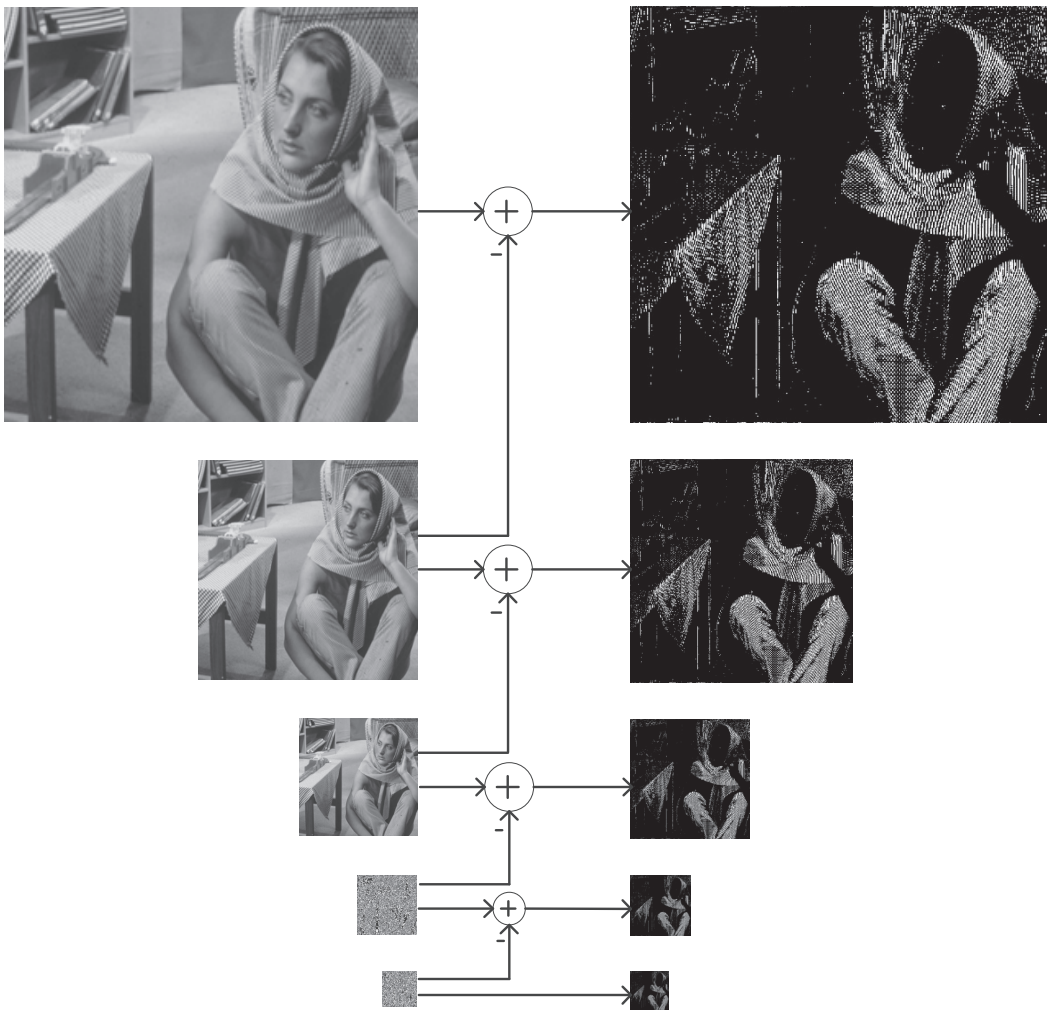

Figure 2.2. Five levels of decomposition using the Laplacian pyramid. In each level, there is a lowpass and a bandpass part.

The frequency scrambling happens in the usual wavelet scheme when highpass filtering and downsampling are performed. It is the folding back of the high frequency band into the low frequency band, and thus the spectrum is reflected. In the Laplacian pyramid, this effect is avoided by downsampling only the lowpass channel, and not the highpass channel. Consequently, the Laplacian pyramid permits further subband decomposition to be applied to its bandpass images. The bandpass images can be fed into the next level of process so that more information such as geometrical information can be captured [3]. In the contourlet transform the next level is called the directional filter bank, which is applied to each single bandpass image.

### 2.2.2 Directional Filter Bank

The directional filter bank has been introduced in [46] where the individual channels are critically sampled without no information loss. In other words, the directional filter bank can be realized by decomposing an image into angular components which are maximally decimated while still allowing the original image to be fully reconstructed from its decimated channels. The directionally-oriented representation implemented by the directional filter bank is very useful for the applications exploiting aspect of visual perception, since retina and visual cortices have cells with directional selectivity [47]. The directional filter bank can be used in applications such as feature extraction, image enhancement, image watermarking and image denoising. The key idea of the directional filter bank is to divide the frequency plane into many frequency directions. The frequency plane partitioning of a directional filter bank with sixteen subbands in each scale is shown in Figure 2.3.

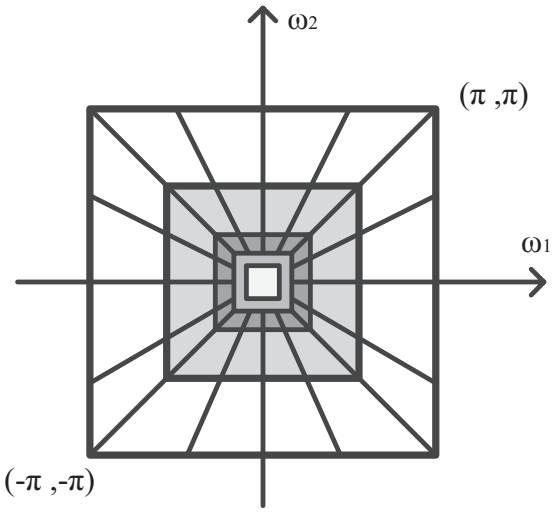


Figure 2.3. An example of possible frequency partitioning by the contourlet transform.

The directional filter bank is a maximally-decimated and perfect reconstruction filter bank. This means that the total number of subband coefficients is the same as the pixels of the original image, and are used to reconstruct the original image without any error. The directional filter bank is implemented by a decomposition tree structure of two-band systems. The wedge-shaped frequency partition of a directional filter bank is realized by an appropriate combination of directional frequency partitioning by the two-channel filters [3], [4], [46].

### 2.2.3 Pyramidal Directional Filter Bank

The directional filter bank is intended to capture the high frequency components and represent the directionality of an image. On the other hand, the low frequency components may be poorly handled by this filter bank. In fact, with the frequency partition shown in Figure 2.3, low frequencies leak into many directional subbands, and hence the directional filter bank may not provide a sparse representation for images. In view of this, the low frequency components must be removed before applying the directional decomposition. This provides a logical reason to combine the directional filter bank with a multiresolution scheme. As discussed, the Laplacian pyramid permits further subband decomposition to be applied on its residual images. These residual images can be fed into a directional filter bank so that directional information are efficiently captured. The scheme can be iterated repeatedly on the coarse image as shown in Figure 2.4. The result is a double iterated filter bank structure, named pyramidal directional filter bank (PDFB), which decomposes an image into directional subbands at multiple scales. The scheme is flexible since it allows for a different number of directions at each scale. Image reconstruction is done using a procedure that is inverse of the decomposition procedure.

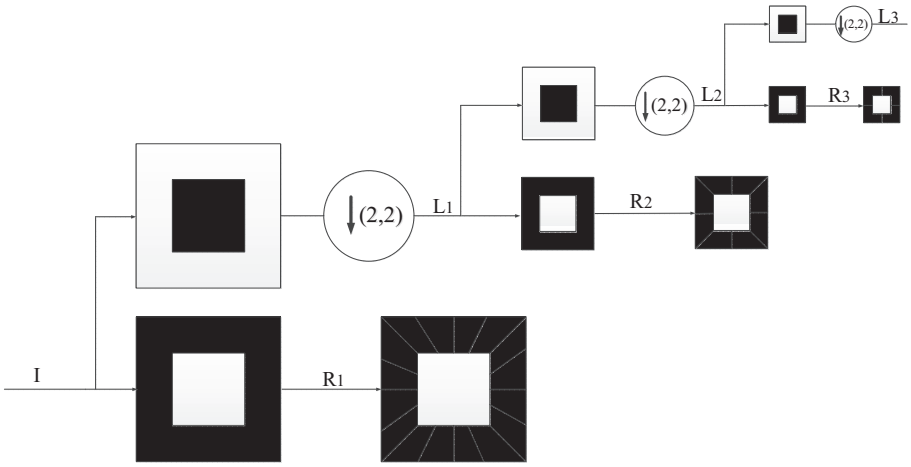


(a)

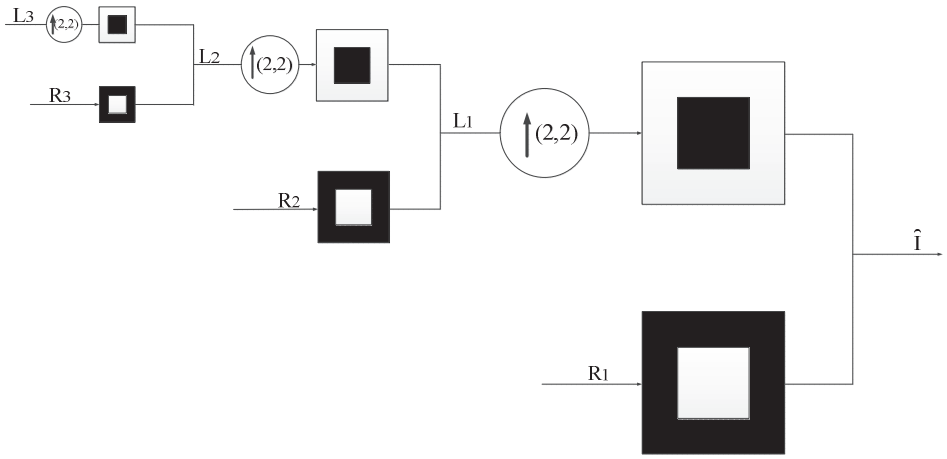


(b)

Figure 2.4. Block diagram of the contourlet filter bank structure. a) In analysis, the Laplacian pyramid is applied to the original image in order to have multiscale decomposition where the coarse image, denoted by "L", is iteratively subsampled and each residual image, denoted by "R", is fed into directional filter bank to obtain directional information. The scheme is flexible since it allows for a different number of directions at each scale. b) In synthesis, the original image is reconstructed using the same filters for Laplacian pyramid as in analysis part.

With perfect reconstruction Laplacian pyramid and directional filter bank, the PDFB is obviously perfect reconstruction. It should be pointed out that there are other multiscale and directional decompositions such as the cortex transform [48] and the steerable pyramid [39]. However, PDFB differs from those in that it allows different number of directions in each scale. An example of applying the PDFB to *Barbara* image is shown in Figure 2.5. The image is first decomposed into two pyramidal levels followed by eight and four directional subbands.

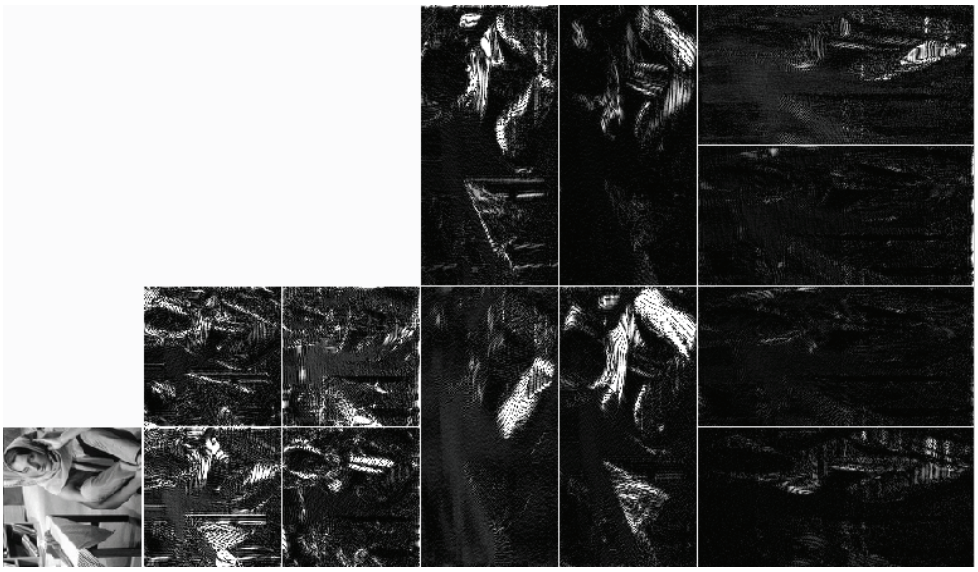

Figure 2.5. Contourlet representation of the *Barbara* image. The original image is first decomposed into two pyramidal levels followed by eight and four directional subbands.

## 2.3 Statistical Modeling of the Contourlet Coefficients

It is known that the contourlet coefficients of images have non-Gaussian and heavy-tailed properties that are best described by the heavy tailed distributions [14], [15]. This can be observed through studying the statistics of the contourlet coefficients of natural images. In Figure 2.6, histograms of the contourlet coefficients for the *Barbara* image are obtained when two finest scales with eight directions in each scale are considered. In comparison to a Gaussian distribution, these densities are more sharply peaked around zero with more extensive tails. This implies that the contourlet transform is sparse, as the majority of coefficients are close to zero. This is due to the fact that the spatial structure images are mostly dominated by the smooth areas with occasional edges or other abrupt transitions. These smooth regions lead to many small coefficients and occasional large coefficients. In order to quantify this, we compute the kurtosis value [49], i.e., the fourth moment divided by squared second moment. The kurtosis value is defined as

$$k_x = \frac{1}{\sigma_x^4} \frac{1}{N} \sum_{i=1}^{N} x_i^4 \tag{2-1}$$

where $x$ is a zero mean random variable with the standard deviation of $\sigma_x$ and $N$ is the number of coefficients in a subband. The estimated kurtoses of all of the subbands are significantly larger than the kurtosis value of a Gaussian distribution, namely, three. Similar results have also been observed for other test images which verify the non-Gaussianity of the contourlet coefficients of natural images, i.e., having large peaks around zero and tails heavier than that of the Gaussian PDF.

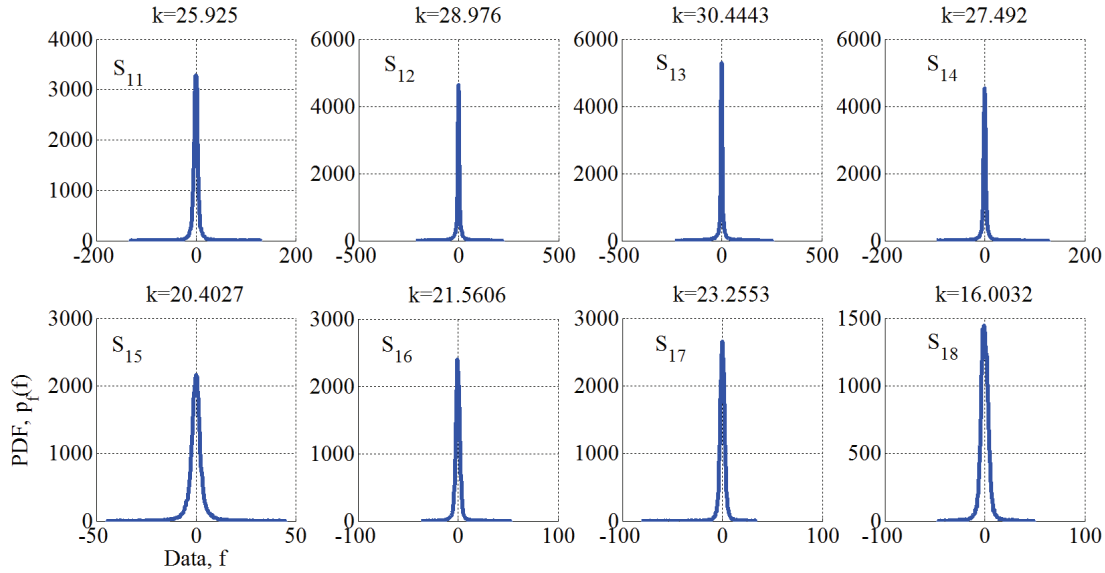


(a)

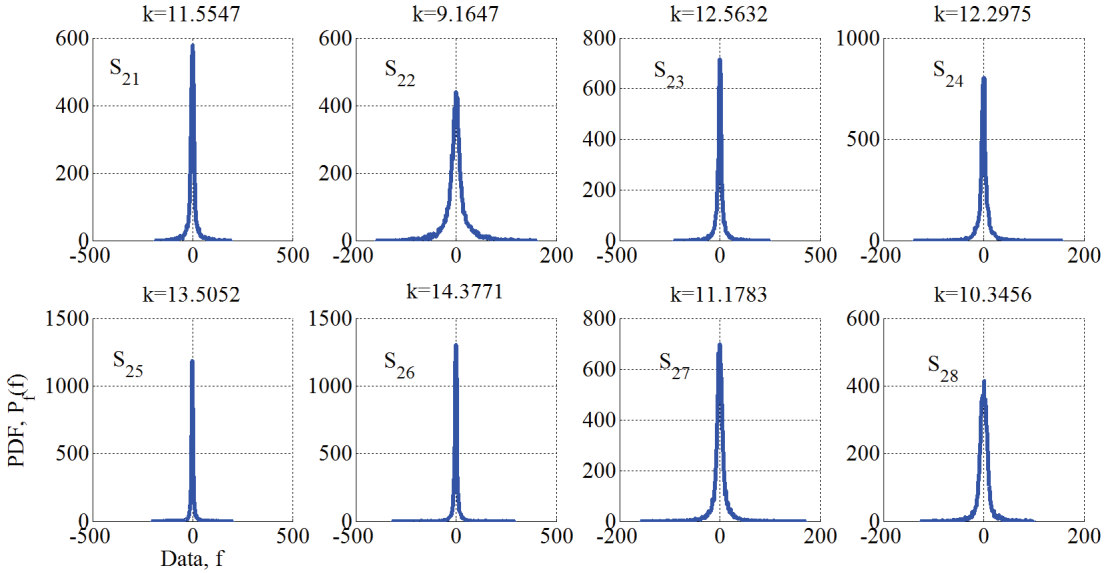


(b)

Figure 2.6. Histograms of the contourlet coefficients of two finest scales for *Barbara* image. The kurtosis value $k$ shows the degree of the non-Gaussianity for the coefficients of each subband. a) Finest scale and b) Second finest scale.

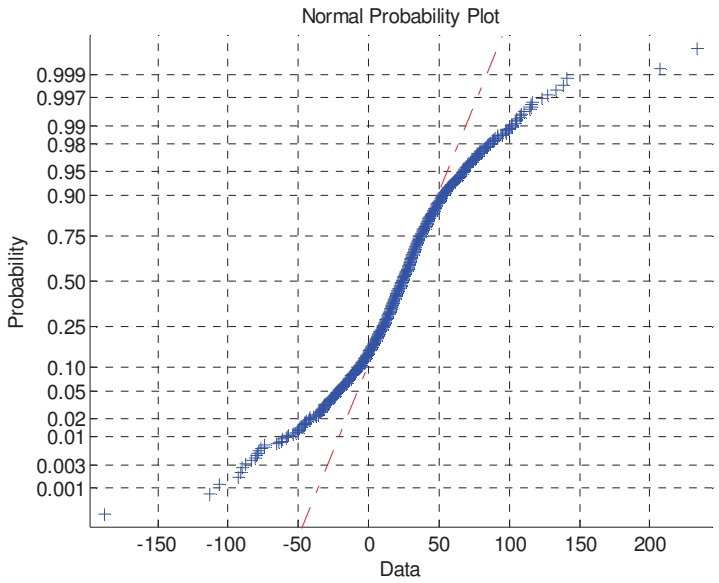


Figure 2.7. Normal probability plot of the *Barbara* image. The empirical data does not follow a straight line showing that the data is not Gaussian.

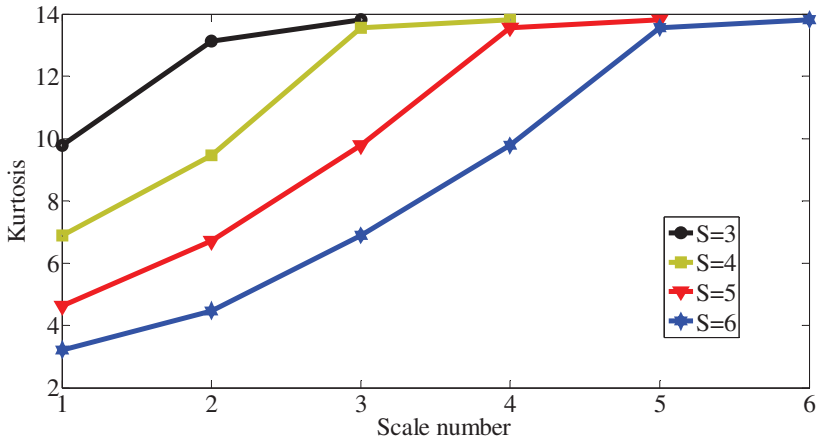


Figure 2.8. Average kurtosis values of contourlet subband coefficients for various values of the number of subbands $S$.

The normal probability plot, a graphical technique for normality testing, displayed in Figure 2.7, for the *Barbara* image, shows that the empirical data deviates from the normal distribution and that it is heavy-tailed. Figure 2.8 shows the averaged kurtosis value of the contourlet subband coefficients over 96 images, taken from [50], for different values of the number of subbands as a function of the scale number. It is seen from this figure that the kurtosis value is close to, yet greater than, the kurtosis value of the Gaussian distribution, namely, three, when the number of scales is increased. It indicates that in higher scales of a multiscale representation such as the contourlet transform, the distribution of the subband coefficients is closer to the Gaussian distribution [15]. In view of this, choosing an appropriate number of scales has a great influence on modeling the transformed domain coefficients by a non-Gaussian distribution.

### 2.3.1 Generalized Gaussian Distribution

In view of the fact that the distribution of the contourlet coefficients of images is non-Gaussian, a proper distribution to model the statistics of the contourlet coefficients is a heavy-tailed PDF. It has been shown in [13] that the generalized Gaussian distribution can be used to model the marginal density of the contourlet coefficients. The generalized Gaussian distribution is characterized by its PDF given by

$$f_{GG}(x;\sigma,\beta) = C(\sigma,\beta)\, e^{-[\alpha(\sigma,\beta)|x|]^{\beta}} \tag{2-2}$$

where $\alpha(\sigma,\beta)=\sigma^{-1}[\Gamma(3/\beta)/\Gamma(3/\beta)]^{0.5}$, $C(\sigma,\beta)=\beta\alpha(\sigma,\beta)/2\Gamma(1/\beta)$, $\sigma$ is the standard deviation of $x$, $\beta$ is the shape parameter and $\Gamma(z)=\int_0^\infty e^{-t}t^{z-1}dt,\ z>0$ is the Gamma function. The generalized Gaussian model contains the Gaussian and Laplacian PDFs as special cases when $\beta=2$ and $\beta=1$, respectively. There are a number of methods to estimate the GG parameters [51]-[56]. The common estimator for GG parameters is the maximum-likelihood estimator since it has been shown to be more accurate for heavy-tailed distribution of the subband coefficients [55], [56].

### 2.3.2 Alpha-Stable Family of Distributions

The generalized Gaussian distribution has been used to model the contourlet coefficients of images [13]. However, this distribution is not capable of accurately capturing the peak and tails of the empirical distribution [15]. In order to overcome this deficiency, we propose the use of the alpha-stable family of distributions as a heavy-tailed PDF, to characterize the distribution of the contourlet subband coefficients of natural images. This model is suitable for describing signals that are highly non-Gaussian. The use of alpha-stable distributions as statistical models for signals is due to two important reasons [57]. First, stable random variables should satisfy the stability property, i.e., any linear combination of the stable variables are still stable (shape of the distribution is unchanged). Second, according to the generalized central limit theorem, the limiting process of sums of independent and identically distributed (i.i.d.) random variables is stable. Several experiment have suggested that many data sets in several physical systems show heavy tail features that can be justified by the use of stable models [57], [58]. In

view of this and the non-Gaussian properties of the contourlet coefficients, the alpha-stable family is assumed to be a prior for the contourlet coefficients of images. A random variable $X \sim S_\alpha(\gamma,\beta,\delta)$ is distributed by the alpha-stable distribution and best described by its characteristic function [57], [59]

$$\varphi(\omega) = \exp\{\, j\delta\omega - \gamma|\omega|^\alpha[1 + j\beta sign(\omega)\varpi(\omega,\alpha)]\} \tag{2-3}$$

where

$$\varpi(\omega,\alpha) = \begin{cases} \tan\dfrac{\alpha\pi}{2} & if\ \alpha \neq 1 \\ \dfrac{2}{\pi}\log|\omega| & if\ \alpha = 1 \end{cases} \tag{2-4}$$

and $\alpha$ is a characteristic exponent, $0 < \alpha \leq 2$, $\delta \in \Re$ a location parameter, $\beta \in [-1,1]$ a skewness parameter and $\gamma > 0$ a dispersion parameter. A stable distribution is called standard if $\delta = 0$ and $\gamma = 1$. If $\beta = 0$, the distribution is called symmetric alpha-stable ($S\alpha S$). The characteristic function of a $S\alpha S$ distribution simplifies to

$$\varphi(\omega) = \exp(\, j\delta\omega - \gamma|\omega|^\alpha) \tag{2-5}$$

The characteristic exponent $\alpha$ determines the shape of the distribution. The smaller the value of $\alpha$, the heavier the tail of the distribution. Thus, the $S\alpha S$ distributed random variables with small $\alpha$ are impulsive. By using power series expansions, the standard $S\alpha S$ density function for a random variable $X \sim S_\alpha(1,0,0)$ is given by [57]

$$f_\alpha(x)=\begin{cases}\frac{1}{\pi x}\sum_{k=1}^{\infty}\frac{(-1)^{k-1}}{k!}\Gamma(\alpha k+1)x^{-\alpha k}\sin(\frac{k\alpha\pi}{2}), & 0<\alpha<1\\ \frac{1}{\pi(x^2+1)}, & \alpha=1\\ \frac{1}{\pi\alpha}\sum_{k=0}^{\infty}\frac{(-1)^{k}}{2k!}\Gamma(\frac{2k+1}{\alpha})x^{2k}, & 1<\alpha<2\\ \frac{1}{2\sqrt{\pi}}\exp(-\frac{x^2}{4}), & \alpha=2\end{cases} \tag{2-6}$$

It should be noted that there are three special cases of the alpha-stable PDF that have closed-form expressions, namely, the Levy $(\alpha=0.5)$, Cauchy $(\alpha=1)$ and Gaussian $(\alpha=2)$ PDFs. In Figures 2.9 (a) and 2.9 (b), for different values of $\alpha$, the PDFs and CDFs of standard $S\alpha S$ distributions are, respectively, depicted.

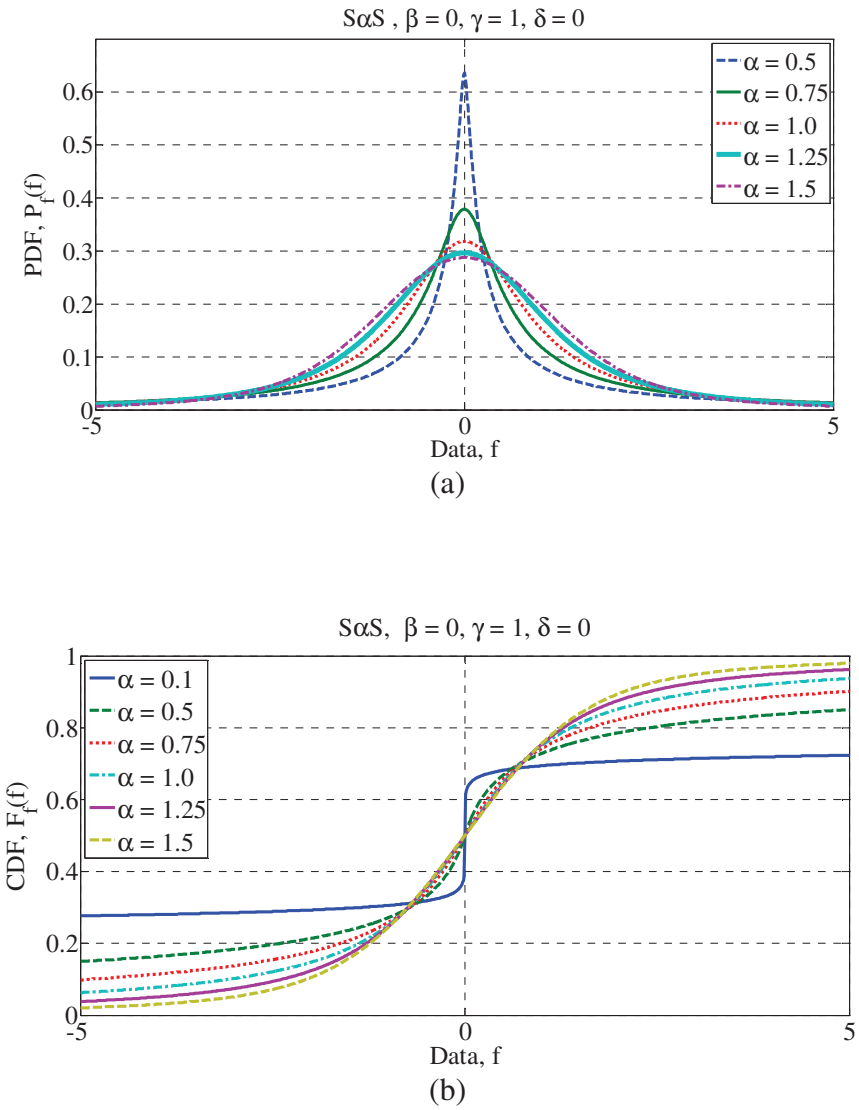


Figure 2.9. a) PDFs and b) CDFs of $S\alpha S$ distributions for different values of the characteristic exponent $\alpha$.

## 2.4 Parameter Estimation of the Alpha-Stable Distribution

A zero-mean symmetric $S\alpha S$ distribution is characterized by two parameters: the characteristic exponent $0 < \alpha \leq 2$, the dispersion parameter $\gamma > 0$. Various methods have been so far presented for estimating the parameter of the alpha-stable family of distributions, namely, tail power law method [57], quantile-based method [57], [60], maximum likelihood method [58], [61]-[63], characteristic function-based method [64]-[66], moments method [67] and fractional lower order moments method [68].

### 2.4.1 Characteristic Function Method

The characteristic function method is based on minimizing the distance between the theoretical and empirical characteristic functions [64]. The sample characteristic function is defined as

$$\hat{\Phi}(\omega) = \frac{1}{N} \sum_{k=1}^{N} \exp(j\omega x_k) \tag{2-7}$$

where $N$ is the sample size and $x_1,...,x_N$ are the observations. The distance between the theoretical and empirical characteristic functions can be formulated by mean of a Hermitian quadrature formula as [66]

$$\int_{-\infty}^{\infty} \left| \Phi(w) - \hat{\Phi}(w) \right|^2 W(w) dw = \sum_{i=1}^{n} \psi_k \left\| \Phi(w) - \hat{\Phi}(w) \right\| \tag{2-8}$$

where $w_k$'s are zeros of the Hermite polynomials of order $n$, $\psi_k$'s are the respective weights and $W(w) = \exp(-w^2)$.

### 2.4.2 Moments Method

The moment method is based on the relations between the logarithm of the characteristic function $\alpha$, power of its argument and $\gamma$ [67]. Solving this equation for a number of values produces estimates for both parameters. In this case, a number of frequencies like $\omega_1, \omega_2, ..., \omega_n$ and their inverses $1/\omega_1, 1/\omega_2, ..., 1/\omega_n$ are chosen for estimation purpose. After taking natural logarithm of the characteristic function in (2-7), we have

$$\begin{aligned} \log\left|\Phi_x(\omega_1)\right| &= -\gamma\left|\omega_1\right|^\alpha \\ \log\left|\Phi_x(\frac{1}{\omega_1})\right| &= -\gamma\left|\frac{1}{\omega_1}\right|^\alpha \end{aligned} \tag{2-9}$$

Replacing $\Phi_x(\omega)$ by its estimate $\hat{\Phi}_{Nx}(\omega)$, we obtain $\gamma$ as

$$\log\hat{\Phi}_{Nx}(\omega_1)\log\hat{\Phi}_{Nx}(1/\omega_1) = \gamma^2 \tag{2-10}$$

Note that $\omega_1$ and $\omega_2$ are known and after some mathematical simplification, parameter $\alpha$ can be obtained as

$$\hat{\alpha} = \frac{\log(-\frac{\log\hat{\Phi}_{Nx}(|\omega_1|)}{\hat{\gamma}})}{\log(|\omega_1|)} \tag{2-11}$$

where $\hat{\gamma}$ is an estimate of $\gamma$. When the number of frequencies is increased, the theoretical formulation becomes challenging. The moment method of estimation can be generalized using two frequencies as

$$\begin{aligned} \log\left|\Phi_X(\omega_1)\right| &= -\gamma\left|\omega_1\right|^{\alpha}, \log\left|\Phi_X(\frac{1}{\omega_1})\right| = -\gamma\left|\frac{1}{\omega_1}\right|^{\alpha} \\ \log\left|\Phi_X(\omega_2)\right| &= -\gamma\left|\omega_2\right|^{\alpha}, \log\left|\Phi_X(\frac{1}{\omega_2})\right| = -\gamma\left|\frac{1}{\omega_2}\right|^{\alpha} \end{aligned} \tag{2-12}$$

After some mathematical simplification, we have

$$\frac{\omega_1^{\alpha} + \omega_1^{-\alpha}}{\omega_2^{\alpha} + \omega_2^{-\alpha}} = \frac{\log\hat{\Phi}_{Nx}(\omega_1) + \log\hat{\Phi}_{Nx}(1/\omega_1)}{\log\hat{\Phi}_{Nx}(\omega_2) + \log\hat{\Phi}_{Nx}(1/\omega_2)} \tag{2-13}$$

An estimate of $\alpha$ is calculated by using (2-13) and employed in (2-9) to find $\gamma$.

### 2.4.3 Fractional Lower Order Moment Method

It is known that the second moment of an $S\alpha S$ random variable $X$, i.e., $E[X^2]$, does not exist. However, moments of order less than $\alpha$ do exist and are called the fractional lower order moments (FLOM) [68]. The FLOMs are defined by $E[\left|X\right|^p]$, $0 < p < \alpha \leq 2$ and can be obtained from the dispersion and characteristic exponents as

$$E[\left|X\right|^p] = \begin{cases} C(p,\alpha)\gamma^{p/\alpha}, 0 < p < \alpha \\ \infty \qquad\quad , p \geq \alpha \end{cases} \tag{2-14}$$

where

$$C(p,\alpha)=\frac{2^{p+1}\Gamma(\frac{p+1}{2})\Gamma(\frac{-p}{\alpha})}{\alpha\sqrt{\pi}\Gamma(\frac{-p}{\alpha})} \tag{2-15}$$

when $-1<p<\alpha$, $E[|X|^p]$ is called negative order moment [69], [70]. The parameters $\alpha$ and $\gamma$ can be estimated in terms of the estimated moments (positive and negative) as

$$E[|x|^p]E[|x|^{-p}]=C(p,\alpha)C(-p,\alpha)=\frac{2\tan(\frac{p\pi}{2})}{\alpha\sin(\frac{p\pi}{2})} \tag{2-16}$$

By assuming a predefined value for $\varepsilon$, an estimation of $\alpha$ can be obtained as

$$\left|\frac{\sin(\frac{p\pi}{\hat{\alpha}})}{\frac{p\pi}{\hat{\alpha}}}-\frac{2\tan(\frac{p\pi}{2})}{p\pi E[|x|^p]E[|x|^{-p}]}\right|<\varepsilon \tag{2-17}$$

To obtain $\gamma$, (2-14) is rewritten as $\hat{\gamma}=\left\{\frac{E[|x|^p]}{C(p,\hat{\alpha})}\right\}^{\hat{\alpha}/p}$.

## 2.5 Alpha-Stable Modeling of the Contourlet Subband Coefficients

In view of the non-Gaussian properties of the contourlet coefficients of images, a proper distribution to model these coefficients would be a non-Gaussian PDF. Therefore, we propose the use of the $S\alpha S$ distribution to model the distribution of the contourlet coefficients of images. To this end, we first estimate the characteristic exponent $\alpha$ values for various contourlet subbands for a given test image, when the image is decomposed

into three pyramidal levels, with eight, eight and four directions, respectively. In Table 2.1, the results obtained by estimating $\alpha$ for various test images are given. It can be seen from Table 2.1 that the value of $\alpha$ varies from 0.8 to 1.6 indicating the heavy-tailed property of the contourlet coefficients and that the distribution is not Gaussian. Thus, the distribution of the contourlet coefficients of an image can be described by the $S\alpha S$ PDF. We now examine the histograms of the actual data as well as the $S\alpha S$ , Cauchy, GG and the Laplacian density functions for a number of test images to see as to how accurately the $S\alpha S$ distribution and its Cauchy member fit the distribution of the contourlet coefficients. Figure 2.10 shows the modeling performance of the contourlet coefficients for two of the images, *Barbara* and *Baboon*. It is seen from this figure that the alpha-stable distribution, and even its Cauchy member for which the characteristic exponent is unity, can more accurately fit the empirical data than the GG and Laplacian distributions can. Moreover, to quantify the performance of the PDFs, we use the Kolmogorov-Smirnov distance (KSD) metric given by

$$\max_{f} \left| \int [P_f(f) - \widehat{P}_f(f)] df \right| \tag{2-18}$$

where $P_f(f)$ denotes the PDF of the random variable and $\widehat{P}_f(f)$ represents the PDF of the empirical data. Table 2.2 gives the values of the KSD metric for the $S\alpha S$ , Cauchy, GG, Laplacian and Levy PDFs of the image contourlet coefficients in the two finest scales. These values are obtained by averaging over a number of images. It is seen from this table that the $S\alpha S$ distribution, and even its Cauchy member, provide better fits to the empirical data than the GG, Laplacian and Levy distribution do.

Table 2.1: Characteristic exponent $\alpha$ values for the contourlet subband coefficients of various test images. Deviation from $\alpha = 2$ reveals the degree of non-Gaussianity.

| Direction | Scale | Peppers | Barbara | Baboon |
|---|---|---|---|---|
| 1 | I | 1.516 | 1.436 | 1.577 |
| 2 | | 1.506 | 1.358 | 1.514 |
| 3 | | 1.571 | 1.337 | 1.562 |
| 4 | | 1.541 | 1.308 | 1.538 |
| 1 | II | 1.330 | 1.376 | 1.471 |
| 2 | | 1.253 | 1.335 | 1.475 |
| 3 | | 1.260 | 1.392 | 1.484 |
| 4 | | 1.403 | 1.334 | 1.406 |
| 5 | | 1.407 | 1.106 | 1.342 |
| 6 | | 1.294 | 1.261 | 1.256 |
| 7 | | 1.211 | 1.203 | 1.225 |
| 8 | | 1.313 | 1.423 | 1.335 |
| 1 | III | 1.432 | 0.966 | 1.341 |
| 2 | | 1.336 | 1.024 | 1.467 |
| 3 | | 1.196 | 0.848 | 1.312 |
| 4 | | 1.216 | 1.105 | 1.523 |
| 5 | | 1.225 | 1.375 | 1.412 |
| 6 | | 1.217 | 1.264 | 1.332 |
| 7 | | 1.115 | 1.209 | 1.314 |
| 8 | | 1.388 | 1.591 | 1.425 |

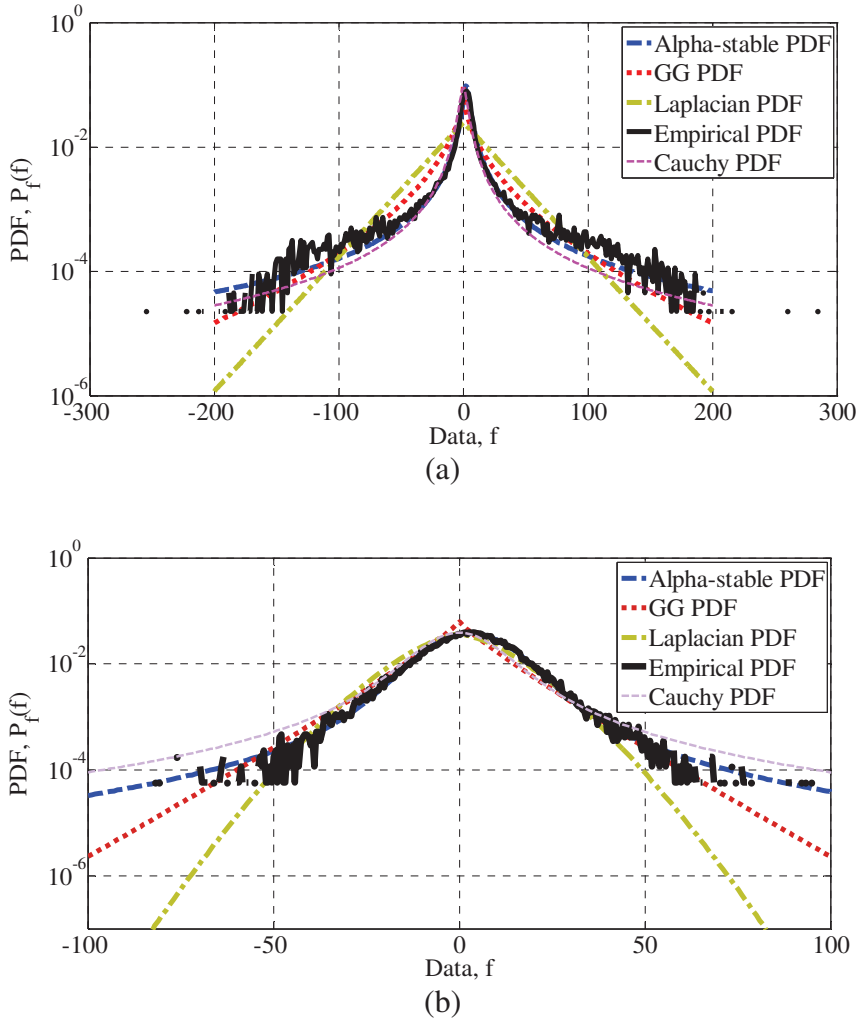


Figure 2.10. Log-scale PDFs of empirical data as well as the alpha-stable, Cauchy, GG and Laplacian distributions for two of the test images. a) *Barbara* $\alpha = 0.8$. b) *Baboon* $\alpha = 1.31$.

Table 2.2: Averaged KSD values of the alpha-stable, Cauchy, GG, Laplacian and Levy distributions in modeling the contourlet coefficients over 10,000 images, $S_{ij}$ denoting the subband in scale i and direction j.

| Direction | SαS | Cauchy | GG | Laplacian | Levy |
|---|---|---|---|---|---|
| $S_{21}$ | **0.1014** | 0.1044 | 0.1321 | 0.1234 | 0.1206 |
| $S_{22}$ | **0.1083** | 0.1097 | 0.1436 | 0.1297 | 0.1229 |
| $S_{23}$ | **0.1156** | 0.1204 | 0.1432 | 0.1357 | 0.1349 |
| $S_{24}$ | **0.0880** | 0.0923 | 0.1269 | 0.1224 | 0.1189 |
| $S_{25}$ | **0.1253** | 0.1275 | 0.1355 | 0.1291 | 0.1215 |
| $S_{26}$ | **0.1189** | 0.1229 | 0.1347 | 0.1305 | 0.1279 |
| $S_{27}$ | **0.0798** | 0.0822 | 0.1351 | 0.1403 | 0.1381 |
| $S_{28}$ | **0.0819** | 0.0835 | 0.1281 | 0.1280 | 0.1253 |
| $S_{11}$ | **0.1135** | 0.1302 | 0.1347 | 0.1468 | 0.1361 |
| $S_{12}$ | **0.0875** | 0.0881 | 0.0895 | 0.1030 | 0.1049 |
| $S_{13}$ | **0.0958** | 0.0959 | 0.0984 | 0.1117 | 0.1012 |
| $S_{14}$ | **0.0727** | 0.0734 | 0.0759 | 0.0995 | 0.0853 |
| $S_{15}$ | **0.0917** | 0.0949 | 0.0928 | 0.1073 | 0.0947 |
| $S_{16}$ | **0.0956** | 0.0957 | 0.0982 | 0.1090 | 0.0979 |
| $S_{17}$ | **0.0884** | 0.0889 | 0.0885 | 0.1063 | 0.0914 |
| $S_{18}$ | **0.0900** | 0.0904 | 0.0878 | 0.1098 | 0.0919 |

The amplitude probability density (APD) function, given by $P(|X| > x)$, is another common statistical representation of heavy-tailed signals. The APD can be used to compare the closeness of the alpha-stable Cauchy distribution to the empirical data. It can be empirically calculated by counting the data, $X$ for which $|X| > x$. It can be also evaluated theoretically from a given density function by estimating its parameters from the transformed coefficients. It is known that the alpha-stable density function has a polynomial tail $P(X > x) \sim c_\alpha x^{-\alpha}\gamma^\alpha$, $x \to \infty$, where $X$ is a non-Gaussian $S\alpha S$ random variable and $c_\alpha = \sin(\frac{\pi\alpha}{2})\frac{\Gamma(\alpha)}{\pi}$ [57]. We now examine the APD curves of the actual data as well as the $S\alpha S$, Cauchy, GG and Laplacian distributions for a number of test images. In Figure 2.11 the APD curves for two of the images, *Barbara* and *Baboon,* are depicted.

It is seen from this figure that the $S\alpha S$ distribution, and even its Cauchy member, provide better fits to the distribution of the contourlet coefficients for both the mode and the tail of the actual data than that provided by the GG and Laplacian distributions. Similar results have also been obtained for other test images.

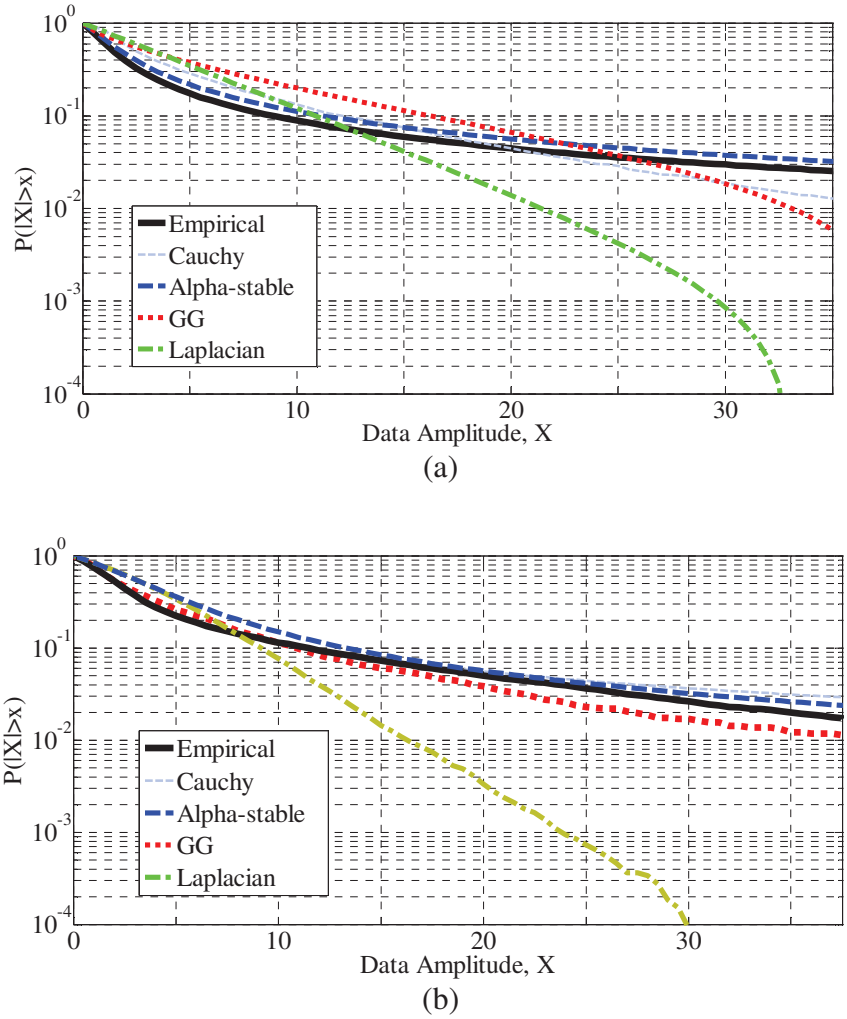


Figure 2.11. APD curves of the empirical data as well as the alpha-stable, Cauchy, GG and Laplacian distributions for two of the test images. a) *Barbara* and b) *Baboon*.

## 2.6 Summary

In this chapter, an introduction of the contourlet transform as a multiscale and multiresolution transform has been given. The contourlet transform is capable of capturing more directional information in images. The statistical properties of the contourlet coefficients of images have been carefully investigated. The empirical PDFs of the contourlet subband coefficients of images have seen to have highly non-Gaussian properties. In view of this, the alpha-stable family of distributions have been proposed to model the contourlet coefficients of images. The performance of the proposed model has been studied in detail by conducting several experiments, and comparing the results with that of the formerly-used distributions for the contourlet coefficients, namely, the generalized Gaussian and Laplacian PDFs. Simulation results have shown that the alpha-stable distribution can model the contourlet subband coefficients more accurately both subjectively in terms of the Kolmogorov-Smirnov distance and objectively by plotting the log-scale histograms. Moreover, comparing the amplitude probability density functions of the various distributions have shown that the alpha-stable distribution provides a better fit for the distribution of the contourlet coefficients than that provided by for both the mode and the tail of the actual data. The proposed alpha-stable model will be employed in developing image denoising and despeckling algorithms in the contourlet domain in Chapters 3 and 4, respectively.

# CHAPTER 3

# Image Denoising in the Contourlet Domain Using the Alpha-Stable Distribution

## 3.1 Introduction

This chapter deals with image denoising problem in the contourlet domain using the alpha-stable model proposed in Chapter 2. Image denoising is a problem of estimating the noise-free image from noisy observations while preserving the image features. The image denoising techniques may be classified into spatial [71], and transform domain [16], [18] approaches. The image denoising in the transform domain has received considerable interest in view of its improved performance in recovering signals from noisy data. In the transform domain approach, denoising process is performed on the coefficients of a transform such as the wavelet transform [17]-[20]. Donoho proposed a simple and non-probabilistic thresholding method in the wavelet domain to remove noise from an image [72]. However, it is known that the wavelet transform is good at isolating discontinuities at edge points and cannot efficiently capture the smoothness along the contour [3], [4]. In addition, applying wavelet to an image results in capturing limited directional information. In [73], the principal component analysis has been proposed to overcome the drawbacks of the wavelet transform in highly-structured images. However, these components are highly affected by the noise. In [74], the K-SVD algorithm has been proposed for the same purpose. However, exhaustive search in learned dictionaries give

rise to a time-consuming algorithm. Another class of image denoising techniques is the non-local means (NLM) algorithms [75]-[81]. The NLM algorithms estimate a pixel by a weighted average of the local and non-local pixels throughout the image and perform denoising by exploiting the natural redundancy of the patterns inside an image. In [82], similar to motion estimation algorithms, a block-wise matching has been used to preprocess the noisy image followed by a transform-domain shrinkage, known as BM3D. However, the accuracy of such block correlations is highly dependent on the noise. In [83], a patch-based locally-optimal Wiener filter has been proposed for image denoising. This method uses similar patches to estimate the filter parameters. In [84], a spatially adaptive iterative singular-value thresholding method has been proposed, which provides slightly better performance in terms of peak signal-to-noise-ratio (PSNR) than that provided by BM3D.

To enhance the sparsity and effectively capture the directional information in natural images, other multi-scale and multi-resolution transforms, such as wavelet-packets [85], complex wavelet [5], [86]-[88], curvelet [8], or contourlet [4], [11], [12], [42], [64] transforms, have been proposed. The better sparseness and decorrelation properties of these transforms result in improved image denoising schemes. In [86], [87], the image denoising is performed in complex wavelet domain, which provides more directionality than that provided by wavelet, yet it is not efficient to handle 2-D singularities. In [8], the curvelet domain image denoising has been proposed. The curvelet transform provides higher directional information of an image resulting in a denoising scheme with visually improved image and more edge preservation. However, the curvelet transform has been defined originally on concentric circles in the continuous domain and the process of

discretization is complex and time-consuming. Therefore, to overcome these disadvantages of the curvelet transform, the contourlet transform has been proposed. Due to the various properties of this transform, discussed in Chapter 2, image denoising in the contourlet domain is superior to that in other multiscale transform domains. Most of the image denoising algorithms in the contourlet domain have been developed based on the thresholding or shrinkage functions [9], [11]. In recent years, statistical models have been adopted for the transform domain coefficients in which the image and noise are modeled as random fields and Bayesian methods are employed to develop shrinkage functions for estimation of the noise-free coefficients from the noisy observations. It is to be noted that the prior distributions for the original image and the noise have considerable effect on the performance of the denoising algorithm. Several prior distributions have been employed to characterize the transform coefficient properties such as their sparsity, i.e., having a large number of small coefficients along with a small number of large coefficients [17]-[21], [88]. It has been shown in Chapter 2 that that the contourlet-domain subband decomposition of images have significant non-Gaussian statistics that are best described by the alpha-stable family.

In this chapter, a new image denoising technique in the contourlet domain based on the alpha-stable family of distributions as a prior for the contourlet coefficients is proposed [89]. Bayesian MMAE and MAP estimators using the alpha-stable distribution are developed to obtain the noise-free contourlet coefficients. The contourlet coefficients are first modelled by the univariate alpha-stable distribution. Then, across-scale dependencies of the contourlet coefficients are taken into account by employing the bivariate alpha-stable distribution to capture these dependencies. In order to estimate the

parameters of the model more accurately, a spatially-adaptive method based on the fractional lower-order moments is proposed. An extension of the proposed denoising scheme to color images is also carried out. Several experiments are conducted to evaluate the performance of the proposed denoising scheme and to compare it with those of the current state-of-the-art techniques. The estimated images are compared with the original ones in terms of the peak signal-to-noise-ratio (PSNR) and mean structural similarity (MSSIM) index, as well as in terms of the visual quality of the denoised images.

## 3.2 Denoising Scheme in the Contourlet Domain

It is known that the use of downsamplers and upsamplers in the structure of the contourlet transform makes it shift-variant, which may produce artifacts around the singularities, e.g., edges. In view of this, in image denoising, the cycle spinning method [11], [90] is employed to compensate for the lack of translation invariance. It is a simple, yet efficient, method to improve the denoising performance for a shift-variant transform. In fact, the cycle spinning is to average out the translation dependence of the subsampled contourlet transform and can be expressed as

$$\hat{I} = \frac{1}{M \times N} \sum_{m=1}^{M} \sum_{n=1}^{N} ICT(S_{-m,-n}(h(CT(S_{m,n}(I))))) \tag{3-1}$$

where $I$ and $\hat{I}$ are noisy and denoised images, CT and ICT are the contourlet transform and its inverse, respectively, $S_{m,n}$ is the cycle spinning operator with $(m,n)$ as shifts in

the horizontal and vertical directions, and $h$ is the denoising operator in the contourlet domain [90].

Figure 3.1 depicts a parent-children relationship for a three-scale contourlet decomposition with eight directions in each scale. The across scale dependencies between parents and children play an important role in the modeling of the contourlet coefficients. In view of this, we also model the contourlet coefficients of an image using the bivariate alpha-stable distribution not only to capture the heavy tails of the distribution of the contourlet coefficients, but also to take into account the contourlet coefficient dependencies across scales. Similar to the univariate $S\alpha S$ distribution, a zero-mean bivariate $S\alpha S$ is characterized by its characteristic function given by

$$\varphi_{\alpha,\gamma}(\omega_1,\omega_2) = \exp\left(-\gamma\left|\sqrt{\omega_1^2+\omega_2^2}\right|^{\alpha}\right) \tag{3-2}$$

Equivalently, the bivariate $S\alpha S$ PDF is obtained as

$$f_{\alpha,\gamma}(x_1,x_2) = \frac{1}{4\pi^2}\int_{-\infty}^{\infty}\int_{-\infty}^{\infty}\exp\left(j\gamma\left|\sqrt{\omega_1^2+\omega_2^2}\right|^{\alpha}(\omega_1 x_1+\omega_2 x_2)\right)d\omega_1 d\omega_2 \tag{3-3}$$

Figure 3.2 shows the joint histogram of the contourlet coefficients across scales for one of the test images, *Barbara*, along with a possible configuration of the bivariate $S\alpha S$ PDF. It can be seen from this figure that the bivariate $S\alpha S$ PDF can suitably model the parent-children relationship of the contourlet coefficients across two consecutive scales. Figure 3.3 shows the distribution of the coefficients conditioned on its parent value in the

four directional subbands of the finest scale for one of the test images, *Barbara* image. It is seen from this figure that the conditional histograms for various directional subbands resemble a bow-tie shape indicating the dependency between the children and their parents. Therefore, in our image denoising task, we model contourlet coefficients of an image using the bivariate alpha-stable distribution in order to not only capture the heavy tails of the distribution of the contourlet coefficients, but also to take into account the contourlet coefficient dependencies across scales.

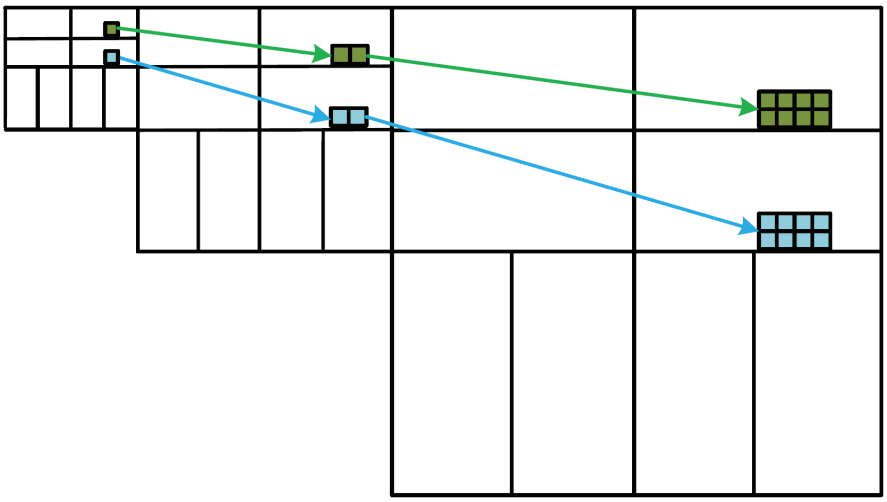

Figure 3.1. Parent-children relationship for a three-scale contourlet decomposition with eight directions in each scale.

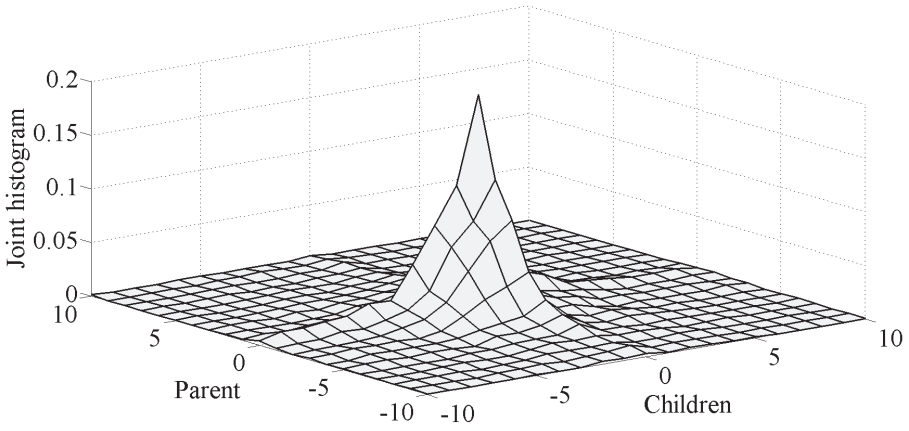


(a)

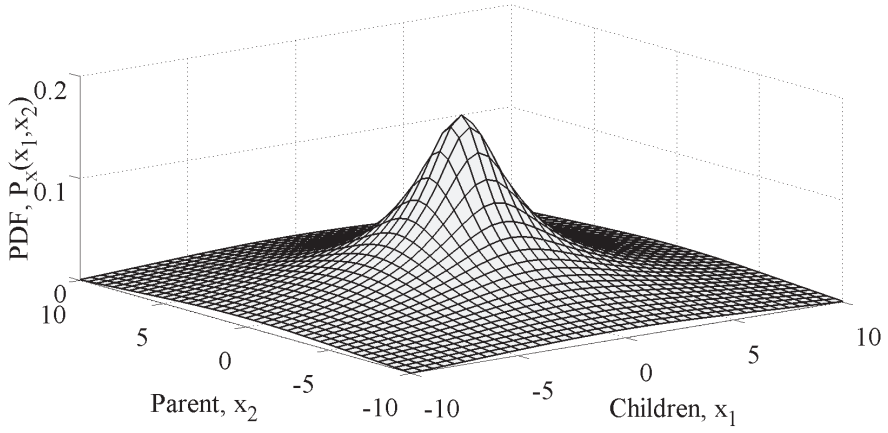


(b)

Figure 3.2. (a) Empirical joint child-parent histogram across two scales of the contourlet coefficients for the fourth direction of the *Barbara* image. b) The configuration of the bivariate $S\alpha S$ distribution.

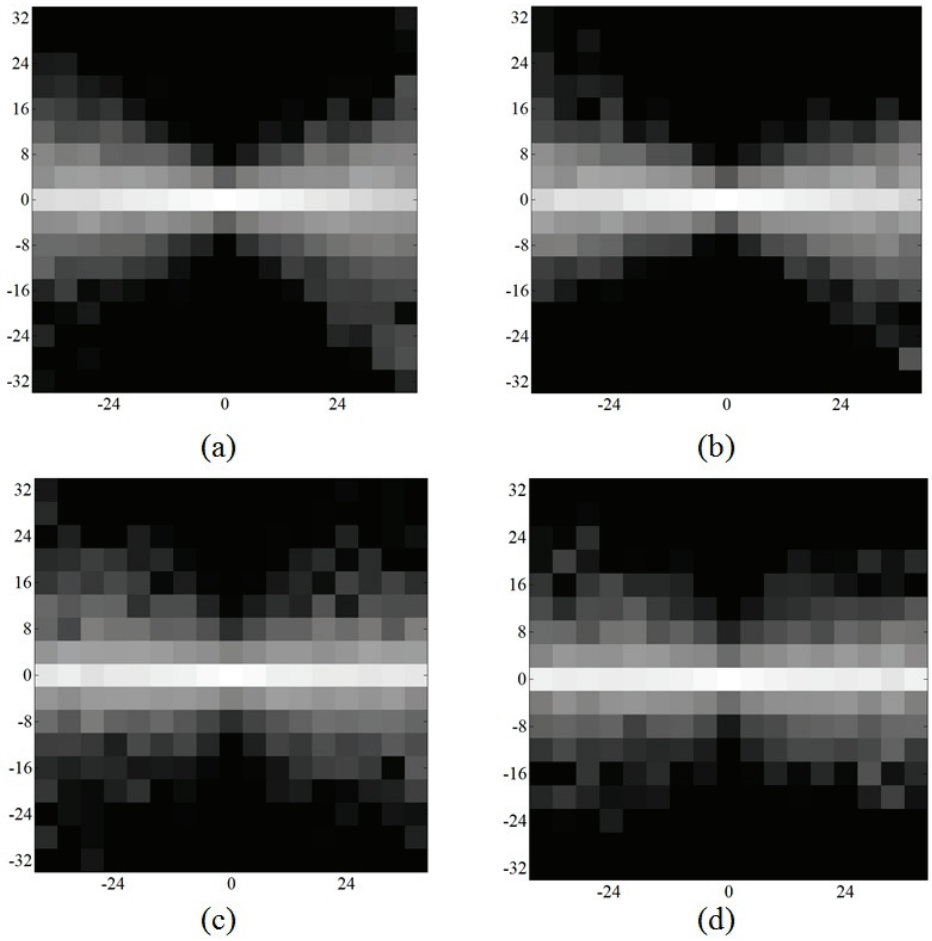


Figure 3.3. Distribution of the contourlet coefficients (vertical axis) conditioned on the corresponding coarser-scale coefficient, i.e., parent coefficient (horizontal axis), in the four directional subbands of the *Barbara* image; A normalized pair of parent and child coefficients is considered.

Let a noise-free image $X$ be contaminated by an additive white Gaussian noise $N$ with a zero-valued mean and known standard deviation $\sigma_\eta$. The corresponding noisy image is denoted by $Y$. We then have

$$Y = X + N \tag{3-4}$$

The contourlet transform is applied to the noisy image. Suppose that a noisy image is decomposed into $j = 1,...,J$ scales and $d = 1,...,D$ direction subbands by the contourlet transform. We have

$$y_j^d(m,n) = x_j^d(m,n) + \eta_j^d(m,n) \tag{3-5}$$

where $y_j^d(m,n)$, $x_j^d(m,n)$ and $\eta_j^d(m,n)$ denote the $(m,n)^{th}$ contourlet coefficient at scale $j$ and direction $d$ of the contourlet transform of $Y$, $X$ and $N$, respectively. For notational simplicity, we drop the subscripts and indices as well and use henceforth $y$, $x$ and $\eta$.

### 3.2.1. Bayesian MAP Estimator for Gaussian Noise

The Bayesian method imposes a prior model on the contourlet coefficients that describe their distribution. In this work, we propose the $S\alpha S$ distribution as a prior for modeling the contourlet coefficients $x$, corresponding to a specific subband of a noise-free image. We assume that the probabilistic model associated with the noisy data $y$ conditionally on $x$ is Gaussian

$$y \mid x \sim N(x, \mu = 0, \sigma_\eta^2) \tag{3-6}$$

The noise distribution can be expressed as

$$P_\eta(y - x) = \frac{1}{\sqrt{2\pi}\sigma_\eta} \exp\left\{ -\frac{(y-x)^2}{2\sigma_\eta^2} \right\} \tag{3-7}$$

For estimating the original image, i.e., the noise free coefficients $x$, given the noisy observation $y$, we employ the MAP estimator. Using the Bayes rule, the MAP estimator is defined by

$$\begin{aligned} \hat{x} &= \arg\max_x P_{x|y}(x \mid y) \\ &= \arg\max_x P_{y|x}(y \mid x) P_x(x) \\ &= \arg\max_x P_\eta(y - x) P_x(x) \end{aligned} \tag{3-8}$$

where $P_x(x)$ is the PDF of the contourlet coefficients of the noise-free image. To obtain the MAP estimate, after inserting $P_\eta(\eta)$ into (3-8), the derivative of the logarithm of the argument in (3-8) is set to zero resulting in

$$\frac{(\hat{x} - y)}{\sigma_\eta^2} + \frac{\partial}{\partial y}(-\ln(P_x(y))) = 0 \tag{3-9}$$

We now need a model for the distribution of the contourlet coefficients $P_x(x)$. At this stage, we consider the following three cases.

Case 1: $P_x(x) \sim N(0,\sigma^2)$, where $\alpha = 2$ and $\sigma^2$ is the variance of the Gaussian PDF.

Case 2: $P_x(x) = \sqrt{\frac{\gamma}{2\pi}} \frac{e^{\frac{-\gamma}{2x}}}{x^{1.5}}$, where $\alpha = 0.5$ and $\gamma$ is the dispersion parameter of the Levy PDF.

Case 3: $P_x(x) = \frac{\gamma}{\pi(x^2 + \gamma^2)}$, where $\alpha = 1$ and $\gamma$ is the dispersion parameter of the Cauchy PDF.

Case 4: Best-fit $S\alpha S$ for which there is no closed-form PDF.

It should be noted that Cases 1 to 3 are the special cases of the alpha-stable PDF having closed-form expressions [57]. For Case 1, the estimate $\hat{x}$ for the Gaussian data is obtained from (3-9) as

$$\hat{x}_i(y) = \frac{\sigma_x^2}{\sigma_x^2 + \sigma_\eta^2} y \tag{3-10}$$

which is the minimum mean square error (MMSE) solution for the Bayesian estimator. For Cases 2 to 4, the Bayesian MAP estimator for non-Gaussian data is obtained from (3-9) as

$$\hat{x}(y) = sign(y) \max(0, | y | - \sigma_\eta^2 | M |) \tag{3-11}$$

where $M = \frac{\partial \ln P_x(y)}{\partial y}$. It may be mentioned that for Case 3, the Cauchy PDF, $M = \frac{2y}{\gamma^2 + y^2}$, while for Case 2, the Levy PDF, one needs to solve a cubic function as

$x^3 + ax^2 + bx + c = 0$, where $a = -y$, $b = \frac{-3\sigma_\eta^2}{2}$ and $c = \frac{\gamma\sigma_\eta^2}{2}$. In the case of the best-fit $S\alpha S$, we have to numerically compute the Bayesian MAP estimator.

### 3.2.2. Bayesian MAP Estimator for Non-Gaussian Noise

We also develop the MAP estimator using zero-mean, independent and identically distributed non-Gaussian noises modelled by the Maxwell and Rayleigh distributions given by

$$P_\eta(\eta) = \begin{cases} \sqrt{\frac{2}{\pi}} \frac{\eta^2}{v^3} \exp\left(-\frac{\eta^2}{2v^2}\right), & \textit{Maxwell} \\ \frac{2|\eta|}{\sigma_\eta^2} \exp\left(-\frac{\eta^2}{\sigma_\eta^2}\right), & \textit{Rayleigh} \end{cases} \tag{3-12}$$

where $v = \frac{\sigma_\eta}{\sqrt{3}}$. The noise standard deviation $\sigma_\eta$ can be estimated by applying the robust median absolute deviation method in the finest subband of the observed noisy coefficients. For the case of α=1, Cauchy member of the alpha-stable distribution, due to having a closed form expression for its PDF, the Bayesian MAP estimator is derived after some manipulations as a root of the following quadratic function

$$\hat{x}^4 + a\hat{x}^3 + b\hat{x}^2 + c\hat{x} + d = 0 \tag{3-13}$$

where for the Maxwell noise

$$
\begin{aligned}
a &= -2y, & b &= \gamma^2 + y^2 \\
c &= -2y\gamma^2 - \frac{2}{3}y\sigma_\eta^2, & d &= -\frac{2\sigma_\eta^2\gamma^2}{3} + \gamma^2 y^2
\end{aligned}
\tag{3-14}
$$

and for the Rayleigh noise

$$
\begin{aligned}
a &= -2y, & b &= \frac{\sigma_\eta^2}{2} + \gamma^2 + y^2 \\
c &= -2y\gamma^2 - y\sigma_\eta^2, & d &= -\frac{\sigma_\eta^2\gamma^2}{2} + \gamma^2 y^2
\end{aligned}
\tag{3-15}
$$

The quadratic function in (3-13) can be solved by using Ferrari's method as

$$
\left(\hat{x}^2 + \frac{1}{2}a\hat{x} + \frac{1}{2}t_0\right)^2 = \left(\sqrt{\hat{x}\,t_0 + \frac{1}{4}a^2 - b} \pm \sqrt{\frac{1}{4}t_0^2 - d}\right)^2 \tag{3-16}
$$

By solving two quadratic functions in (3-16), $\hat{x}$ is found as

$$
\begin{aligned}
\hat{x} = &-\frac{a}{4} \pm \frac{1}{2}\sqrt{\frac{a^2}{4} - b + t_0} \\
&+ \frac{1}{2}\sqrt{\left(\frac{a}{2} \pm \sqrt{\frac{a^2}{4} - b + t_0}\right)^2 - 2t_0 \pm \sqrt{\frac{t_0^2}{4} - d}}
\end{aligned}
\tag{3-17}
$$

where $t_0$ is a root of the cubic function

$$
t^3 - bt^2 + (ac - 4d)t + (4bd - a^2 d - c^2) = 0 \tag{3-18}
$$

as

$$t_0 = \sqrt[3]{-\frac{q}{2}+\sqrt{D}} + \sqrt[3]{-\frac{q}{2}-\sqrt{D}} + \frac{b}{3} \tag{3-19}$$

where

$$\begin{aligned} q &= \frac{b(ac-4d)}{3} - \frac{2b^3}{27} - a^2 d - c^2 + 4bd \\ D &= \frac{(ac-4d-\frac{b^3}{3})}{27} - \frac{q^3}{4} \end{aligned} \tag{3-20}$$

It should be noted that for the general case (best-fit α), and the Bayesian MMAE estimator, we have numerically estimated the noise-free coefficients.

### 3.2.3. Bayesian MMAE Estimator

We now develop a Bayesian MMAE estimator, using the proposed $S\alpha S$ prior, by minimizing the mean absolute error between the observed data and the estimated one. Since the coefficients in the approximation subband carry most of the information about the signal to be recovered, we leave them unchanged, and apply the Bayesian MMAE estimator to the coefficients of the detail subbands. The Bayesian MMAE estimator of $x$, given a noisy observation $y$, is given by

$$\hat{x}(y) = \int x P_{x \mid y}(x \mid y)\, dx \tag{3-21}$$

According to the Bayesian rule, $P_{x|y}(x \mid y)$ can be written as

$$P_{x|y}(x \mid y) = \frac{P_{y|x}(y \mid x) P_x(x)}{\int P_{y|x}(y \mid x) P_x(x)\, dx} \tag{3-22}$$

where $P_x(x)$ is the prior model for the contourlet coefficients of a noise-free image. Substituting (3-22) into (3-21), we obtain

$$\begin{aligned} \hat{x}(y) &= \frac{\int x P_{y|x}(y \mid x) P_x(x)\, dx}{\int P_{y|x}(y \mid x) P_x(x)\, dx} \\ &= \frac{\int x P_{\eta}(\eta) P_x(x)\, dx}{\int P_{\eta}(\eta) P_x(x)\, dx} \end{aligned} \tag{3-23}$$

where $P_{\eta}(\eta)$ is the PDF of the noise. In order to estimate the noise-free coefficients, we consider the four cases mentioned above, namely, the Gaussian, Cauchy, Levy and the best-fit $S\alpha S$ distributions. It should be noted that in case of the general best-fit $S\alpha S$, the Bayesian MMAE estimator has to be computed by direct numerical integration [57], [58]. To lower the computational complexity, we resort to the shrinkage function in terms of a linear convolution as

$$\hat{x}(y) = \frac{P_{\eta}(y) * x P_x(x)}{P_{\eta}(y) * P_x(x)} \tag{3-24}$$

where * is the convolution operator. Therefore, instead of employing direct numerical integration for each coefficient, the Bayesian MMAE estimator of the coefficients of a subband are obtained using the cubic spline interpolation method when the convolution operation is carried out at a limited number of points using the fast Fourier transform (FFT) algorithm as

$$\hat{x}(y) = \frac{F^{-1}\left\{F\left\{P_{\eta}(y)\right\} F\left\{x\, P_{x}(x)\right\}\right\}}{F^{-1}\left\{F\left\{P_{\eta}(y)\right\} F\left\{P_{x}(x)\right\}\right\}} \tag{3-25}$$

where $F^{-1}$ and $F$ denote the FFT and inverse FFT transforms, respectively. A consequence of using (3-23) is reducing the computational effort in obtaining the MMAE estimates.

### 3.2.4. Parameter Estimation

In order to employ the $S\alpha S$ prior in denoising, first it is needed to estimate the parameters $\alpha$ and $\gamma$ from the noisy coefficients. As mentioned in Chapter 2, there are several estimators, that can be used to estimate the parameters of the alpha-stable distribution, such as the characteristic function-based estimators including regression-type [65] and methods based on minimum distance [91], moments [91], quantiles [60], fractional lower order moments [70], [92] and maximum likelihood (ML) [93], [94]. Among these, the ML estimator [93] has been shown to provide an efficient estimate of the parameters. We now propose a method for parameter estimation that uses spatially-adaptive fractional lower order moments. It has been shown in [15] that when the number of scales is increased, the distribution of the contourlet coefficients is close to the Gaussian distribution. In other words, the distribution of the contourlet coefficients of images is locally Gaussian. In view of this, the dispersion parameter $\gamma$ of an alpha-stable distribution can be estimated as $\gamma = \frac{\sigma^2}{2}$, in which $\sigma^2$ is the variance of the Gaussian

distribution in a small spatial window. In order to estimate $\sigma^2$ in a given scale $j$, we employ the spatially-adaptive technique [18] as

$$\sigma_j^2(m,n) = \max\left( \sum_{i \in S} \frac{y_j^2(i)}{l^2} - \sigma_{\eta,j}^2, 0 \right) \tag{3-26}$$

where $S$ is a square-shaped window of size $l \times l$. The characteristic exponent $\alpha$ is then estimated using the fractional lower order moment (FLOM) method. The moments of order less than $\alpha$ for a $S\alpha S$ random variable [92], [95], [96] is defined as

$$E\left[ |X|^p \right] = \frac{\gamma^{p/\alpha} \Gamma(1 - \frac{p}{\alpha})}{\cos(\frac{p\pi}{2}) \Gamma(1-p)} \tag{3-27}$$

in which $-1 < p < \alpha \le 2$. It should be noted that the choice of the order $p$ of the fractional moment is arbitrary. However, as shown in [97], the best choice is $p \approx \frac{\alpha}{3}$. In order to estimate the standard deviation of the noise $\sigma_\eta$ from the noisy contourlet coefficients, the Donoho's estimator [72] is modified in the finest decomposition scale as

$$\hat{\sigma}_\eta = \frac{1}{0.6745} \sum_{d=1}^{D} \left( MAD\{S_{1,d}\} \right) \tag{3-28}$$

where MAD is the *median absolute deviation* and $S_{1,d}$ denotes the $d$ th directional subband coefficients in the finest scale. The contourlet domain image denoising algorithm using the alpha-stable distribution can be summarized as follow:

Step 1: Apply the contourlet transform to the noisy image.

Step 2: Estimate the parameters $\gamma$, $\alpha$ and $\sigma_\eta$ from the noisy coefficients.

Step 3: Obtain an estimation of the noise-free coefficients by using the Bayesian MAP (3-11) or MMAE (3-23) estimator.

Step 4: Apply the inverse contourlet transform to the estimates obtained in Step 3.

The above method of denoising an image is also shown in the form of a block diagram in Figure 3.4.

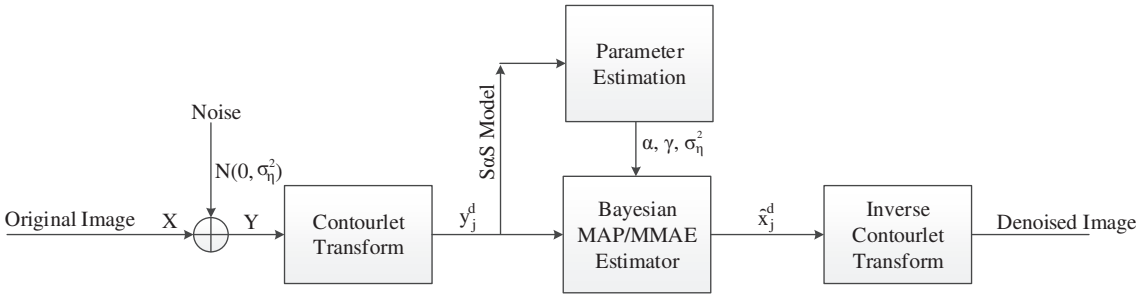


Figure 3.4. Block diagram of the proposed denoising algorithm in the contourlet domain.

## 3.3 Experimental Results

The performance of the contourlet domain denoising method is evaluated by conducting experiments using set of images obtained from [98], and then compared to that of the many of the state-of-the-art techniques. The experiments are performed on images corrupted with Gaussian noise of standard deviation, $\sigma_\eta$ varying from 10 to 40. The noisy images are decomposed by the contourlet transform into three scales with eight directions in each scale. Note that any further decomposition beyond these levels does not produce a significant increase in the denoising performance. We use the 9-7 bi-orthogonal filters for both the multi-scale and multi-directional decomposition stages. Since the contourlet transform is not shift-invariant, the denoised image is affected by the pseudo-Gibbs phenomena, resulting in artifacts in smooth regions and ringing effect around the edges. To overcome this problem, as discussed in Section 3.2, we employ the cycle spinning mode by averaging the result of the contourlet shrinkage method over all the circulant shifts of the input noisy image. The PSNR, in decibels, and MSSIM index measure are used to provide quantitative evaluations of the algorithm. It should be noted that for a particular noise level, the PSNR value is calculated by repeating the experiment ten times and then averaging over these values.

Tables 3.1 and 3.2 give the PSNR values obtained for various estimators using the alpha-stable family of distributions including the bivariate and univariate $S\alpha S$ distributions and its Cauchy member ($\alpha$=1) in the wavelet and contourlet domains for two of the test images, namely, *Barbara* and *Peppers*, respectively. From these tables, it is seen that the performance of the denoising algorithm in the contourlet domain is better than that obtained in the wavelet domain, irrespective of the distribution employed. Further, it is

observed that the proposed denoising scheme using the bivariate $S\alpha S$ distribution provides higher PSNR values than that provided by using the univariate $S\alpha S$ . Finally, it is noted that the bivariate alpha-stable distribution in the contourlet domain using the MMAE estimator (CT-Bi-$S\alpha S$ -MMAE) provides the highest PSNR values for all the noise levels considered. We further compare the performance of the $S\alpha S$ prior to that of the GG, Cauchy, Levy and Laplacian distributions in our proposed denoising scheme. Table 3.3 gives the PSNR values obtained using the proposed method when different priors are used for two of the test images, namely, *Barbara* and *Peppers*. It is seen from this table that the $S\alpha S$ distribution provides a better denoising performance than the other distributions do.

Moreover, to investigate the performance of the proposed denoising scheme on textured images, we apply our proposed denoising algorithm to a set of textured images [99] and the results are given in Table 3.4. It is seen from this table that the proposed algorithm performs very well even for images with high textures.

Table 3.1: PSNR values obtained using denoising methods employing the alpha-stable family of distributions in wavelet (WT) and contourlet (CT) domains for *Barbara* image.

| | Barbara | | | | | |
|---|---|---|---|---|---|---|
| | 10 | 15 | 20 | 25 | 30 | 40 |
| Noisy | 28.13 | 24.61 | 22.13 | 20.17 | 18.63 | 16.14 |
| WT-Cauchy | 32.22 | 30.41 | 28.42 | 26.87 | 24.61 | 22.64 |
| CT-Cauchy | 32.71 | 30.66 | 28.74 | 26.99 | 25.16 | 22.97 |
| WT-SαS-MAP | 32.60 | 30.46 | 28.56 | 26.31 | 24.93 | 22.74 |
| CT-SαS-MAP | 32.97 | 31.01 | 29.21 | 28.09 | 26.23 | 24.03 |
| WT-SαS-MMAE | 32.78 | 30.77 | 28.97 | 27.10 | 25.39 | 23.11 |
| CT-SαS-MMAE | 33.62 | 31.34 | 29.47 | 28.53 | 26.74 | 24.95 |
| WT-Bi-SαS-MAP | 33.34 | 31.17 | 29.22 | 28.22 | 26.51 | 24.83 |
| CT-Bi-SαS-MAP | 34.61 | 32.86 | 31.19 | 30.23 | 27.84 | 26.58 |
| WT-Bi-SαS-MMAE | 33.70 | 31.42 | 29.77 | 28.76 | 26.98 | 25.74 |
| CT-Bi-SαS-MMAE | **34.89** | **33.03** | **31.65** | **30.61** | **28.24** | **26.97** |

Table 3.2: PSNR values obtained using denoising methods employing the alpha-stable family of distributions in wavelet (WT) and contourlet (CT) domains for *Peppers* image.

| | Peppers | | | | | |
|---|---|---|---|---|---|---|
| | 10 | 15 | 20 | 25 | 30 | 40 |
| Noisy | 28.13 | 24.61 | 22.15 | 20.17 | 18.63 | 16.13 |
| WT-Cauchy | 32.13 | 30.05 | 28.24 | 26.56 | 24.39 | 22.55 |
| CT-Cauchy | 32.45 | 30.35 | 28.33 | 26.79 | 25.01 | 22.67 |
| WT-SαS-MAP | 32.31 | 30.21 | 28.25 | 26.74 | 24.97 | 22.57 |
| CT-SαS-MAP | 32.65 | 30.80 | 29.10 | 27.92 | 25.94 | 23.19 |
| WT-SαS-MMAE | 32.60 | 30.62 | 28.76 | 27.28 | 25.22 | 23.19 |
| CT-SαS-MMAE | 33.41 | 31.13 | 29.34 | 28.23 | 26.19 | 24.76 |
| WT-Bi-SαS-MAP | 33.02 | 30.89 | 29.14 | 28.01 | 26.04 | 24.66 |
| CT-Bi-SαS-MAP | 34.29 | 32.55 | 30.51 | 29.02 | 27.51 | 26.35 |
| WT-Bi-SαS-MMAE | 33.41 | 31.06 | 29.51 | 28.34 | 26.56 | 25.11 |
| CT-Bi-SαS-MMAE | **34.59** | **32.73** | **30.78** | **29.22** | **28.10** | **26.78** |

Table 3.3: PSNR values obtained using the proposed denoising method with different priors for two of the test images, *Barbara* and *Peppers*, when $\sigma_\eta$=10.

| | SαS | | Cauchy | | GG | | Laplacian | | Levy | |
|---|---|---|---|---|---|---|---|---|---|---|
| | MAP | MMAE | MAP | MMAE | MAP | MMAE | MAP | MMAE | MAP | MMAE |
| Barbara | 32.97 | 33.62 | 32.13 | 32.71 | 31.98 | 32.48 | 31.51 | 31.83 | 31.46 | 31.75 |
| Peppers | 32.65 | 33.41 | 32.01 | 32.45 | 31.75 | 32.22 | 31.21 | 31.60 | 31.26 | 31.64 |
| | Bi-SαS | | Bi-Cauchy | | Bi-GG | | Bi-Laplacian | | Bi-Levy | |
| | MAP | MMAE | MAP | MMAE | MAP | MMAE | MAP | MMAE | MAP | MMAE |
| Barbara | 34.61 | **34.89** | 33.45 | 33.96 | 33.15 | 33.69 | 32.74 | 33.10 | 33.23 | 33.64 |
| Peppers | 34.29 | **34.59** | 33.13 | 33.61 | 32.68 | 33.18 | 32.24 | 32.53 | 32.87 | 33.29 |

Table 3.4: Averaged PSNR values obtained using the proposed denoising method over 60 textured images [99], when $\sigma_\eta$=20.

| SαS | | Cauchy | | GG | | Laplacian | |
|---|---|---|---|---|---|---|---|
| MAP | MMAE | MAP | MMAE | MAP | MMAE | MAP | MMAE |
| 28.39 | 29.02 | 28.04 | 28.65 | 28.01 | 28.58 | 27.34 | 28.11 |
| Bi-SαS | | Bi-Cauchy | | Bi-GG | | Bi-Laplacian | |
| MAP | MMAE | MAP | MMAE | MAP | MMAE | MAP | MMAE |
| 29.84 | 30.11 | 29.35 | 29.76 | 29.26 | 29.69 | 28.87 | 29.27 |

In order to compare the denoising performance using the proposed parameter estimation method discussed in Section 3.2.4 with that using the ML method, the corresponding PSNR values are obtained and presented in Table 3.5 for various noise levels. It is seen from this table that the proposed method provides higher PSNR values as compared to that provided by the ML method, irrespective of whether a MAP or an MMAE estimator is employed. The effect of window size on images of various sizes in parameter estimation is now investigated. Table 3.6 gives the PSNR values obtained using the proposed denoising method for a few of the test images, namely, *Lena*, *Boat*, *Peppers* and *Couple*. It can be seen from this table that the window size of the local variance has an impact on the overall denoising performance. It is observed that, in general, for images of size 1024×1024, 512×512 and 256×256, windows of size of 15×15, 7×7 and 5×5, respectively, give the best denoising results in terms of the PSNR values. Similar results are also observed for other test images. We now compare the performance of the CT-Bi-$S\alpha S$ -MMAE denoising method, to that of a large number of existing methods, namely, Visu-shrink (hard) [71], Bayes-shrink [16], HMT [19], LPG-PCA [73], K-SVD [74], NSCCT-NLM [75], R-NL [76], NHDW[77], LSSC [78], CASD [79], TDNL [80], NCSR [81], BM3D [82], PLOW [83], SAIST [84], WPshrink [85], BLS-GSM [17], CW-Bi-shrink [86], Surelet [100], MGGD [101], SURE-shrink [102], CW-CGSM [103], NSCT-LAS [104], Trivariate [105], TIDFT [106], LAWMAP [107], Fuzzy-shrink [108], NSSTM [109], MMSE-MAP [110], PID [111], DDID [112], NLB [113], EPLL [114] and GNW [115].

Table 3.5: PSNR values obtained using the ML method and the proposed parameter estimation method for various noise levels.

| | | 10 | | 20 | | 30 | | 40 | |
|---|---|---|---|---|---|---|---|---|---|
| | | ML | Prop. | ML | Prop. | ML | Prop. | ML | Prop. |
| Barbara | MMAE | 34.73 | 34.89 | 31.49 | 31.65 | 28.09 | 28.24 | 26.53 | 26.97 |
| | MAP | 34.53 | 34.61 | 31.03 | 31.19 | 27.58 | 27.84 | 26.21 | 26.58 |
| Peppers | MMAE | 34.48 | 34.59 | 30.63 | 30.87 | 27.83 | 28.10 | 26.35 | 26.78 |
| | MAP | 34.21 | 34.29 | 30.34 | 30.51 | 27.22 | 27.51 | 26.10 | 26.35 |

Table 3.6: PSNR values obtained using denoising methods with various windows and image sizes.

| | 3×3 | 5×5 | 7×7 | 9×9 | 11×11 | 15×15 | 19×19 |
|---|---|---|---|---|---|---|---|
| Lena 256×256 | 34.61 | **34.82** | 34.75 | 34.64 | 34.49 | 34.22 | 34.01 |
| Lena 512×512 | 35.76 | 35.91 | **36.01** | 35.98 | 35.92 | 35.84 | 35.70 |
| Lena 1024×1024 | 36.78 | 37.04 | 37.52 | 37.74 | 37.85 | **37.93** | 37.82 |
| Boat 256×256 | 32.82 | **32.89** | 32.74 | 32.60 | 32.47 | 32.21 | 32.07 |
| Boat 512×512 | 33.65 | 33.87 | **34.05** | 33.93 | 33.81 | 33.56 | 33.40 |
| Boat 1024×1024 | 34.24 | 35.20 | 35.62 | 35.80 | 35.89 | **35.96** | 35.82 |
| Peppers 256×256 | 33.12 | **33.17** | 33.09 | 32.99 | 32.85 | 32.77 | 32.64 |
| Peppers 512×512 | 34.32 | 34.47 | **34.59** | 34.51 | 34.85 | 34.20 | 34.07 |
| Peppers 1024×1024 | 35.51 | 35.64 | 35.79 | 35.91 | 36.05 | **36.14** | 36.02 |
| Couple 256×256 | 33.00 | **33.06** | 32.95 | 32.87 | 32.73 | 32.61 | 32.49 |
| Couple 512×512 | 33.98 | 34.05 | **34.10** | 34.03 | 33.96 | 33.84 | 33.71 |
| Couple 1024×1024 | 35.24 | 35.39 | 35.51 | 35.65 | 35.77 | **35.87** | 35.76 |

Table 3.7: PSNR values obtained using various denoising methods for three of the test images, *Barbara*, *Boat* and *Lena*.

| | Barbara | | | | Boat | | | | Lena | | | |
|---|---|---|---|---|---|---|---|---|---|---|---|---|
| Visu-shrink | 26.87 | 26.99 | 26.31 | 25.77 | 28.61 | 26.90 | 25.82 | 25.03 | 30.65 | 28.89 | 27.76 | 27.02 |
| Sure-shrink | 30.21 | 28.34 | 27.02 | 25.84 | 31.83 | 29.88 | 28.55 | 27.50 | 33.42 | 31.50 | 30.17 | 29.18 |
| Bayes-shrink | 30.86 | 28.51 | 27.13 | 26.01 | 31.77 | 29.84 | 28.45 | 27.37 | 33.29 | 31.38 | 30.14 | 29.19 |
| HMT | 31.36 | 29.23 | 27.80 | 25.99 | 32.25 | 30.28 | 28.81 | 27.65 | 33.81 | 31.73 | 30.36 | 29.21 |
| LAWMAP | 32.57 | 30.19 | 28.59 | 27.42 | 32.22 | 30.27 | 28.97 | 27.88 | 34.31 | 32.36 | 31.01 | 29.98 |
| Surelet | 32.15 | 29.61 | 27.93 | 26.65 | 32.67 | 30.55 | 29.14 | 28.09 | 34.56 | 32.68 | 31.37 | 30.36 |
| GNW | 32.41 | - | 27.64 | - | - | - | - | - | 33.96 | - | 30.62 | - |
| CW-Bi-shrink | 33.35 | 31.31 | 29.80 | 28.61 | 33.10 | 31.36 | 30.08 | 29.06 | 35.21 | 33.50 | 32.28 | 31.34 |
| LPG-PCA | 32.50 | - | 28.50 | - | - | - | - | - | 33.70 | - | 29.70 | - |
| Trivariate | 33.66 | 31.49 | 29.97 | 28.78 | 33.23 | 31.35 | 30.01 | 28.98 | 35.32 | 33.60 | 32.36 | 31.38 |
| TIDFT | 33.81 | - | 30.37 | - | - | - | - | - | 35.70 | - | 32.98 | - |
| MGGD | - | - | - | - | 33.31 | 31.46 | 30.14 | 29.12 | 35.35 | 33.70 | 32.46 | 31.48 |
| CW-CGSM | 34.01 | 31.79 | 30.25 | 29.07 | 33.49 | 31.51 | 30.13 | 29.09 | 35.50 | 33.72 | 32.40 | 31.35 |
| BLS-GSM | 34.03 | 31.86 | 30.32 | 29.13 | 33.58 | 31.70 | 30.38 | 29.37 | 35.61 | 33.90 | 32.66 | 31.69 |
| NSCT-LAS | 34.09 | - | 30.60 | - | - | - | - | - | 34.46 | - | 32.50 | - |
| K-SVD | 34.42 | 32.37 | 30.83 | 29.60 | 33.64 | 31.73 | 30.38 | 29.37 | 35.61 | 33.90 | 32.66 | 31.69 |
| Fuzzy-shrink | 33.99 | 31.81 | 30.31 | - | 33.67 | 31.75 | 30.24 | - | - | - | - | - |
| WP-shrink | 34.15 | 32.00 | 30.50 | - | 33.52 | 31.70 | 30.38 | - | - | - | - | - |
| NSSTM | 33.56 | - | 30.02 | - | - | - | - | - | 35.87 | - | 32.93 | - |
| EPLL | 33.59 | 31.33 | 29.75 | - | 33.63 | 31.89 | 30.63 | - | 35.56 | 33.85 | 32.60 | - |
| MMSE-MAP | 32.50 | - | 28.55 | - | 32.43 | - | 28.94 | - | 34.29 | - | 31.09 | - |
| NSCCT-NLM | 34.49 | - | 30.99 | - | 33.71 | - | 30.52 | - | 35.98 | - | 32.96 | - |
| NCSR | 34.98 | 33.02 | 31.72 | - | 33.90 | 32.03 | 30.74 | - | 35.81 | 34.09 | 32.92 | - |
| PLOW | - | 32.17 | - | 30.20 | - | 31.53 | - | 29.59 | - | 33.90 | - | 31.92 |
| TDNL | - | - | - | - | - | - | - | - | 35.87 | 34.13 | 32.86 | 31.86 |
| CASD | 34.38 | 32.22 | 30.64 | 29.33 | 33.69 | 31.46 | 30.90 | 29.69 | 34.66 | 32.46 | 30.94 | 29.81 |
| R-NL | - | - | 29.76 | - | - | - | 29.92 | - | - | - | 32.04 | - |

| | | | | | | | | | | | | |
|---|---|---|---|---|---|---|---|---|---|---|---|---|
| PID | 34.55 | - | 30.56 | - | 33.77 | - | 29.80 | - | 35.81 | - | 32.12 | - |
| DDID | 34.67 | - | 30.80 | - | 33.74 | - | 29.79 | - | 35.81 | - | 32.14 | - |
| NBL | 34.82 | - | 30.24 | - | 33.91 | - | 29.67 | - | 35.78 | - | 31.80 | - |
| LSSC | 34.97 | 33.00 | 31.57 | 30.47 | 34.02 | 32.20 | 30.89 | 29.87 | 35.83 | 34.15 | 32.90 | 31.87 |
| NHDW | 35.01 | - | 31.79 | 30.70 | - | - | - | - | 35.89 | - | 32.99 | 32.02 |
| BM3D | 34.98 | 33.11 | 31.78 | 30.72 | 33.92 | 32.14 | 30.88 | 29.91 | 35.93 | 34.27 | 33.05 | 32.08 |
| SAIST | 35.23 | 33.32 | 32.10 | - | 33.91 | 32.09 | 30.81 | - | 35.90 | 34.21 | 33.08 | - |
| CT-Bi-SαS-MMAE | 34.89 | 33.02 | 31.65 | 30.57 | 34.05 | 32.19 | 30.95 | 29.94 | 36.01 | 34.34 | 33.06 | 32.01 |

Table 3.7 gives the PSNR values obtained using these methods and the proposed method for three of the test images, namely, *Barbara*, *Boat* and *Lena*. It is seen from this table that the proposed CT-Bi-$S\alpha S$ -MMAE method provides PSNR values that are generally higher than that provided by the other methods.

To subjectively evaluate the performance of the proposed denoising method, the zoomed-in versions of the three test images as well as the denoised versions obtained using the proposed CT-Bi-$S\alpha S$ -MMAE method and the BM3D method when $\sigma_\eta = 30$, are shown in Figures 3.5, 3.6 and 3.7. Although the denoised images obtained using BM3D may be visually appealing, a closer look at these figures clearly shows that the denoised images obtained using BM3D are over smoothened. This over smoothing diminishes the sharpness of the edges and results in a loss of some details; on the other hand, they are better preserved by the proposed algorithm. This is clearly noticeable, especially from the edges highlighted by the arrows and the surrounding areas.

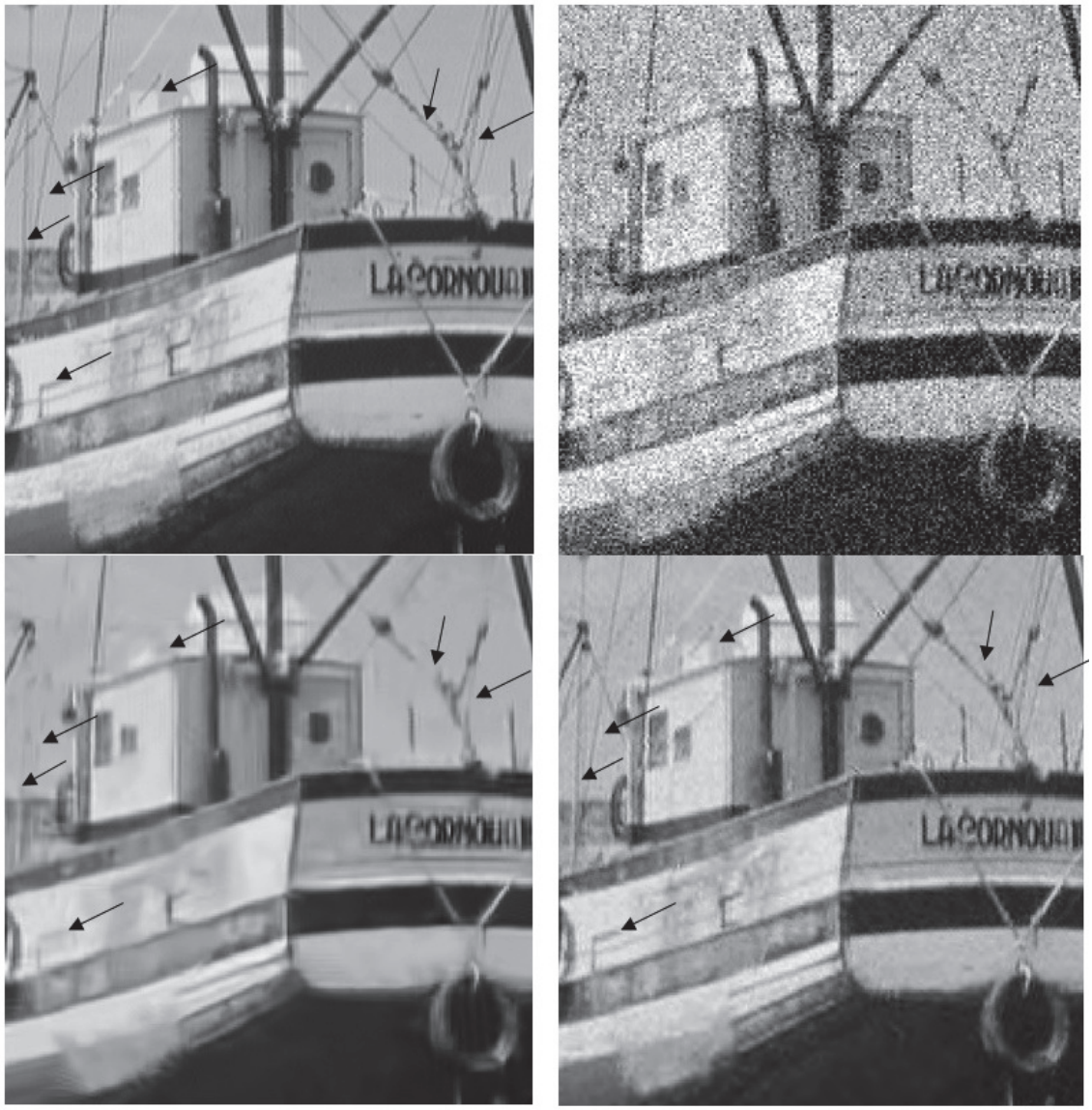

Figure 3.5. Top-left: original *Boat* image. Top-right: Noisy image with $\sigma_\eta$ =30. Bottom-left: Denoised using BM3D. Bottom-right: Denoised using the proposed method.

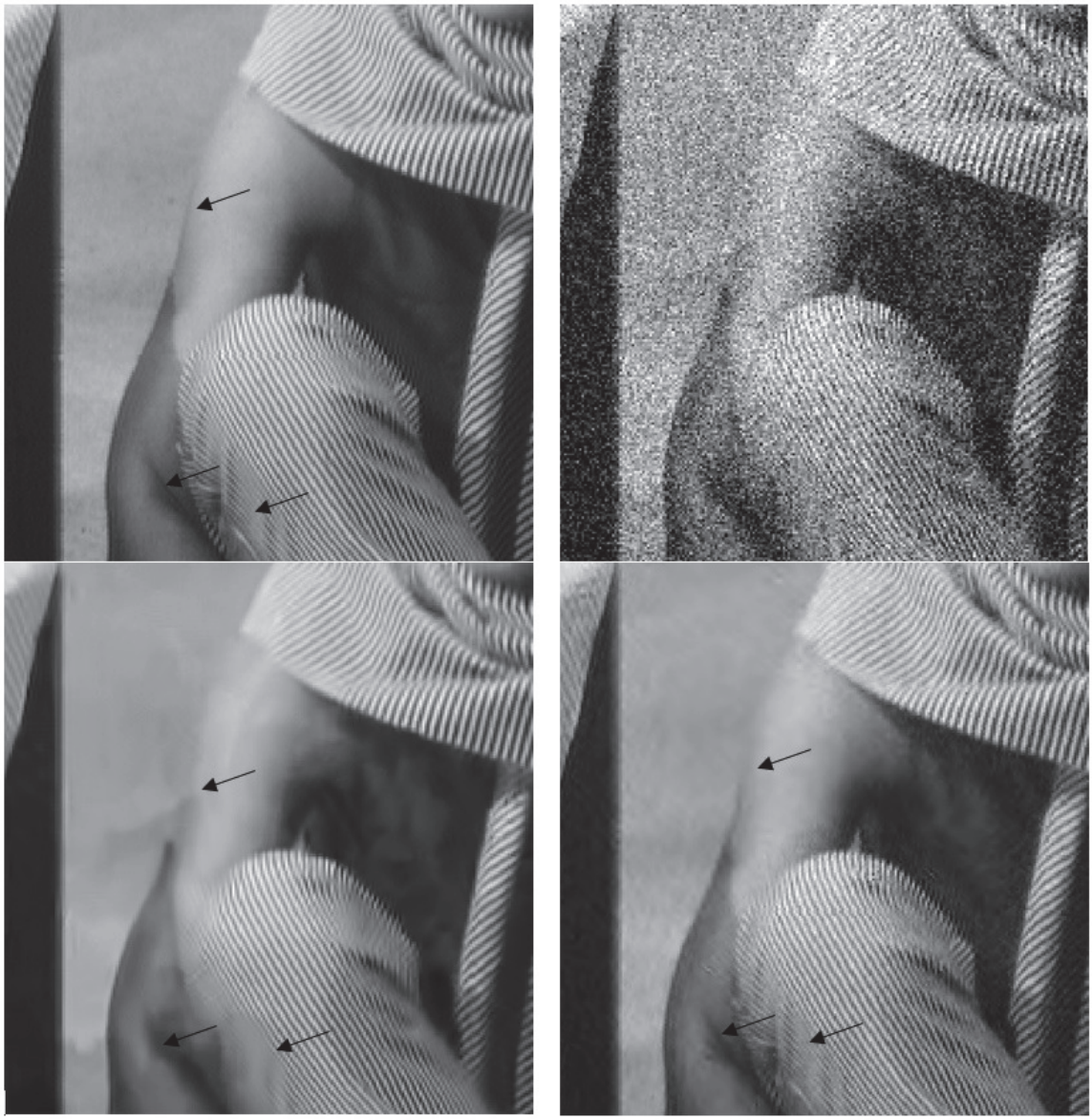

Figure 3.6. Top-left: original *Barbara* image. Top-right: Noisy image with $\sigma_\eta$=30. Bottom-left: Denoised using BM3D. Bottom-right: Denoised using the proposed method.

Figure 3.7. Top-left: original *Lena* image. Top-right: Noisy image with $\sigma_\eta$ =30. Bottom-left: Denoised using BM3D. Bottom-right: Denoised using the proposed method.

To further compare the performance of the proposed CT-Bi-$S\alpha S$-MMAE denoising method to that of the other methods, Table 3.8 gives the average PSNR values over 1000 images obtained using the proposed denoising scheme and that of some of the existing image denoising methods. It is seen from this table that the proposed denoising method provides a better performance in terms of higher PSNR values. It is also observed that the proposed CT-Bi-$S\alpha S$-MMAE denoising method outperforms BM3D, K-SVD, BLS-GSM, Trivariate and LAWMAP methods in 77%, 93%, 96.8%, 98.3% and 100% of images, respectively. Moreover, to statistically compare the performance of the proposed denoising scheme and that of BM3D, as the closest competitor, we compute the t-value of confidence between the two algorithms. The t-value between BM3D and the proposed denoising method is 1.962 that falls in 0.05 column of the t-Table of significance (95%). In view of this, the difference is considered to be significant.

Table 3.8: Averaged PSNR values obtained using various denoising methods over 1000 images.

| | Standard Deviation | | | |
|---|---|---|---|---|
| | 10 | 15 | 20 | 25 |
| LAWMAP | 33.09 | 31.37 | 29.83 | 28.37 |
| BLS-GSM | 34.53 | 32.78 | 30.97 | 29.76 |
| Trivariate | 34.11 | 32.55 | 30.71 | 29.45 |
| K-SVD | 34.82 | 33.02 | 31.36 | 30.03 |
| BM3D | 35.41 | 33.40 | 32.01 | **30.99** |
| CT-Bi-$S\alpha S$-MMAE | **35.63** | **33.51** | **32.05** | 30.90 |

Table 3.9 gives MSSIM [116] values obtained using the proposed denoising method and some of the other existing methods for three of the test images, *Barbara*, *Boat* and *Lena*. It is seen from this table that the values of the MSSIM index obtained from our proposed method is generally higher than that of the other methods, except for BM3D in which case our results are comparable, indicating the effectiveness of the proposed method in preserving edges and providing better visual quality. It should be noted that for denoising an image of size 256×256, the approximate execution time is 18 seconds, indicating the computational efficiency of the proposed algorithm.

Table 3.9: MSSIM values obtained using proposed denoising method and some of the other existing methods for three of the test images, *Barbara*, *Boat* and *Lena*.

| $\sigma_\eta$ | [16] | [19] | [107] | [86] | [105] | [18] | [82] | Proposed |
|---|---|---|---|---|---|---|---|---|
| Barbara | | | | | | | | |
| 10 | 0.92 | 0.93 | 0.93 | 0.94 | 0.94 | 0.95 | 1.00 | 0.96 |
| 20 | 0.85 | 0.87 | 0.87 | 0.88 | 0.89 | 0.91 | 0.98 | 0.94 |
| 30 | 0.78 | 0.79 | 0.81 | 0.83 | 0.82 | 0.84 | 0.95 | 0.91 |
| Boat | | | | | | | | |
| 10 | 0.93 | 0.94 | 0.94 | 0.95 | 0.96 | 0.97 | 1.00 | 0.98 |
| 20 | 0.89 | 0.90 | 0.91 | 0.92 | 0.92 | 0.93 | 0.97 | 0.96 |
| 30 | 0.86 | 0.85 | 0.87 | 0.87 | 0.89 | 0.90 | 0.95 | 0.93 |
| Lena | | | | | | | | |
| 10 | 0.93 | 0.94 | 0.94 | 0.96 | 0.97 | 0.98 | 1.00 | 0.98 |
| 20 | 0.87 | 0.89 | 0.90 | 0.89 | 0.91 | 0.91 | 0.97 | 0.95 |
| 30 | 0.81 | 0.84 | 0.83 | 0.85 | 0.86 | 0.87 | 0.94 | 0.92 |

To evaluate the performance of the proposed denoising scheme in presence of non-Gaussian noises such as Maxwell and Rayleigh, we compute the root mean squared error (RMSE) between the original and denoised images. Table 3.10 gives the averaged RMSE between the original and denoised images obtained for the proposed MAP and MMAE estimators using the alpha-stable family of distributions including the bivariate and univariate $S\alpha S$ distributions and its Cauchy member ($\alpha$=1) over a number of test images. It is seen from this table that the CT-Bi-$S\alpha S$-MMAE gives a lower RMSE values indicating its superiority to other estimators in removing non-Gaussian noises. Figures 3.8 and 3.9 illustrate the noisy *Lena* image and the corresponding denoised images obtained using BM3D and proposed CT-Bi-$S\alpha S$-MMAE denoising methods. It is seen from these figures that the proposed denoising method is superior to BM3D in removing non-Gaussian noises from images. The averaged RMSE over 20 test images obtained using BM3D and the proposed denoising methods are 0.0097 and 0.0086, when images are corrupted by the Rayleigh noise, and 0.0123 and 0.0102, when images are corrupted by the Maxwell noise, respectively. The lower RMSE values obtained using the proposed denoising scheme indicates its superiority to BM3D method in presence of non-Gaussian noises.

Table 3.10: Averaged RMSE values obtained for the MAP and MMAE estimators using the alpha-stable family of distributions over a number of test images corrupted by the Maxwell and Rayleigh noises with σ = 5.

| | Cauchy | | $S\alpha S$ | | Bi-Cauchy | | Bi-$S\alpha S$ | |
|---|---|---|---|---|---|---|---|---|
| | MAP | MMAE | MAP | MMAE | MAP | MMAE | MAP | MMAE |
| Maxwell | 0.0217 | 0.0195 | 0.0169 | 0.0145 | 0.0164 | 0.0140 | 0.0126 | **0.0102** |
| Rayleigh | 0.0189 | 0.0161 | 0.0147 | 0.0118 | 0.0133 | 0.0112 | 0.0105 | **0.0086** |

| Noisy (Maxwell) σ=5 | BM3D, RMSE=0.0945 | Proposed, RMSE=0.0883 |
|---|---|---|
| (a) | (b) | (c) |

Figure 3.8: (a) Noisy *Lena* image by the Maxwell noise with σ = 5, (b) Denoised image obtained using BM3D method, RMSE=0:0945, and (c) Denoised image obtained using the proposed method, RMSE = 0.0883.

| Noisy (Rayleigh) σ=5 | BM3D, RMSE=0.0051 | Proposed, RMSE=0.0023 |
|---|---|---|
| (a) | (b) | (c) |

Figure 3.9: (a) Noisy *Lena* image by the Rayleigh noise with σ = 5, (b) Denoised image obtained using BM3D method, RMSE = 0.0051, and (c) Denoised image obtained using the proposed method, RMSE = 0.0023.

### 3.3.1. Extension to Color Image Denoising

To denoise color images, we consider standard RGB images corrupted by additive Gaussian noise in each channel. The most common approach to denoise color images is to employ the grayscale denoising method for each of the channels. However, in order to take into consideration the dependencies of the RGB channels in color images, as shown in Figure 3.10, we use the trivariate alpha-stable model, i.e., CT-Tri-$S\alpha S$-MMAE, and its Cauchy member in the contourlet domain. An efficient closed-form shrinkage function corresponding for the MAP estimator using the multivariate Cauchy distribution is derived.

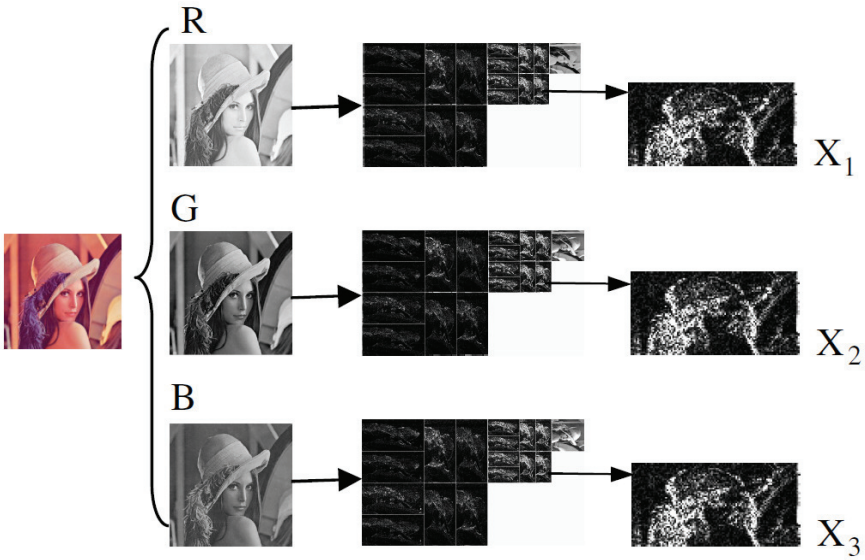


Figure 3.10. Contourlet domain decomposition of the RGB channels for color images. Each subband coefficients $X_1$ are highly dependent to the same-oriented subband coefficients of two other channels, namely, $X_2$ and $X_3$.

The PDF of the multivariate Cauchy distribution is given by

$$P_{\mathbf{x}}(\mathbf{x};\Sigma) = \frac{\Gamma(\frac{n+1}{2})}{\Gamma(\frac{1}{2})\pi^{0.5}\left|\Sigma\right|^{0.5}\left[1+\mathbf{x}^{T}\Sigma^{-1}\mathbf{x}\right]^{\frac{n+1}{2}}} \tag{3-29}$$

where $n$ is the dimensionality of the distribution, i.e., the number channels, $\Sigma$ is the covariance matrix that for the case of $n=3$ is given by

$$\Sigma = \begin{bmatrix} \sigma_1^2 & \rho_{12}\sigma_1\sigma_2 & \rho_{13}\sigma_1\sigma_3 \\ \rho_{12}\sigma_1\sigma_2 & \sigma_2^2 & \rho_{23}\sigma_2\sigma_3 \\ \rho_{13}\sigma_1\sigma_3 & \rho_{23}\sigma_2\sigma_3 & \sigma_3^2 \end{bmatrix} \tag{3-30}$$

where $\rho_{ij};\ i,j=1,2,...,n$ denotes the correlation coefficient between each of the two color channels. Let a noise-free color image $\mathbf{X}=[X_1,X_2,X_3]$ be corrupted by an additive noise $\mathbf{N}$ which is assumed to be i.i.d. Gaussian with zero mean and standard deviation $\sigma_\eta$. The corresponding noisy image $\mathbf{Y}=[Y_1,Y_2,Y_3]$ is given by $\mathbf{Y}=\mathbf{X}+\mathbf{N}$. Suppose that a noisy image is decomposed to $k=1,...,K$ scales and $d=1,...,D$ directional subbands by the contourlet transform. Then, we have $y^{i}_{k,d}(m_1,m_2)=x^{i}_{k,d}(m_1,m_2)+\eta^{i}_{k,d}(m_1,m_2)$, where $y^{i}_{k,d}(m_1,m_2)$, $x^{i}_{k,d}(m_1,m_2)$

and $\eta^{i}_{k,d}(m_1, m_2)$ denote the $(m_1, m_2)$ th coefficient at scale $k$ and direction $d$ of the contourlet transform of $\mathbf{Y}$, $\mathbf{X}$ and $\mathbf{N}$, respectively. The purpose here is to estimate the noise-free coefficients of the RGB channels. The Bayesian MAP estimator of $\mathbf{x}$, given noisy observation $\mathbf{y}$, is given by

$$\begin{aligned}\hat{\mathbf{x}} &= \arg\max_{\mathbf{x}} P_{\mathbf{x}|\mathbf{y}}(\mathbf{x} \mid \mathbf{y}) \\ &= \arg\max_{\mathbf{x}} P_{\mathbf{y}|\mathbf{x}}(\mathbf{y} \mid \mathbf{x}) P_{\mathbf{x}}(\mathbf{x}) \\ &= \arg\max_{\mathbf{x}} P_{\boldsymbol{\eta}}(\mathbf{y}-\mathbf{x}) P_{\mathbf{x}}(\mathbf{x})\end{aligned} \tag{3-31}$$

where $P_{\mathbf{x}}(\mathbf{x})$ is the PDF of the contourlet coefficients of a noise-free image and $P_{\boldsymbol{\eta}}(\boldsymbol{\eta})$ is the noise PDF which is given by

$$P_{\boldsymbol{\eta}}(\boldsymbol{\eta}) = \frac{1}{\left(\sqrt{2\pi}\sigma_{\eta}\right)^{n}} \exp\left(-\frac{\eta_1^2 + \eta_2^2 + \ldots + \eta_n^2}{2\sigma_{\eta}^2}\right) \tag{3-32}$$

The parameters $\sigma_i$ and $\rho_{ij}$ of the noise-free coefficients can be estimated by using where $S$ is a square-shaped window of size $1 \times 1$ applied to estimate the variance of each signal coefficient in a given channel $i$. After inserting (3-29) and (3-32) into (3-9), the derivative of the logarithm of the argument in (3-9) is set to zero resulting in the MAP estimate given by

$$\hat{x}_i = \text{sign}(y_i).\left(\max\left(|y_i| - 4\sigma_{\eta}^2 |B_i|\right), 0\right) \tag{3-34}$$

where B for each channel is given by

$$B_1 = \frac{\sigma_1^2 y_1 + \rho_{12}\sigma_1\sigma_2 y_2 + \rho_{13}\sigma_1\sigma_3 y_3}{[1 + \mathbf{y}^T \Sigma^{-1} \mathbf{y}]}$$
$$B_2 = \frac{\sigma_2^2 y_2 + \rho_{12}\sigma_1\sigma_2 y_1 + \rho_{23}\sigma_2\sigma_3 y_3}{[1 + \mathbf{y}^T \Sigma^{-1} \mathbf{y}]} \quad (3\text{-}35)$$
$$B_3 = \frac{\sigma_3^2 y_3 + \rho_{13}\sigma_1\sigma_3 y_1 + \rho_{23}\sigma_2\sigma_3 y_2}{[1 + \mathbf{y}^T \Sigma^{-1} \mathbf{y}]}$$

A comparison with some of the state-of-the-art methods [17], [117]-[119], is given in Table 3.11 for three of the test images, namely, *Lena*, *Peppers* and *Baboon*. It is seen from this table that the proposed color image denoising method is better than the other methods in terms of the PSNR values, except for CBM3D method for which our results are comparable. Figures 3.11, 3.12 and 3.13 illustrate the cropped noisy *Lena, Girl* and *Peppers* images and their corresponding denoised images obtained using the proposed CT-Tri-$S\alpha S$-MMAE and CBM3D methods. It can be seen from these figures that the proposed denoising method is capable of significantly suppressing the noise and preserving the details and providing a better visual quality for denoised images than that provided by CBM3D. To further investigate the performance of the proposed color image denoising, we use another group of test images, namely, the *Kodak* dataset which consists of 24 color images of size 512×768. Table 3.12 gives the averaged PSNR values obtained using the proposed denoising method as well as that yielded by other methods over the *Kodak* dataset. It is seen from this table that the proposed image denoising for color images provides higher PSNR values compared to that yielded by the other methods.

Table 3.11: PSNR values obtained using various denoising methods for two of the color images, *Lena* and P*eppers*.

| $\sigma_\eta$ | 10 | 15 | 20 | 25 | 30 |
|---|---|---|---|---|---|
| Lena | | | | | |
| Noisy | 28.13 | 24.61 | 22.13 | 20.17 | 18.60 |
| BLS-GSM [17] | 34.45 | 32.90 | 31.78 | 30.89 | 30.15 |
| Surelet [118] | 34.64 | 33.02 | 31.90 | 31.04 | 30.33 |
| ProbShrink-MB [117] | 34.60 | 33.03 | 31.92 | 31.04 | - |
| CT-Tri-Cauchy-MAP | 35.05 | 33.76 | 32.91 | 32.10 | 31.15 |
| CBM3D [119] | 35.22 | 33.94 | 33.02 | 32.27 | 31.59 |
| CT-Tri-SαS-MMAE | 35.25 | 33.95 | 32.96 | 32.11 | 31.33 |
| Peppers | | | | | |
| Noisy | 28.13 | 24.61 | 22.15 | 20.17 | 18.59 |
| BLS-GSM [17] | 33.26 | 31.89 | 30.92 | 29.46 | 27.47 |
| Surelet [118] | 33.35 | 31.79 | 30.72 | 29.89 | 29.19 |
| ProbShrink-MB [117] | 33.44 | 32.05 | 31.12 | 30.35 | - |
| CT-Tri-Cauchy-MAP | 33.61 | 32.43 | 31.59 | 30.79 | 30.09 |
| CBM3D [119] | 33.78 | 32.60 | 31.83 | 31.20 | 30.60 |
| CT-Tri-SαS-MMAE | 33.86 | 32.64 | 31.68 | 30.99 | 30.32 |
| Baboon | | | | | |
| Noisy | 28.13 | 24.61 | 22.15 | 20.17 | 18.59 |
| BLS-GSM [17] | 30.13 | 27.66 | 26.08 | 24.95 | 24.07 |
| Surelet [118] | 30.49 | 28.15 | 26.64 | 25.55 | 24.71 |
| ProbShrink-MB [117] | 30.15 | 27.72 | 26.17 | 25.04 | 24.16 |
| CT-Tri-Cauchy-MAP | 30.61 | 28.26 | 26.93 | 25.80 | 25.02 |
| CBM3D [119] | 30.64 | 28.39 | 26.97 | 25.95 | 25.14 |
| CT-Tri-SαS-MMAE | 30.71 | 28.43 | 27.00 | 25.97 | 25.13 |

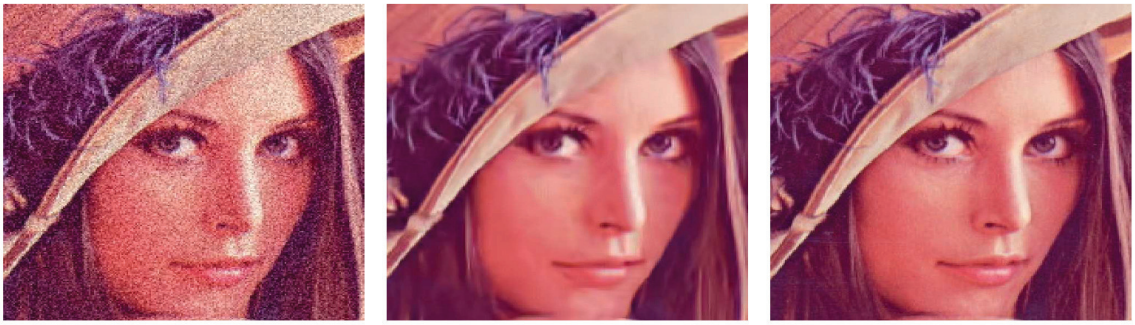

(a) (b) (c)

Figure 3.11. Color image denoising; (a) Cropped noisy *Lena* image with $\sigma$=20, PSNR=18.60 dB as well as the corresponding denoised images obtained using (b) CBM3D, PSNR=31.59 dB and (c) the proposed CT-Tri- $S\alpha S$ -MMAE, PSNR=31.33 dB.

(a) (b) (c)

Figure 3.12. Color image denoising; (a) Cropped noisy *Girl* image with $\sigma$=30, PSNR=18.61 dB as well as the corresponding denoised images obtained using (b) CBM3D, PSNR=31.78 dB and (c) the proposed CT-Tri- $S\alpha S$ -MMAE, PSNR=31.90 dB.

(a) (b) (c)

Figure 3.13. Color image denoising; (a) Cropped noisy *Peppers* image with $\sigma$=30, PSNR=18.61 dB as well as the corresponding denoised images obtained using (b) CBM3D, PSNR=31.61 dB and (c) the proposed CT-Tri- $S\alpha S$ -MMAE, PSNR=31.42 dB.

Table 3.12: Averaged PSNR (in dB) values obtained using various denoising methods on the *Kodak* dataset.

| | Standard Deviation | | | | |
|---|---|---|---|---|---|
| | 10 | 15 | 20 | 25 | 30 |
| NLM | 33.45 | 31.49 | 30.06 | 28.93 | 28.00 |
| K-SVD | 34.16 | 32.12 | 30.75 | 29.72 | 28.88 |
| BM3D | 34.90 | 32.88 | 31.55 | 30.57 | **29.81** |
| Proposed | **35.01** | **32.95** | **31.61** | **30.59** | 29.80 |

## 3.4 Summary

In this Chapter, a new image denoising method in the contourlet domain has been proposed. In this method the contourlet subband coefficients of images have been modeled by using the univariate alpha-stable distribution. The bivariate alpha-stable distribution has also been used to model the across-scale dependencies of the contourlet coefficients. Bayesian MAP and MMAE estimators have been developed by using the proposed prior in order to estimate the noise-free contourlet coefficients. To estimate the parameters of the alpha-stable distribution, a spatially-adaptive method based on fractional lower-order moments has been proposed and shown to be superior to the maximum likelihood method. Extensive experiments have been conducted to evaluate the performance of the proposed algorithm and results have been compared with that provided by the state-of-the-art methods. It has been shown that the proposed denoising method outperforms other methods in terms of the PSNR and MSSIM values as well as in terms of the visual quality of the denoised images. These results have been shown to be equally true in the case of color images, where a trivariate alpha-stable distribution has been proposed to capture cross correlations between the RGB color channels. In the next chapter, the proposed alpha-stable model will be employed in developing a technique for despeckling the synthetic aperture radar images.

# CHAPTER 4

# Despeckling of the SAR Images in the Contourlet Domain

## 4.1 Introduction

Synthetic aperture radar (SAR) images are intrinsically affected by multiplicative speckle noise. There has been a growing effort in preprocessing of the SAR images due to their importance in many applications such as high-resolution remote sensing, surface surveillance and automatic target recognition [120], [121]. A prerequisite of using SAR images is to remove the multiplicative speckle noise. In recent years, multiscale transforms have been used with considerable success for recovering signal from noisy data [121]-[126]. It has been shown that denoising of images in the contourlet domain in comparison to wavelet domain reduces the noise more significantly [127], [128]. This is due to the fact that the contourlet transform because of its flexible directional decomposability in each scale is more effective than wavelet is in representing smooth contour details in images [4].

It is known that the Bayesian estimators outperform classical linear processors and simple thresholding estimators in removing speckle noise from SAR images [122]. In view of this, the homomorphic filtering-based methods wherein a suitable PDF is used as a prior model for describing the log-transformed wavelet coefficients have been proposed for multiplicative noise reduction [123]-[126]. In [123], a spatially-adaptive despeckling method has been proposed in wavelet domain. In [124], a dual-tree complex wavelet transform based despeckling method has been used to denoise the SAR images. In [125],

a Laplacian-Gaussian modeling has been used in wavelet domain for despeckling the SAR images. The performance of the Bayesian estimator depends considerably on the suitability of the model assumed for the prior PDF of the image and noise. As discussed in Chapter 2, the contourlet subband coefficients of an image have significant non-Gaussian and heavy-tailed statistics and can be accurately modeled by the alpha-stable family of distributions [15]. In view of this, in this chapter, a new Bayesian MAP estimator using the symmetric alpha-stable distribution is developed to despeckled SAR images [129]. The proposed estimator exploits the statistics of the contourlet coefficients. Simulations are conducted using synthetically-speckled and real SAR images, and the performance of the proposed method using the MAP estimator is evaluated and compared to that of the existing techniques.

## 4.2 Bayesian MAP Estimator

Since the speckle noise model for SAR images is considered to be multiplicative, the observed output of the SAR imaginary system can be defined as

$$y_{i,j} = x_{i,j} n_{i,j} \tag{4-1}$$

where $y_{i,j}$ denotes the $(i, j)$ th noisy pixel in a SAR image corresponding to the noise-free pixel $x_{i,j}$ and $n_{i,j}$ denotes the corrupting multiplicative speckle component. For an $L$-look SAR image, the PDF of the speckle noise has a Gamma distribution given by

$$P_n(n) = \frac{L^L n^{L-1} e^{-Ln}}{\Gamma(L)} \tag{4-2}$$

where $\Gamma$ denotes the gamma function and variance of noise equals to $1/L$ [124]. It should be noted that the lower the value of $L$, the higher is the level of the noise. With log-transformation, (4-1) becomes

$$Y_{i,j} = X_{i,j} + N_{i,j} \tag{4-3}$$

where $Y = \ln(y)$, $X = \ln(x)$ and $N = \ln(n)$. The mean and variance of the logarithmically transformed gamma distribution are $\psi(0, L) - \ln(L)$ and $\psi(1, L)$, respectively [124], where $\psi(i, L)$ is the $i$th polygamma function of $L$ looks, and it is given by $\psi(i, z) = (\frac{\partial}{\partial z})^{i+1} \ln\Gamma(z)$. Suppose that a noisy image is decomposed to $j = 1,..., J$ scales and $d = 1,..., D$ direction subbands by the contourlet transform. Then, we have

$$y_j^d(m,n) = x_j^d(m,n) + \eta_j^d(m,n) \tag{4-4}$$

where $y_j^d(m,n)$, $x_j^d(m,n)$ and $\eta_j^d(m,n)$ denote the $(m,n)$th contourlet coefficient of the log-transformed noisy image at scale $j$ with direction $d$, the corresponding log-transformed noise-free coefficient and the corresponding noise component after logarithmic transformation. Despeckling is based on estimating the noise-free coefficients $x$ as a function of the noisy observations $y$. To this end, a Bayesian MAP estimator is developed through modeling the contourlet coefficients of a noisy image by the alpha-

stable PDF. The Bayesian MAP estimator of $x$, given noisy observation $y$, can be derived as

$$\begin{aligned}\hat{x}(y) &= \arg\max_x P_{x|y}(x \mid y) \\ &= \arg\max_x P_{x|y}(y \mid x) P_x(x) \\ &= \arg\max_x P_\eta(y - x) P_x(x)\end{aligned} \tag{4-5}$$

where $P_x(x)$ is the PDF of the contourlet coefficients of a noise-free image, $P_\eta(\eta)$ is the noise PDF. Although the speckle noise can be modelled by the gamma PDF, it becomes very close to the Gaussian distribution as a result of the logarithmic transformation [123]. Therefore, in the proposed denoising method, the noise is assumed to be white Gaussian with a zero mean and a standard deviation of $\sigma_\eta$. The corresponding PDF is given by

$$P_\eta(\eta) = \frac{1}{\sqrt{2\pi\sigma_\eta^2}} \exp\left(-\frac{\eta^2}{2\sigma_\eta^2}\right) \tag{4-6}$$

If $\sigma_\eta$ is unknown, it may be estimated by applying the robust median absolute deviation method [72] in the finest subband of the observed noisy coefficients. To obtain the MAP estimate, after inserting the noise PDF into (4-5), the derivative of the logarithm of the argument in (4-5) is set to zero resulting in

$$\frac{\hat{x} - y}{\sigma_\eta^2} + \frac{\partial}{\partial y}(-\ln(P_x(y))) = 0 \tag{4-7}$$

Therefore, the Bayesian MAP estimator for non-Gaussian data is derived as

$$\hat{x}(y) = sign(y)\max\left(0, |y| - \sigma_\eta^2 \left| \frac{d \ln P(y)}{dy} \right| \right) \tag{4-8}$$

Since there is no closed-form PDF for the alpha-stable distribution, we numerically compute the Bayesian MAP estimator output in (4-8). The proposed despeckling, whose block diagram is shown in Figure 4.1, can be summarized as follows:

1) Perform the log-transformation of the observed SAR image.
2) Apply the contourlet transform on the log-transformed image and obtain the contourlet coefficients.
3) Estimate the parameters of the alpha-stable distribution $\gamma$ and $\alpha$ from the noisy coefficients.
4) Estimate the noise-free coefficients using the Bayesian MAP estimator in (4-8).
5) Apply the inverse contourlet transform on the estimated noise-free coefficients.
6) Carry out the mean adjustment of the quantity obtained in Step 5 by subtracting it from the mean of log-transformed noise, i.e., $\psi(L) - \ln(L)$.
7) Perform the exponential transformation of the values obtained in Step 6 to obtain the despeckled image.

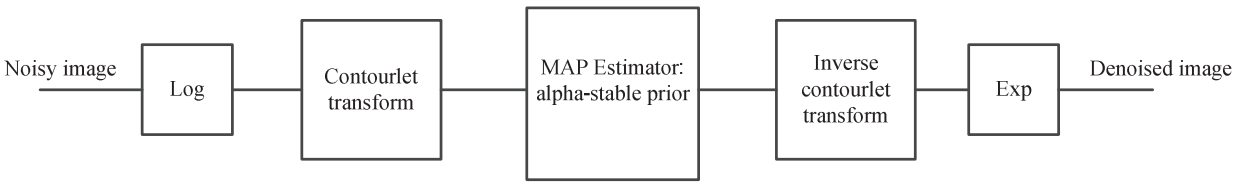


Figure 4.1. Block diagram of the proposed algorithm for speckle reduction.

## 4.3 Experimental Results

The performance of the proposed despeckling method is evaluated by conducting experiments on synthetically-speckled or real SAR images. The obtained results are compared to those obtained by some of the existing speckle filtering methods in the wavelet and contourlet domain, namely, WIN-SAR [122], UWT [126], LAM [128], and NSCT [130]. It should be noted that the contourlet transform is a shift-variant transform. In order to overcome the possible pseudo-Gibbs phenomenon in the neighborhood of discontinuities, in the proposed despeckling method, the cycle spinning method is performed on the observed noisy image. The noisy image is then decomposed, using the contourlet transform, into four scales with eight directions in each scale. In order to quantify the performance improvement, the PSNR is computed between the synthetically-speckled and denoised images. Table 4.1 shows the PSNR values in decibels for the two synthetically-speckled images, namely *Boat* and *Lena*. It can be seen from this table that the proposed contourlet-based despeckling method provides PSNR values that are higher than those provided by the other methods for a given range of noise level. In case of the *Lena* image, the proposed despeckling method exhibits a clearly better performance than that of other methods do. Figure 4.2 shows a real SAR image, *Ajkwa* image, obtained from [131] and its despeckled versions obtained by using the NSCT, UWT and LAM methods. The equivalent number of looks (ENL) value is given by [123] $ENL = \frac{\mu_x^2}{\sigma_x^2}$, which is used to evaluate the performance of these methods for speckle noise reduction in which $\mu$ and $\sigma$ are the mean and standard deviation within the selected homogenous region $x$. For the ENL calculation, two uniform regions in the

*Ajkwa* image are considered, shown in Figure 4.2(a). Table 4.1 gives the ENL values obtained for two regions using various despeckling methods. From this table, it can be seen that the proposed method outperforms the other methods in reducing speckle noise in uniform regions and provides better visual quality by preserving the edges than those given by the other methods.

TABLE 4.1: PSNR values obtained using different despeckling methods for synthetically-speckled *Boat* and *Lena* images.

| | Number of looks (L) | | | |
|---|---|---|---|---|
| | 3 | 4 | 5 | 6 |
| | Boat | | | |
| Proposed | **23.05** | **23.89** | **24.32** | **24.56** |
| WIN-SAR [122] | 22.14 | 23.13 | 23.92 | 24.42 |
| NSCTS [130] | 22.93 | 23.79 | 24.35 | 24.68 |
| UWT [126] | 21.83 | 22.49 | 23.07 | 23.88 |
| LAM [128] | 21.55 | 22.89 | 23.69 | 24.15 |
| | Lena | | | |
| Proposed | **28.95** | **30.08** | **30.72** | **31.46** |
| WIN-SAR [122] | 25.09 | 26.93 | 29.05 | 30.62 |
| NSCTS [130] | 28.65 | 29.70 | 30.75 | 31.46 |
| UWT [126] | 28.12 | 29.36 | 30.29 | 31.08 |
| LAM [128] | 25.78 | 26.73 | 27.29 | 27.90 |

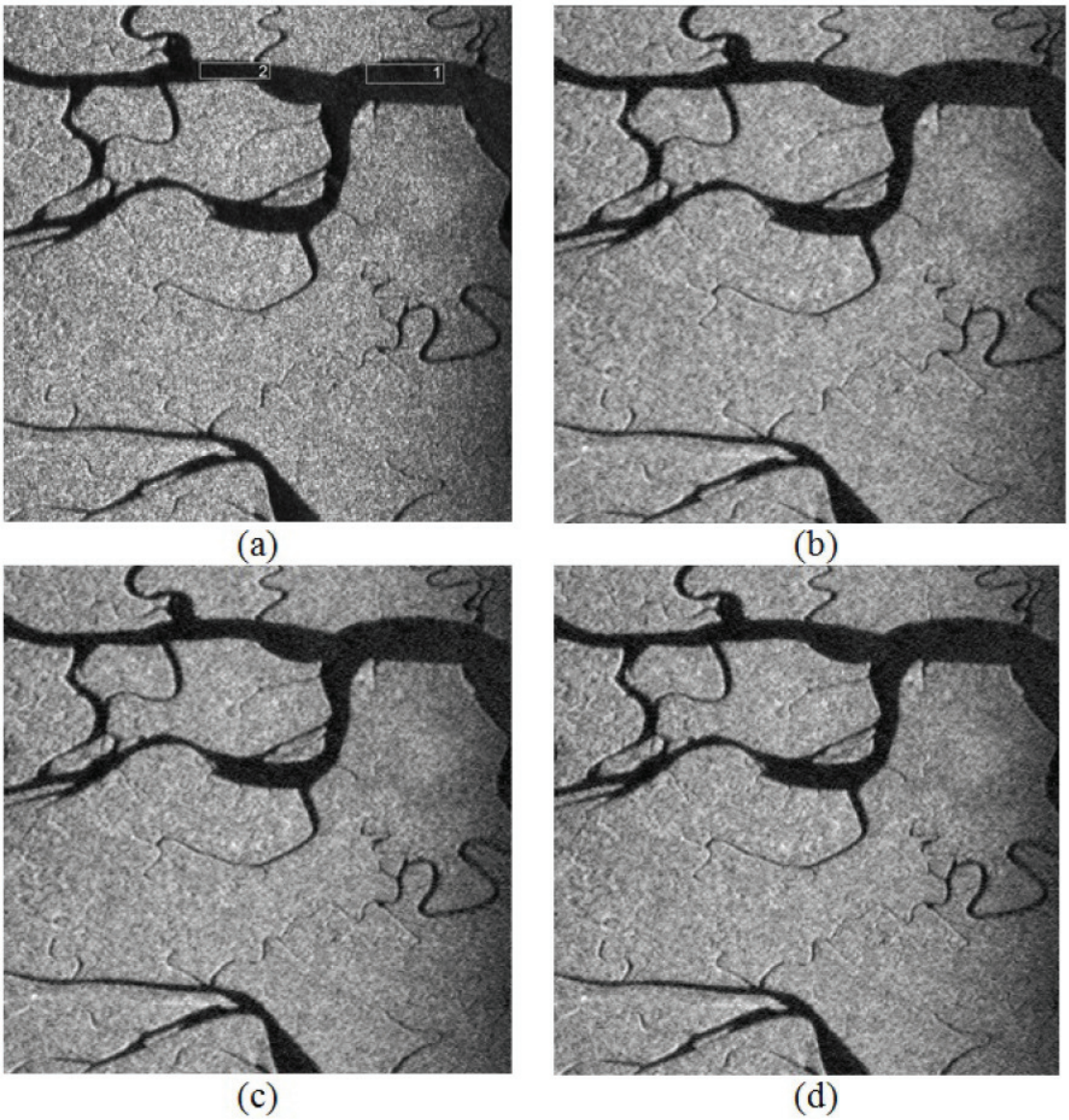


Figure 4.2. (a) *Ajkwa* image. Obtained despeckled images by using various methods, namely, (b) WIN-SAR, (c) NCST, and (d) the proposed method.

## 4.4 Summary

In this chapter, a new scheme for despeckling of SAR images in the contourlet domain has been proposed. The SAR images are logarithmically transformed to convert the multiplicative speckle noise into an additive noise. It is then decomposed into various scales and directional subbands via the contourlet transform. The proposed method has been developed by modeling the contourlet coefficients of the log-transformed SAR image using the symmetric alpha-stable distribution. The noise in all the detail subbands is removed by the Bayesian MAP estimator using the alpha-stable prior. Experiments have been carried out using the synthetically-speckled and real images to examine the performance of the proposed method and compare it with that of some of the existing methods. The results have shown that the proposed despeckling method outperforms other methods in term of the PSNR values and provides better visual quality despeckled images. The proposed method has also been shown to provide a better speckle reduction in the homogeneous regions of images.

# CHAPTER 5

# Multiplicative Watermark Detection in the Contourlet Domain Using Alpha-Stable Distributions

## 5.1 Introduction

Based on the study carried out in Chapter 2 on effectiveness of the alpha-stable family of distributions in modeling the contourlet coefficients of images, in this chapter, a new image watermarking scheme in the contourlet domain is proposed [132]. A new blind watermark detector is also designed based on the proposed alpha-stable family of distributions.

Digital data distribution on the internet has made researchers to pay special attention to copyright issues. Digital watermarking has been widely applied to different media contents such as videos, audios and images for the purpose of identifying the ownership of the media. Various watermarking schemes have been proposed to protect the copyright information. These schemes may be categorized in many ways such as the domain in which the watermark is embedded for example pixel [133], frequency [134], and the method of embedding, additive [135], [136] multiplicative [137], [138] or based on quantization [139]. In many applications, the detection of a specific watermark is sufficient, without it being extracted. The commonly-used additive and multiplicative embedding rules are given by

Additive watermarking:

$$Y = X + \xi W \tag{5-1}$$

Multiplicative watermarking:

$$Y = X + X\,\xi\,W \tag{5-2}$$

where $X$ and $Y$ are, respectively, the original and watermarked data, $W$ is a watermark sequence and $\xi$ a weighting factor. It should be mentioned that by increasing the amount of embedded information, i.e., by increasing $\xi$, the robustness of the watermarking scheme is increased. The multiplicative watermarks have been widely used for copyright protection, in view of its robustness. Hence, detection of multiplicative watermarks has received a great deal of attention. Due to their simplicity, correlation-based detectors have been used for detecting the watermarks, especially for additive watermarking schemes [135]. However, it has been shown that these detectors are not optimal for the detection of multiplicative watermarks [138].

A watermarking scheme should be robust against any intentional or unintentional distortion and the authorized user should be able to detect the watermark. The robustness can be significantly increased by utilizing the spread spectrum technique in which the watermark is embedded in a transformed domain such as DCT [24], [25], DWT [26]-[28], ridgelet transform [140], curvelet transform [141] and the contourlet transform [33], [34]. Recently, a number of watermarking schemes have been proposed, wherein the watermark is embedded into the contourlet coefficients of the image [13], [142]. It has been shown that the contourlet-domain watermark techniques are more robust than other frequency-domain watermarking algorithms against any kind of attack [13], [33], [34]. The most commonly used detector for the frequency domain watermarking schemes is the correlation detector, which is optimal only if the data samples follow the Gaussian distribution function [143]. In the case when these data samples are not Gaussian, optimal

or sub-optimal detectors have been developed by modeling the frequency-domain coefficients using various PDFs, such as the Laplacian [28], student-t [36], and generalized Gaussian [13]. In view of the fact that the contourlet coefficients of an image are highly non-Gaussian [12], [15], a proper distribution to model the statistics of the contourlet coefficients is a heavy-tailed PDF. It has been shown in [13] that the generalized Gaussian distribution can model the contourlet coefficients. Accordingly, a statistical watermark detector has been proposed in [13] for the contourlet-domain image watermarking by modeling the contourlet coefficients with the GG distribution.

In this chapter, multiplicative watermark detectors are designed in the contourlet domain by using the univariate and bivariate alpha-stable distributions. The watermark detectors using the univariate and bivariate Cauchy members of the alpha-stable family are also designed. The performance of the proposed detectors are evaluated experimentally and theoretically by obtaining the receiver operating characteristics. The robustness of the proposed watermarking scheme is examined when the watermarked images are attacked by various kinds of attacks. Finally, we compare the performance of the proposed detectors with that of the GG detector.

## 5.2 Watermarking

In watermarking applications, there have been several works suggesting that the performance of the contourlet-domain algorithms is better than those based on the wavelets [12], [36]. This is mostly due to the spreading property of the contourlet transform in that if the watermark bits are inserted into specific subbands (e.g., lowpass or highpass), they will be spread out into all the subbands when the watermarked image is reconstructed [36]. Thus, it makes the contourlet-domain watermarking algorithms more

resistant to attacks. The spreading effect and robustness are affected by many factors such as the embedded watermark, the content of the original image and the filter characteristics of the contourlet transform.

### 5.2.1 Watermark Embedding

In the embedding process, we focus specifically on a multiplicative spread spectrum scheme in the contourlet domain. The contourlet transform is first applied to an image to capture the important features of the image in a few coefficients. It has been shown that a watermark should be inserted into the significant features of an image in order to increase the robustness of the watermark [133]. In view of this, we are going to find the coefficients that represent most of the features of an image; hence, we compute the variance of the coefficients in each directional subband and then select the subband $X$ that has the highest value for its variance for embedding the watermark. For an $M_1 \times M_2$ image, this subband $X$ is given by

$$\left\{ X = \arg\max_{j,d} \left[ \sum_{k=1}^{N_j} \left[ C_{j,d}^{k} \right]^2 \right], \quad N_j = \frac{M_1 M_2}{2^{2(j-1)} D_j} \right\} \tag{5-3}$$

where $j = 1,..., J$ refers to the number of resolution levels and $d = 1,..., D_j$ to the number of frequency directions. Figure 5.1 shows a block diagram of the proposed watermark embedding procedure. The watermark sequence $W$ modifies the contourlet coefficients of the selected subband $X$ giving the watermarked coefficients $Y$. The watermark may or may not contain a message. When the watermark carries a message, the message is coded into a binary sequence $\{b_i\}_{i=1}^{N}$ with +1 for bit 1 and -1 for bit 0 for

the message. The watermark is generated using a direct sequence spread spectrum technique, wherein the watermark is generated using a pseudorandom sequence generator that has an authentication key as its initial value. This pseudorandom sequence spreads the spectrum of the watermark signal over many coefficients making it difficult to be detected. To maximize the security and robustness of the watermarking scheme, the sequence should have white-noise like properties [27]. Let such a sequence be denoted by $\{s_i\}_{i=1}^{N}$, where $s_i$ takes the values 1 or -1 with equal probability. In order to assure a robust watermarking scheme, the watermark should have maximum strength without affecting the perceptual quality of the image. For this purpose, a positive watermark weighting factor $\xi$ is used to provide a trade-off between the robustness of the watermarking method and the imperceptibility of the embedded watermark based on the local characteristics of the image for a given resolution level and frequency direction. The contourlet coefficients of the selected subband are modified as $y_i = x_i + \xi x_i w_i$, where $\{x_i\}_{i=1}^{N}$ and $\{y_i\}_{i=1}^{N}$ are the original and watermarked coefficients, respectively, and $W = \{w_i = b_i s_i\}_{i=1}^{N}$.

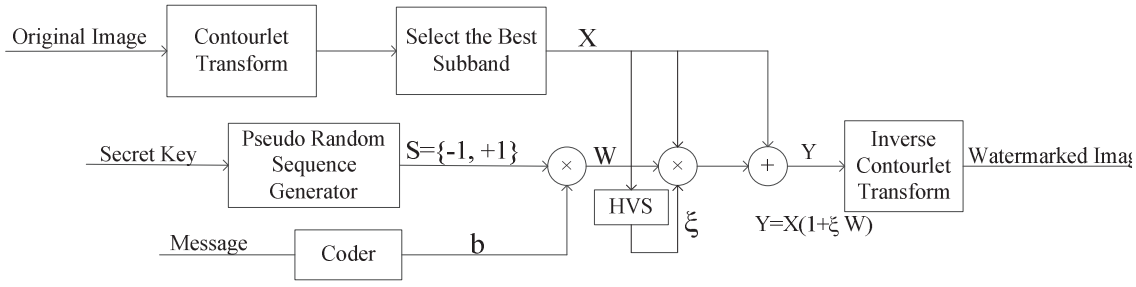


Figure 5.1. Block diagram of the watermark embedding procedure.

The weighting factor $\xi$ is calculated for an image by using the watermark to document ratio (WDR) given by [27]

$$WDR = 10\log\left(\frac{\xi^2}{\sigma_{x_i}^2}\right) \tag{5-4}$$

where the term "document" refers to the contourlet coefficients of the original image and $\sigma_{x_i}^2 = \frac{1}{N}\sum_i x_i^2$ . In this case, the watermark can be adapted to the local properties of the original image. It should be mentioned that $\xi$ can be increased to a point where the watermark is still invisible, and yet it is still detectable. The watermarked contourlet coefficients are then inverse transformed to get the watermarked image.

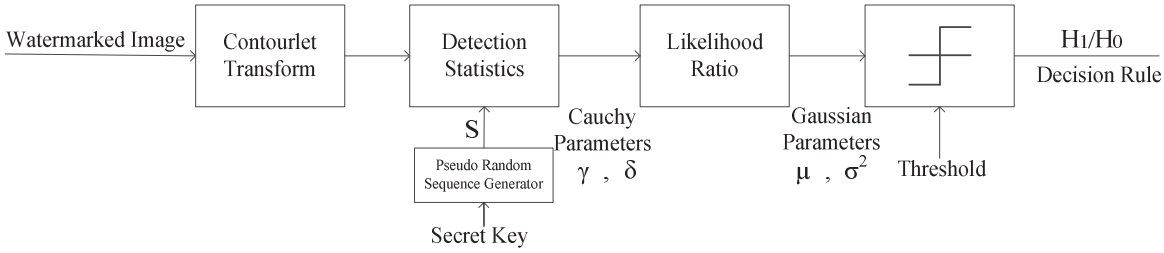


Figure 5.2. Block diagram of the watermark detection procedure.

### 5.2.2 Watermark Detection

In general, a watermarking scheme for copyright protection has an embedded watermark that is known to the intended receiver. Hence, the verification of its existence, i.e., the detection of the watermark, is sufficient for the purpose of checking the authenticity of the copyright. Figure 5.2 gives a block diagram of the different steps involved in the

watermark verification process. Current detection methods use the signal statistics for the watermark detection. We propose a method based on Bayesian log-likelihood ratio test for detecting the watermark in the contourlet coefficients of a watermarked image. This method can be reduced to a binary hypothesis test to verify the presence of a watermark. It consists of testing a hypothesis $H_1$ against a null hypothesis $H_0$ and can be mathematically formulated based on the statistical properties of the contourlet coefficients [144]. The hypotheses $H_1$ and $H_0$ represent as to whether the contourlet coefficients are watermarked by the sequence $W$ or do not carry any watermark, respectively, and can be stated as

$$\begin{aligned} H_1 &: Y = X + \xi XW \\ H_0 &: Y = X \end{aligned} \tag{5-5}$$

In detection, the goal is to see whether or not there is a watermark in the received image $Y$, based on the statistical properties of the original image $X$. The data is modeled by an appropriate statistical distribution. The decision rule is then defined as the likelihood ratio $\Lambda_{\text{det}}(Y)$

$$\Lambda_{\text{det}}(Y) = \frac{f_y(Y \mid H_1)}{f_y(Y \mid H_0)} \tag{5-6}$$

which is then compared to a threshold $\tau$:

$$\Lambda_{\text{det}}(Y) \underset{H_0}{\overset{H_1}{\gtrless}} \tau \tag{5-7}$$

The likelihood ratio uses the probability density functions as

$$f_y(Y \mid H_1) = \frac{1}{1+\xi W} f_x\left(\frac{Y}{1+\xi W}\right)$$
$$f_y(Y \mid H_0) = f_x(Y) \tag{5-8}$$

The likelihood ratio becomes

$$\Lambda_{\text{det}}(Y) = \prod_{i=1}^{N} \frac{p\left(\frac{y_i}{1+\xi w_i}\right)}{p(y_i)} \cdot \frac{1}{1+\xi w_i} \tag{5-9}$$

In practice, the log-likelihood ratio is usually preferred in hypothesis testing [144], and is defined as the natural logarithm of $\Lambda_{\text{det}}(Y)$; hence, the decision rule becomes:

$$\ln \Lambda_{\text{det}} \underset{H_0}{\overset{H_1}{\gtrless}} \ln(\tau) \tag{5-10}$$

and the log-likelihood ratio is

$$\ln(\Lambda_{\text{det}}) = \sum_{i=1}^{N} \ln\left( \frac{p\left(\frac{y_i}{1+\xi w_i}\right)}{p(y_i)} \cdot \frac{1}{1+\xi w_i} \right) \tag{5-11}$$

The detector is supposed to choose between $H_1$ and $H_0$ based on the received image $Y$. In this case, if $\ln(\Lambda_{\text{det}}) > \ln(\tau)$, $H_1$ is accepted; otherwise, $H_0$ is accepted. The log-

likelihood ratio is clearly a superposition of $N$ statistically independent random variables with finite mean and variance. Thus, according to the central limit theorem for large $N$ [143], the log-likelihood ratio follows an approximately Gaussian distribution under each hypothesis. The mean and variance of each of the Gaussian distributions can be estimated from the empirical data and are given by $(\mu_0, \sigma_0^2)$ and $(\mu_1, \sigma_1^2)$, for $H_0$ and $H_1$, respectively. It is known that in the decision task there may be two types of errors [37], [144]. Type I error occurs when detector decides $H_1$ when in fact $H_0$ is correct. This error is called the probability of false-alarm denoted by $P_{fa}$. Type II error occurs when $H_0$ is accepted while $H_1$ is correct. This error is called miss-detection denoted by $P_m = 1 - P_{\text{det}}$, where $P_{\text{det}}$ is the detection probability of accepting $H_1$ when the watermark is present. In order to design our watermark detector based on the alpha-stable distribution, we obtain the log-likelihood ratio in (5-11) using the alpha-stable PDF. It is to be noted that there is no closed-form expression for the $S\alpha S$ distribution except when $\alpha$ takes the values 0.5 for the Levy, 1 for the Cauchy and 2 for the Gaussian distributions. Therefore, we use the Monte Carlo simulations to numerically find the log-likelihood ratio $\ln(\Lambda_{\text{det}})$. To this end, 1000 randomly generated watermark sequences that have uniquely-defined keys are employed. For each run, we first estimate the log-likelihood ratio $\ln(\Lambda_{\text{det}})$ of an image using (5-11) for both the hypotheses. The experimental mean and variance of $\ln(\Lambda_{\text{det}})$ for each of the detectors are then estimated. Thus, when the mean and variance of the log-likelihood ratio under both hypotheses are known, for a particular value of $\tau$, the probabilities of false alarm and detection can be estimated as [144]

$$P_{fa} = Q\left(\frac{\tau - \mu_0}{\sigma_0}\right) \quad , \quad P_{\text{det}} = Q\left(\frac{\tau - \mu_1}{\sigma_1}\right) \tag{5-12}$$

where $Q(x)$ is defined as $Q(x) = \frac{1}{\sqrt{2\pi}} \int_x^{\infty} e^{-z^2/2} dz$. The decision threshold is obtained by using the Neyman-Pearson criterion that minimizes the probability of miss-detection, i.e., $1 - P_{\text{det}}$, for a given probability of false alarm $P_{fa}$ [37], [144] and can be expressed as

$$\tau = \sigma_0 \, Q^{-1}\left(P_{fa}\right) + \mu_0 \tag{5-13}$$

and $P_{\text{det}}$ as

$$P_{\text{det}} = Q\left(\frac{\sigma_0}{\sigma_1} Q^{-1}\left(P_{fa}\right) - \frac{\mu_1 - \mu_0}{\sigma_1}\right) \tag{5-14}$$

The performance of the proposed statistical detector can be analyzed theoretically by relating the probability of detection and the probability of false alarm. Resulting curves are called the receiver operating characteristics (ROC). It should be noted that the probability of detection needs to be kept at a high level for a predefined rate of false alarm to increase the reliability of detection.

### 5.2.3 Detector Based on the Univariate Alpha-Stable Distribution

The theoretical ROC curves can be derived by obtaining the mean and variance of the log-likelihood ratio under each hypothesis. Using the Cauchy member of the alpha-stable family, the log-likelihood ration in (5-11) can be rewritten as

$$\ln(\Lambda_{\text{det}}) = \sum_{i=1}^{N} \ln\left( \frac{\gamma^2 + (y_i)^2}{\gamma^2 + \left( \frac{y_i}{1+\xi w_i} \right)^2} \right) + \sum_{i=1}^{N} \ln\left| \frac{1}{1+\xi w_i} \right| \tag{5-15}$$

Having (5-15), the theoretical mean and variance of $\ln(\Lambda_{\text{det}})$ under $H_0$ can be obtained as follows:

Let $\ln(\Lambda_{\text{det}}) = q_1(Y) + q_2(Y)$, where

$$\begin{aligned} q_1(Y) &= -\ln(1+\xi W) \\ q_2(Y) &= \ln\left( \frac{\gamma^2 + Y^2}{\gamma^2 + \left( \frac{Y}{1+\xi W} \right)^2} \right) \end{aligned} \tag{5-16}$$

It is known in that for large $N$, the log-likelihood ratio under both the hypotheses can be approximated by Gaussian distributions with means $(\mu_0, \mu_1)$ and variances $(\sigma_0^2, \sigma_1^2)$ [143]. The mean and variance of the log-likelihood ratio under $H_0$ can be obtained as

$$\mu_0 = \mu(\ln(\Lambda_{\text{det}}); H_0) = \sum_{i=1}^{N} \left( \mu_{q_1}(y_i) + \mu_{q_2}(y_i) \right) \tag{5-17}$$

and

$$\sigma_0^2 = \sigma^2\left(\ln(\Lambda_{\text{det}}); H_0\right)$$
$$= \sum_{i=1}^{N}\left(\sigma_{q_1}^2(y_i) + \sigma_{q_2}^2(y_i) - 2\mu_{q_1}(y_i)_{q_2}(y_i) + 2\mu_{q_1}(y_i)\mu_{q_2}(y_i)\right) \tag{5-18}$$

We assume that the watermark sequence $W$ is generated by a pseudorandom sequence taking values +1 and -1 with equal probability. Hence, $\mu_{q_1}(y_i)$ and $\mu_{q_2}(y_i)$ can be obtained as

$$\mu_{q_1}(y_i) = -\frac{1}{2}\left[\ln(1+\xi) + \ln(1-\xi)\right] \tag{5-19}$$

and

$$\mu_{q_2}(y_i) = \ln\left(\gamma^2 + Y^2\right) - \frac{1}{2}\ln\left(\gamma^2 + \left(\frac{Y}{1+\xi}\right)^2\right) - \frac{1}{2}\ln\left(\gamma^2 + \left(\frac{Y}{1-\xi}\right)^2\right) \tag{5-20}$$

and hence $\mu_0$ can be calculated as

$$\mu_0 = E\left[\ln(\Lambda_{\text{det}}) \mid H_0\right] = -\sum_{i=1}^{N}\frac{\ln(1+\xi) + \ln(1-\xi)}{2} + \sum_{i=1}^{N}\left(\ln\left[\gamma^2 + (x_i)^2\right] - \frac{1}{2}\ln\left[\gamma^2 + \left(\frac{x_i}{1+\xi}\right)^2\right] - \frac{1}{2}\ln\left[\gamma^2 + \left(\frac{x_i}{1-\xi}\right)^2\right]\right) \tag{5-21}$$

In order to find the variance of the log-likelihood ratio, given by (5-18), the various terms can be found as

$$\sigma_{q1}^2 = E\left[{q_1}^2\right] - \mu_{q1}^2 = \frac{1}{4}\left[\ln(1+\xi) + \ln(1-\xi)\right]^2 \tag{5-22}$$

$$\sigma_{q2}^2 = E\left[{q_2}^2\right] - \mu_{q2}^2 = \frac{1}{4}\left[\ln\frac{\gamma^2 + \left(\frac{Y}{1-\xi}\right)^2}{\gamma^2 + \left(\frac{Y}{1+\xi}\right)^2}\right]^2 \tag{5-23}$$

$$\mu_{q1q2} = -\frac{1}{2}\left[\ln(1+\xi)\frac{\gamma^2 + Y^2}{\gamma^2 + \left(\frac{Y}{1+\xi}\right)^2}\right] - \frac{1}{2}\left[\ln(1-\xi)\frac{\gamma^2 + Y^2}{\gamma^2 + \left(\frac{Y}{1-\xi}\right)^2}\right] \tag{5-24}$$

$$\mu_{q1}\mu_{q2} = -\frac{1}{2}\left[\ln(1+\xi) + \ln(1-\xi)\right]\left[\ln\frac{\gamma^2 + Y^2}{\left[\left(\gamma^2 + \left(\frac{Y}{1+\xi}\right)^2\right)\left(\gamma^2 + \left(\frac{Y}{1-\xi}\right)^2\right)\right]^{1/2}}\right] \tag{5-25}$$

Then, after some mathematical manipulations, the final expression for the variance, $\sigma_0^2$ is obtained as

$$\sigma_0^2 = Var[\ln(\Lambda_{\text{det}}) \mid H_0] = E[\ln(\Lambda_{\text{det}}) - E[\ln(\Lambda_{\text{det}}) \mid H_0]]^2$$
$$= \sum_{i=1}^{N} \frac{1}{4} \left\{ \left( \ln(1+\xi) - \ln(1-\xi) + \ln \frac{\gamma^2 + \left( \frac{x_i}{1-\xi} \right)^2}{\gamma^2 + \left( \frac{x_i}{1+\xi} \right)^2} \right)^2 \right\} \tag{5-26}$$

where parameter $\gamma$ of the Cauchy distribution can be directly computed from the contourlet coefficients of the watermarked image. The mean and variance of the log-likelihood ratio under $H_1$ can also be found as $\mu_0 = -\mu_1$ and $\sigma_0^2 = \sigma_1^2$. Figure 5.3 depicts the experimental ROC curves for the $S\alpha S$ distribution. This figure also shows the theoretical ROC curves for the Cauchy with $\alpha = 1$ and GG distributions. It is seen from Figure 5.3 that the detectors based on the $S\alpha S$ distribution, and even its Cauchy member, have higher rates of detection for a given probability of false alarm than that based on the GG distribution.

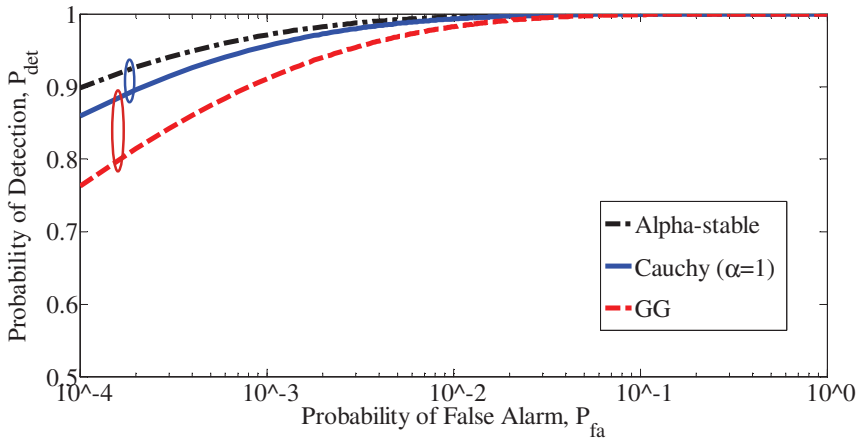


Figure 5.3. ROC curves for the detectors based on alpha-stable, Cauchy and GG distributions.

### 5.2.4 Detector Based on the Bivariate Alpha-Stable Distribution

Using the bivariate $S\alpha S$ and its Cauchy member with $\alpha = 1$, we also obtain the ROC curves. Figure 5.4 shows the corresponding ROC curves for the bivariate and univariate $S\alpha S$, bivariate and univariate Cauchy and GG distributions. It should be noted that for the case of bivariate Cauchy distribution, having the PDF given by $f_\gamma(x_1, x_2) = \dfrac{\gamma}{2\pi(x_1^2 + x_1^2 + \gamma^2)^{3/2}}$, one can obtain the theoretical mean and variance of $\ln(\Lambda_{\text{det}})$ under $H_0$, i.e., $x_i = y_i$, as

$$\mu_0 = E\left[\ln(\Lambda_{\text{det}}) \mid H_0\right] = -\sum_{i=1}^{N} \frac{\ln(1+\xi) + \ln(1-\xi)}{2} + \frac{3}{2}\sum_{i=1}^{N} \left( \ln \left( \frac{\gamma^2 + (x_{i1})^2 + (x_{i2})^2}{\left( \left( \gamma^2 + \left( \frac{x_{i1}}{1+\xi} \right)^2 + (x_{i2})^2 \right) \left( \gamma^2 + (x_{i1})^2 + \left( \frac{x_{i2}}{1-\xi} \right)^2 \right) \right)^{1/2}} \right) \right) \tag{5-27}$$

and

$$\sigma_0^2 = Var\left[\ln(\Lambda_{\text{det}}) \mid H_0\right] = E\left[\ln(\Lambda_{\text{det}}) - E\left[\ln(\Lambda_{\text{det}}) \mid H_0\right]\right]^2 = \sum_{i=1}^{N} \frac{1}{4} \left( \ln \frac{(1+\xi)}{(1-\xi)} + \ln \frac{\gamma^2 + \left( \frac{x_{i1}}{1-\xi} \right)^2 + (x_{i2})^2}{\gamma^2 + \left( \frac{x_{i1}}{1+\xi} \right)^2 + (x_{i2})^2} \right)^2 \tag{5-28}$$

where parameter $\gamma$ of the bivariate Cauchy distribution can be directly computed from the children contourlet coefficients of the watermarked image. To obtain the mean and variance of the log-likelihood ratio, following assumptions have been made. 1) The number of directions in each scale should be the same in order to have a relation between the parents and their children in each direction. 2) The watermark is embedded only in the children subband. To have both $x_{i1}$ and $x_{i2}$ to be of the same size, we expand the parent subband by a factor of 2. It should be noted that the PDF of the original and watermarked images are assumed to be the same, i.e., embedding the watermark does not change the distribution of the original image coefficients [37]. It is seen from Figure 5.4 that the detectors based on the bivariate $S\alpha S$ distribution, and even its Cauchy member, have higher rates of detection for a given probability of false alarm than that based on the GG distribution. We also obtain the CPU times for the detectors based on these distributions; Table 5.1 gives the CPU times averaged over a number of images. It is observed from this table that the CPU time when using the best fit bivariate and univariate $S\alpha S$ is indeed high. Thus, the performance improvement of the bivariate $S\alpha S$ over that using bivariate Cauchy distribution, as seen from Figure 5.4, is at the expense of a substantially high computational complexity. Therefore, without any appreciable loss of the rate of detection, a watermark detector is also designed based on the bivariate Cauchy distribution. It should be noted that the bivariate Cauchy distribution has a closed form expression for its PDF which leads to a computationally efficient detector with low CPU time required.

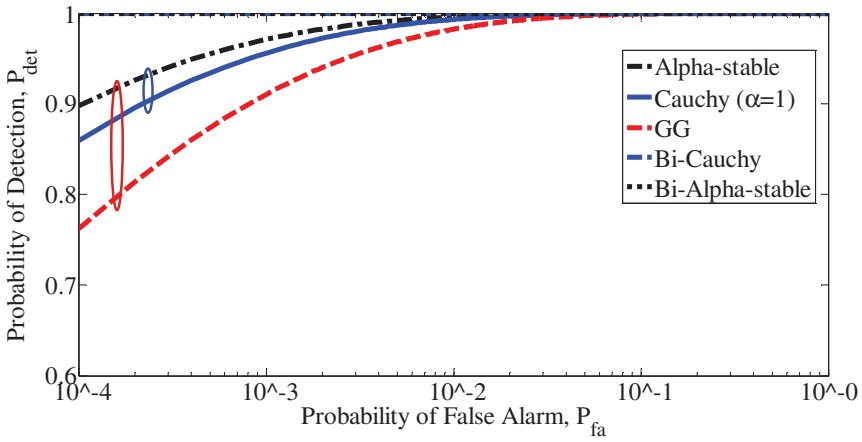


(a)

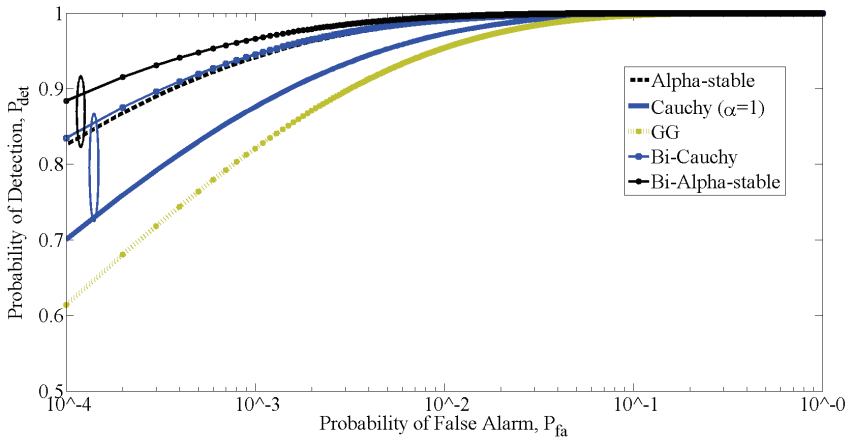


(b)

Figure 5.4. ROC curves for the detectors based on bivariate alpha-stable (bi-alpha-stable), univariate alpha-stable, bivariate Cauchy (bi-Cauchy), Cauchy and GG distributions, (a) WDR= - 38 dB, (b) WDR= - 40 dB.

Table 5.1: The computational complexity of the detectors based on the $S\alpha S$ , Cauchy and GG distributions.

| | Bi-SαS | SαS | Bi-Cauchy | Cauchy | GG |
|---|---|---|---|---|---|
| CPU time(sec) | 60.53 | 43.47 | 3.12 | 1.85 | 1.83 |

## 5.3 Experimental Results

Experiments are conducted to investigate the imperceptibility of the embedded watermark as well as the robustness of the proposed method against attacks. The standard images considered in these experiments are images of size 512×512 [99]. In our experiments, the watermark is generated following the procedure described in 5.2.1. To select the appropriate subband for embedding the watermark bits adopting the multiplicative embedding rule, both the robustness and the visual quality of watermarked image should be considered. In view of this, we embed the watermark through the following procedure.

- Decompose the original image into a number of subbands by using the contourlet transform with two pyramidal levels followed by eight directions in each scale.
- Compute the variance of the intensity of each subband by using (5-3) and choosing the subband that has the highest variance for embedding the watermark.
- By using $y_i = x_i + \xi x_i w_i$, we can embed the watermark in a multiplicative manner.
- Apply the inverse contourlet transform to the modified coefficients to obtain the watermarked image.

In Figures 5.5(a)-(e), a few of the original images namely, *Barbara*, *Peppers*, *Airplane* and *Baboon* are presented and the watermarked images with WDR = - 40 in Figures 5.5 (f)-(j). The images are indistinguishable, thus showing the effectiveness of the multiplicative contourlet-domain watermarking in terms of the invisibility of the watermark. Watermark detection is performed without requiring the use of the original image (i.e., blind image watermarking).

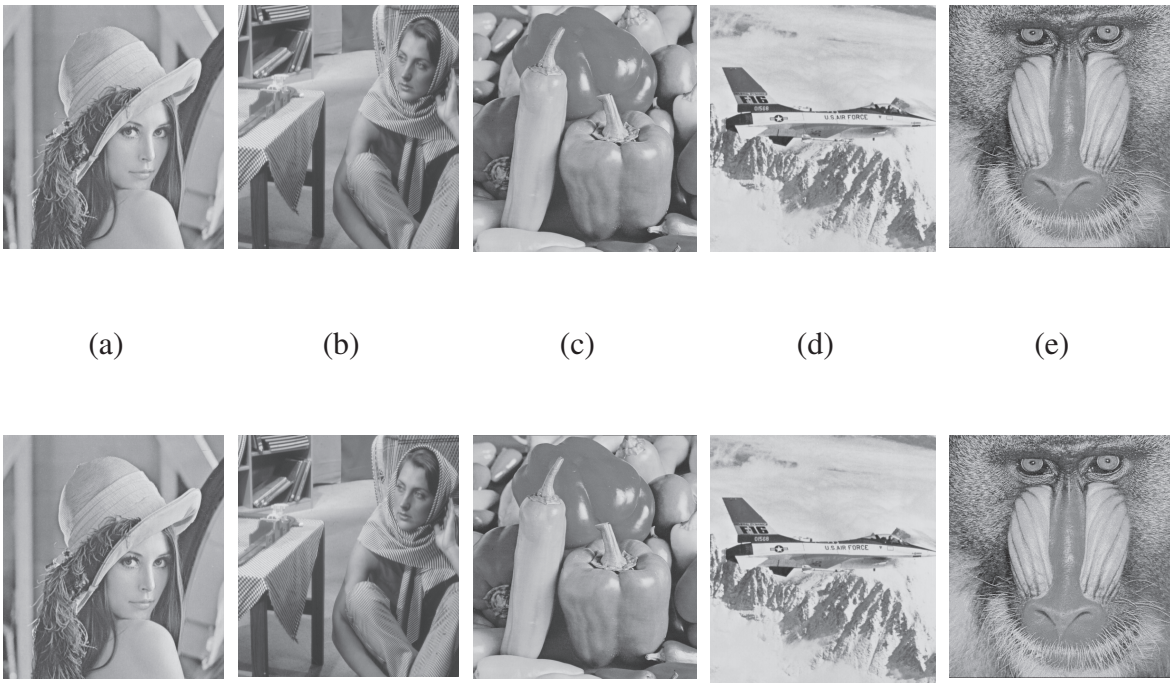

(a) (b) (c) (d) (e)

(f) (g) (h) (i) (j)

Figure 5.5. Original (a-e) and watermarked with WDR = - 40 dB (f-j) images of *Lena* PSNR = 58.42, *Barbara* PSNR = 52.19, *Peppers* PSNR = 60.20, *Airplane* PSNR = 56.85 and *Baboon* PSNR=53.35. No visual difference can be realized.

To compare the performance of the contourlet transform with other sparse transforms such as wavelet, dual-tree complex wavelet and curvelet transforms, we assume a two level of decomposition for each transform and a same-size watermark inserted in the subband coefficients with highest value for their variances. Based on this assumption, the ROC curves for various transforms are derived for the univariate Cauchy and GG distributions. Figure 5.6 depicts the ROC curves obtained for one of the test images, the *Barbara* image. It is seen from this figure that the contourlet and curvelet transforms have the best rates of detection as compared to other transforms. Similar results have been obtained for other test images. The reason for better rates of detection for these two transforms is due to their capability in capturing more geometrical shapes by allowing for a flexible number of directions at each scale [3], [4]. However, the fact that the contourlet transform has been directly defined in the discrete domain and on rectangular grids, resulting in having 2-D frequency partition on concentric rectangles rather than on concentric circles for curvelet, motivated us to use the contourlet transform in our work. Table 5.2 gives the CPU times averaged over a number of images, required by the detectors using the contourlet and curvelet transforms. It is seen from this table that the detector using the contourlet transform has a very much lower computational complexity compared to that using the curvelet transform. The significantly lower CPU time for the contourlet-based method can be attributed to the fact that this transform is not only defined directly in the discrete domain, but also employs iterated filter banks making it computationally efficient.

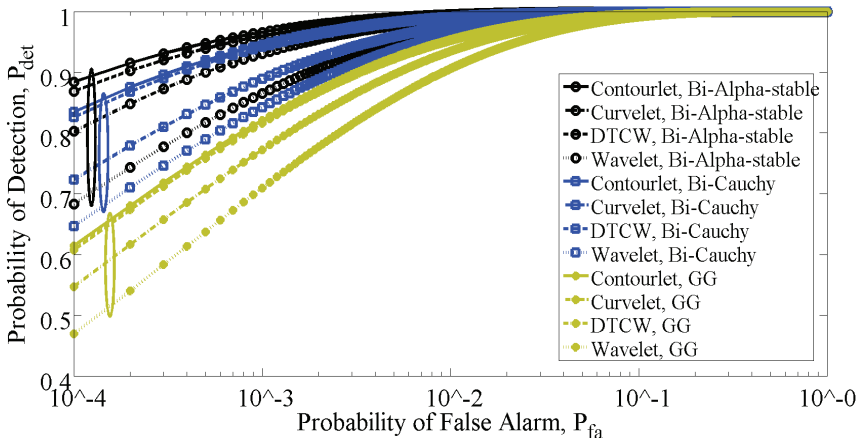


Figure 5.6. ROC curves for the detectors using contourlet, curvelet, wavelet and dual-tree complex wavelet (DTCW) transforms.

Table 5.2: The computational complexity of the detectors based on the univariate Cauchy distribution using the contourlet and curvelet transforms.

| | Contourlet | Curvelet |
|---|---|---|
| CPU time(sec) | 1.85 | 213.90 |

Now, for each image, the performance of the bivariate Cauchy detector is first compared to that of the GG detector in terms of the ROC curves without any kind of attack. It is to be pointed out that the theoretical ROC can be computed directly from the data by estimating the parameters for each of the two distributions. To validate this theoretical ROC, Monte Carlo simulations are performed. The experimental mean and variance of $\ln(\Lambda_{det})$ for each of the detectors are estimated. The theoretical and experimental ROC curves are shown in Figure 5.7 for the bivariate Cauchy and GG detectors. It is seen from this figure that the experimental ROC curves are very close to the theoretical ones for both the detectors. It is also seen that the bivariate Cauchy detector yields a performance better than that of the GG detector as evidenced by a higher probability of detection for any given value of false alarm.

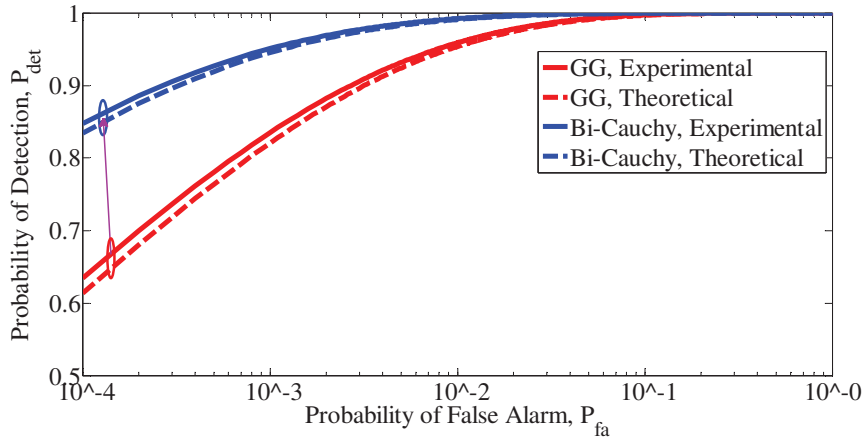


Figure 5.7. Theoretical and experimental ROC curves for the bivariate Cauchy and GG detectors.

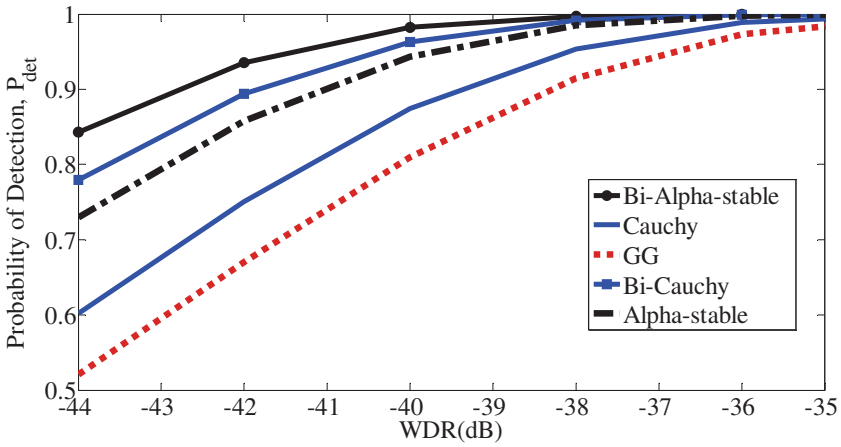


Figure 5.8. Probability of detection for watermarks of varying strength parametrized by the WDR (dB) for various detectors.

In order to compare the performance of the detectors for watermarks with different strengths, we consider WDR in the range - 42 dB to - 32 dB for all the test images. Figure 5.8 shows the results of detection rate when $P_{fa}$ is fixed at $10^{-3}$. From this figure, it can be seen that as WDR decreases, the performance of both the schemes deteriorates. However, the bivariate $S\alpha S$ and bivariate Cauchy detectors outperform the GG detector at any level of watermark strength, as can be seen from the values of the detection probabilities. Figure 5.9 shows the probability of false alarm $P_{fa}$ as a function of the strength of the watermark, WDR, for a fixed value of the probability of detection $P_{\text{det}} = 0.9$. It is seen from this figure that the probability of false alarm for the proposed bivariate $S\alpha S$ and bivariate Cauchy detectors are lower than that of the GG detector for different watermark strengths. The robustness of the detectors against the various attacks is next studied using the same test images.

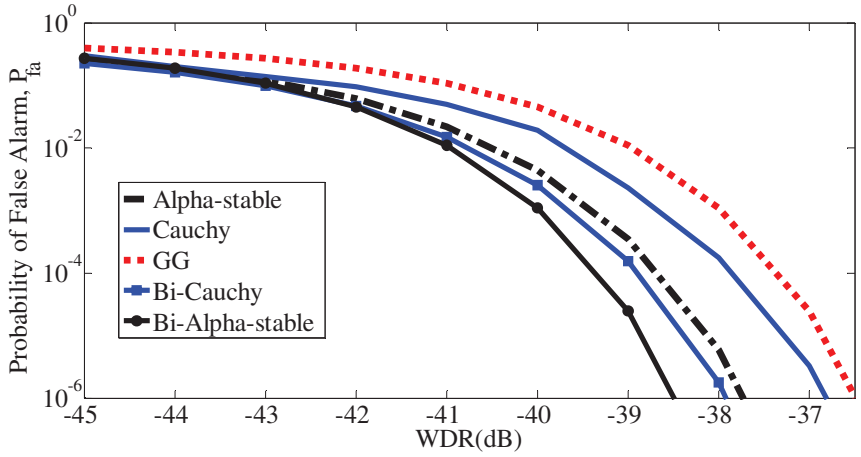


Figure 5.9. Probability of false alarm for watermarks of varying strength parametrized by WDR (dB) for various detectors.

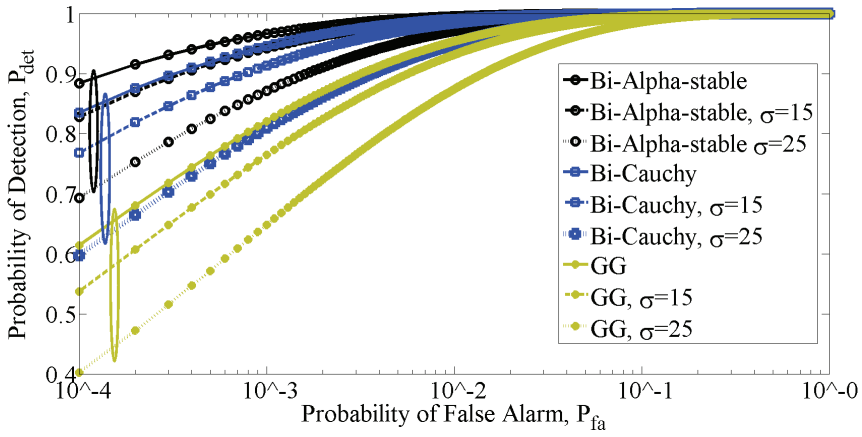


Figure 5.10. ROC curves for various detectors when the AWGN with various standard deviations is added to the watermarked images.

To study the robustness against noise, the watermarked images are corrupted by AWGN with $\sigma$ varying from 0 to 25. Figure 5.10 shows the averaged ROC curves obtained using various detectors when the watermarked image is contaminated by AWGN attack. It is seen from this figure that the proposed bivariate $S\alpha S$ and bivariate Cauchy detectors are more robust than GG detector is.

The robustness of the proposed detector under JPEG compression is now investigated. For this purpose, we compare the log-likelihood ratio $\ln(\Lambda_{\text{det}})$ with the decision threshold $\tau$ for a given false alarm probability to obtain the detector response for a given image. The detector responses of the proposed watermarking scheme with the bivariate SαS and bivariate and univariate Cauchy detectors as well as that with the GG detector for one of the test images, the *Lena* image, are shown in Figure 5.11. It is seen from this figure that by using the proposed watermarking scheme with the bivariate $S\alpha S$ detector and even its Cauchy member, a higher detection rate is obtained and that the scheme is more robust than the one with the GG detector. Finally, the robustness of the proposed scheme when the watermarked image undergoes median filtering is studied. Figure 5.12 shows the detector responses of the proposed watermarking scheme with the bivariate $S\alpha S$ and bivariate and univariate Cauchy detectors as well as that with the GG detector for the Lena image with windows of size 3×3, 5×5 and 7×7 for the median filter. It is evident from this figure that for the size of 7×7, the GG detector cannot recognize the presence of the watermark. Thus, the proposed scheme using the bivariate $S\alpha S$ and bivariate Cauchy detectors are much more robust than that with GG detector.

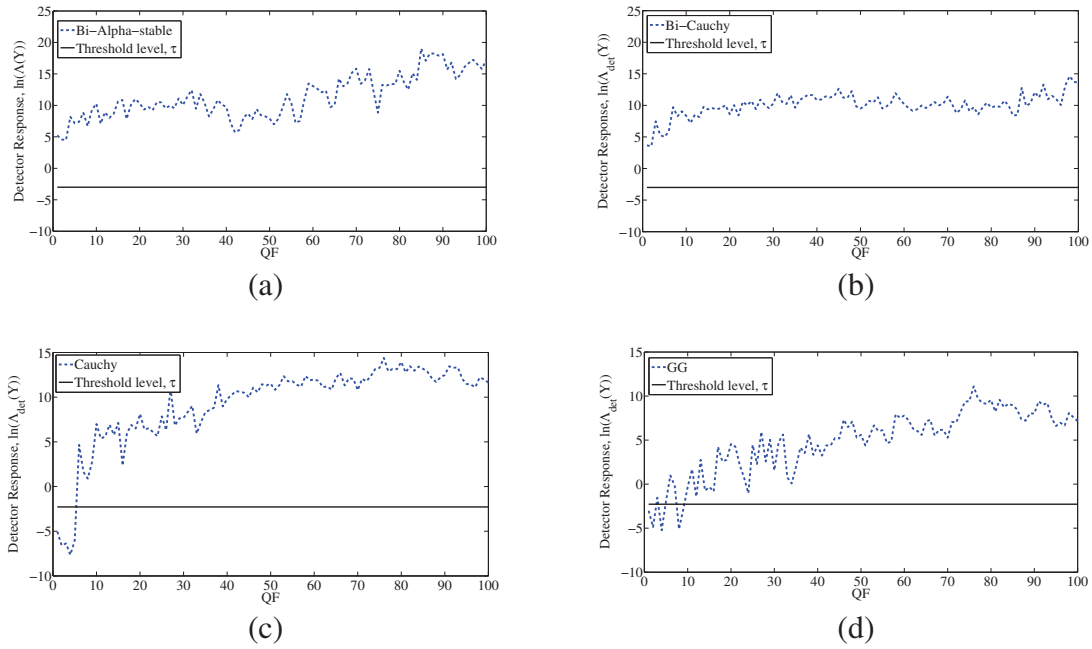


Figure 5.11. Detector response for the (a) bivariate alpha-stable, (b) bivariate Cauchy, (c) univariate Cauchy and (d) GG distributions when the *Lena* image is JPEG-compressed with different quality factors varying from 1 to 100, WDR = - 38 dB.

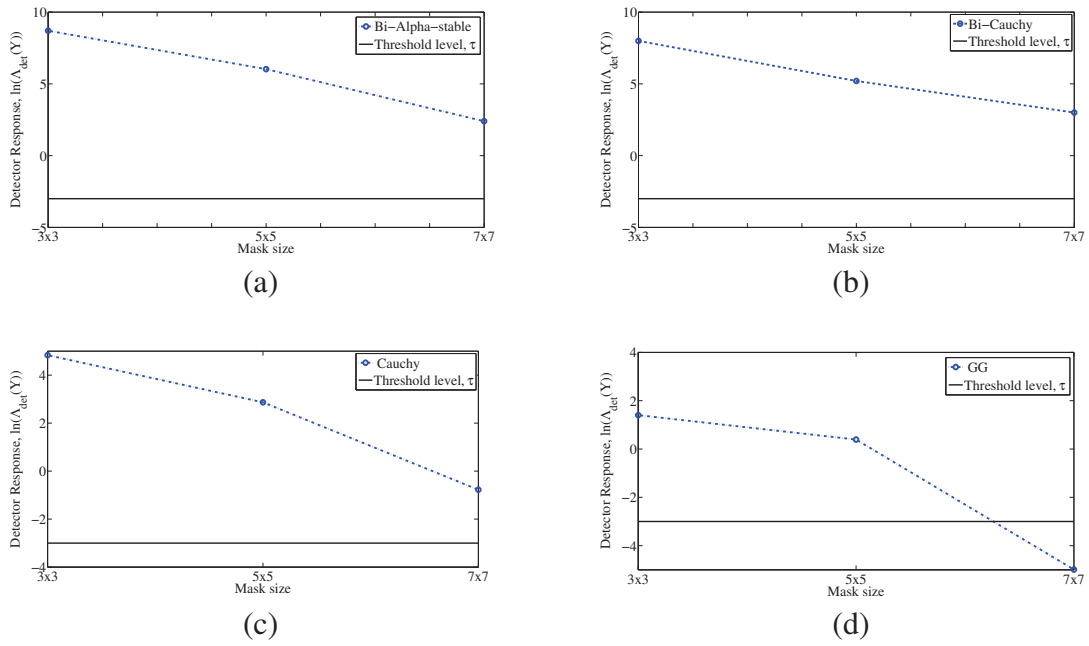


Figure 5.12. Detector response for the (a) bivariate alpha-stable, (b) bivariate Cauchy, (c) univariate Cauchy and (d) GG distributions when the *Lena* image is under median filtering with windows of size of 3×3, 5×5 and 7×7;WDR = - 38 dB.

## 5.4 Summary

In this chapter, blind watermark detectors using the univariate and bivariate alpha-stable distributions have been designed. The proposed detectors employ the Bayesian log-likelihood ratio criterion for the watermark detection. It has been shown that the detectors based on both of these distributions have rates of detection for a given probability of false alarm higher than that of the detector designed based on the GG distribution. Even though the detector based on the best-fit alpha-stable distribution provides a higher detection rate, it is computationally expensive because of the lack of a closed-form expression for its distribution. In view of this, watermark detectors have been designed based on the univariate and bivariate Cauchy members of the alpha-stable family. It has been shown that a very significant advantage of the closed-form expression of the Cauchy PDF is that it allows a derivation of closed-form expressions for the mean and variance of the log-likelihood ratio in terms of the empirical data. This has resulted in the design of significantly reduced-complexity detectors, and yet has provided a performance that is much superior to that of the GG detector and very close to that corresponding to the best-fit alpha detectors. The performance of the proposed detectors have been evaluated in detail by conducting several experiments. The robustness of the proposed detectors against additive white Gaussian noise, JPEG compression and median filtering attacks has been studied and shown to be superior to that of the GG detector. In the next chapter, the problem of watermarking color images will be investigated by taking into account the inter-channel dependencies of the RGB color channels.

# CHAPTER 6

# Multiplicative Watermark Detector for Color Images in the Contourlet Domain

## 6.1 Introduction

Most of the image watermarking schemes have focused on grayscale images [24]-[29]. The generalization of such schemes to color images is feasible by embedding the watermark into the luminance channel in the luminance/chrominance, i.e., YUV, domain or through watermarking each channel separately. However, it has been shown that the dependencies between the RGB channels can remarkably improve the performance of the watermark detection [145]. In [145], a watermarking technique has been proposed in the discrete cosine transform domain in which the dependencies of the RGB channels have been taken into account by defining a global correlation measure. In [146]-[149], the complex and quaternion Fourier transforms have been used to capture the chromatic information of the color images. However, quaternion Fourier transform-based watermarking is computationally inefficient. In [150], a wavelet-based watermarking scheme for color images has been proposed through visual masking in the YUV domain. However, it does not take the color information into account by ignoring the chrominance components. In [151], the histogram bin shifting technique has been used for reversible watermarking of the color images. However, the performance of this algorithm is not satisfactory in the RGB color space. In many watermarking schemes in the transform

domain, a decision rule has been devised as a binary hypothesis test to verify the presence or absence of the hidden information. It has been shown that the effectiveness of a watermark detector depends highly on the modeling of the transform-domain coefficients [13], [24]. In [24], the Weibull density function has been used to model the discrete Fourier transform coefficients of color images. In [152], a multivariate power-exponential (MPE) distribution has been proposed to capture the wavelet subband statistics and dependencies across RGB channels in an additive color image watermarking scheme. However, the detector proposed in [152] is not robust when the watermark is low-powered or the watermarked image is under attack. In this chapter, a multichannel multiplicative watermark detector for color images is proposed [153]. The proposed detector is developed by using the multivariate Cauchy distribution. A Bayesian log-likelihood ratio test is employed to derive an efficient closed-form expression for the test statistics. The performance of the proposed detector is evaluated by obtaining the receiver operating characteristics curves. The robustness of the proposed watermarking scheme is examined when the watermarked images undergo JPEG-compression, salt and pepper noise, median filtering and Gaussian noise attacks.

## 6.2 Watermarking Scheme

To embed the watermark bits, the original RGB color channels are separately decomposed into a number of subbands by using the contourlet transform with highest sparsity among other transforms [4], [13]. It is known that the watermark should be inserted into the significant features of an image in order to increase the robustness of the watermark [154]. In view of this, the directional subband with highest entropy in the

second scale of each channel is chosen for embedding purpose. The contourlet coefficients of the selected subband are modified as

$$\mathbf{y} = \mathbf{x}(1 + \zeta \mathbf{w}) \tag{6-1}$$

where $\mathbf{x} = \lfloor x_1, x_2, x_3 \rfloor$ and $\mathbf{y} = \lfloor y_1, y_2, y_3 \rfloor$ are the original and marked coefficients of RGB channels, $\mathbf{w} = \lfloor w_1, w_2, w_3 \rfloor$ is the watermark of size $N \times 3$ and $\zeta$ is a positive watermark weighing factor. The watermark is generated using a direct sequence spread spectrum technique, wherein the watermark is generated using a pseudorandom sequence generator that has an authentication key as its initial value. This pseudorandom sequence spreads the spectrum of the watermark signal over many coefficients making it difficult to be detected. The watermarked contourlet coefficients are then inverse transformed to obtain the watermarked image.

In order to detect the presence of the watermark in the receiver, the signal statistics is taken into account via modeling the contourlet coefficients of RGB color channels by the multivariate Cauchy distribution. The Cauchy model has been shown to accurately fit the histogram of the contourlet coefficients of images [15]. To design the watermark detector, we employ a Bayesian log-likelihood ratio test which can be reduced to a binary hypothesis test as

$$\begin{aligned} H_0 &: \ \mathbf{y} = \mathbf{x} \quad (not - watermarked) \\ H_1 &: \ \mathbf{y} = \mathbf{x}(1 + \zeta \mathbf{w}) \quad (watermarked) \end{aligned} \tag{6-2}$$

The hypotheses $H_1$ and $H_0$ represent as to whether the contourlet coefficients are watermarked by the sequence $\mathbf{w}$ or do not carry any watermark, respectively. The decision rule is then defined as the log-likelihood ratio given by

$$\Lambda_{\text{det}} = \ln\left(\frac{f_{\mathbf{Y}}(\mathbf{y} \mid H_1)}{f_{\mathbf{Y}}(\mathbf{y} \mid H_0)}\right) \underset{H_0}{\overset{H_1}{\gtrless}} \tau \tag{6-3}$$

where $\tau$ is the decision threshold and

$$\begin{aligned} f_{\mathbf{Y}}(\mathbf{y} \mid H_0) &= f_{X_1, X_2, X_3}(y_1, y_2, y_3) \\ f_{\mathbf{Y}}(\mathbf{y} \mid H_0) &= \frac{f_{X_1, X_2, X_3}\left(\frac{y_1}{1+\zeta w_1}, \frac{y_2}{1+\zeta w_2}, \frac{y_3}{1+\zeta w_3}\right)}{(1+\zeta w_1)(1+\zeta w_2)(1+\zeta w_3)} \end{aligned} \tag{6-4}$$

The detector is supposed to choose between $H_1$ and $H_0$ based on the received image coefficients $\mathbf{y}$. Then, by assuming the independence of the observations, the log-likelihood ratio becomes

$$\Lambda_{\text{det}} = \sum_{i=1}^{N} \ln\left(\frac{P\left(\frac{y_{1i}}{1+\zeta w_1}, \frac{y_{2i}}{1+\zeta w_2}, \frac{y_{3i}}{1+\zeta w_3}\right)}{(1+\zeta w_1)(1+\zeta w_2)(1+\zeta w_3) P(y_{1i}, y_{2i}, y_{3i})}\right) \tag{6-5}$$

To take into account the information carried out by all the three color channels, the data $\mathbf{x}$ is modeled by the multivariate Cauchy distribution given by

$$f_{\mathbf{X}}(\mathbf{x}:n,\Sigma)=\frac{\Gamma(\frac{n+1}{2})}{\Gamma(\frac{1}{2})\pi^{1/2}\,|\Sigma|^{1/2}\left[1+\mathbf{x}^T\Sigma^{-1}\mathbf{x}\right]^{\frac{n+1}{2}}} \tag{6-6}$$

where $\Gamma(.)$ is the gamma function and $\Sigma$ is the covariance matrix of size $n\times n$. Thus, the log-likelihood ratio for the multivariate Cauchy distribution is obtained as

$$\Lambda_{\text{det}}=\sum_{i=1}^{N}\ln\left(\frac{1+\mathbf{y}_i^T\Sigma^{-1}\mathbf{y}_i}{1+\mathbf{z}_i^T\Sigma^{-1}\mathbf{z}_i}\right)^2+\sum_{i=1}^{N}\ln\left|\frac{1}{(1+\zeta w_{1i})(1+\zeta w_{2i})(1+\zeta w_{3i})}\right| \tag{6-7}$$

where

$$\mathbf{z}=\left[\frac{y_1}{1+\zeta\, w_1},\frac{y_2}{1+\zeta\, w_2},\frac{y_3}{1+\zeta\, w_3}\right] \tag{6-8}$$

The log-likelihood ratio can be seen as a superposition of $N$ statistically independent random variables. Thus, according to the central limit theorem, the log-likelihood ratio follows a Gaussian distribution under each hypothesis. The mean and variance of each of the Gaussian distributions can be estimated from the empirical data and are given by $(\mu_0,\mu_1)$ and $(\sigma_0^2,\sigma_1^2)$ for $H_0$ and $H_1$, respectively. Having (6-7), the theoretical mean and variance of $\Lambda_{\text{det}}$ under $H_0$ can be obtained as follows:

Let $\Lambda_{\text{det}}=g_1(y)+g_2(y)$, where

$$g_1(y)=\ln\left|(1+\zeta\, w_1)(1+\zeta\, w_2)(1+\zeta\, w_3)\right| \tag{6-9}$$

and

$$g_2(y) = \ln\left(\frac{1+\mathbf{y}^T\Sigma^{-1}\mathbf{y}}{1+\mathbf{z}^T\Sigma^{-1}\mathbf{z}}\right)^2 \tag{6-10}$$

The mean and variance of the log-likelihood ratio under $H_0$ can be obtained as

$$\mu_0 = \mu(\ln(\Lambda_{\text{det}}); H_0) = \sum_{i=1}^{N} (\mu_{g_1} + \mu_{g_2}) \tag{6-11}$$

and

$$\sigma_0^2 = \sigma^2(\ln(\Lambda_{\text{det}}); H_0) = \sum_{i=1}^{N} \left(\sigma_{g_1}^2 + \sigma_{g_2}^2 - 2\mu_{g_1 g_2} + 2\mu_{g_1}\mu_{g_2}\right) \tag{6-12}$$

We assume that the watermark sequence $w_1 = w_2 = w_3$ where is generated by a pseudorandom sequence taking values +1 and -1 with equal probability. Hence, $\mu_{g_1}$ and $\mu_{g_2}$ can be obtained as

$$\mu_{g_1} = \frac{-3}{2}\left(\ln(1+\zeta) + \ln(1-\zeta)\right) \tag{6-13}$$

and

$$\mu_{g_2} = \ln\left(\frac{\mathbf{y}^T\Sigma^{-1}\mathbf{y}}{1+\dfrac{\mathbf{y}^T\Sigma^{-1}\mathbf{y}}{(1+\zeta)^2}}\right) + \ln\left(\frac{\mathbf{y}^T\Sigma^{-1}\mathbf{y}}{1+\dfrac{\mathbf{y}^T\Sigma^{-1}\mathbf{y}}{(1-\zeta)^2}}\right) \tag{6-14}$$

Substituting (6-13) and (6-14) in (6-11), and after making some manipulations, the mean of the log-likelihood is obtained as

$$\mu_0 = \frac{-3}{2}\left[\ln(1+\zeta)+\ln(1-\zeta)\right]+\sum_{i=1}^{N}\ln\frac{(1+y_i^T\Sigma^{-1}y_i)^2}{\left(1+\frac{y_i^T\Sigma^{-1}y_i}{(1+\zeta)^2}\right)\left(1+\frac{y_i^T\Sigma^{-1}y_i}{(1-\zeta)^2}\right)} \tag{6-15}$$

In order to find the variance of the log-likelihood ratio under $H_0$, the various terms are found as

$$\sigma_{g_1}^2 = E[g_1^2]-\mu_1^2 = \frac{9}{4}\left(\ln(1+\zeta)+\ln(1-\zeta)\right)^2 \tag{6-16}$$

$$\sigma_{g_2}^2 = E[g_2^2]-\mu_2^2 = \left(\ln\frac{1+\frac{y^T\Sigma^{-1}y}{(1-\zeta)^2}}{1+\frac{y^T\Sigma^{-1}y}{(1+\zeta)^2}}\right)^2 \tag{6-17}$$

$$\mu_{g_1g_2} = -\frac{3}{2}\ln\left(\frac{1+\mathbf{y}^T\Sigma^{-1}\mathbf{y}}{1+\frac{\mathbf{y}^T\Sigma^{-1}\mathbf{y}}{(1+\zeta)^2}}\right)\ln(1+\varsigma)-\frac{3}{2}\ln\left(\frac{1+\mathbf{y}^T\Sigma^{-1}\mathbf{y}}{1+\frac{\mathbf{y}^T\Sigma^{-1}\mathbf{y}}{(1+\zeta)^2}}\right)\ln(1-\varsigma) \tag{6-18}$$

$$\mu_{g_1}\mu_{g_2} = -\frac{3}{2}\left(\ln(1+\varsigma)+\ln(1-\varsigma)\right).\ln\left(\frac{\left(1+\mathbf{y}^T\Sigma^{-1}\mathbf{y}\right)^2}{\left(1+\dfrac{\mathbf{y}^T\Sigma^{-1}\mathbf{y}}{(1+\zeta)^2}\right)\left(1+\dfrac{\mathbf{y}^T\Sigma^{-1}\mathbf{y}}{(1-\zeta)^2}\right)}\right) \tag{6-19}$$

Substituting (6-16) to (6-19) in (6-12), and after some mathematical manipulations, the final expression for the variance if found as

$$\sigma_0^2 = \sum_{i=1}^{N}\left(\frac{3}{2}\ln\frac{1+\zeta}{1-\zeta}+\ln\frac{1+\dfrac{y_i^T\Sigma^{-1}y_i}{(1+\zeta)^2}}{1+\dfrac{y_i^T\Sigma^{-1}y_i}{(1-\zeta)^2}}\right)^2 \tag{6-20}$$

It can be shown that $\mu_1 = -\mu_0$ and $\sigma_1^2 = \sigma_0^2$. Having found the mean and variance of the log-likelihood ratio under both the hypotheses, the probabilities of false alarm and detection can be estimated by

$$P_{\text{det}} = Q\left(\frac{\tau-\mu_1}{\sigma_1}\right)$$
$$P_{fa} = Q\left(\frac{\tau-\mu_0}{\sigma_0}\right) \tag{6-21}$$

The ROC curves are obtained by relating the probability of detection $P_{\text{det}}$ to a predefined probability of false alarm $P_{fa}$ in a Neyman-Pearson sense, given by [144]

$$P_{\text{det}} = Q\left( Q^{-1}(P_{fa}) - \frac{2\mu_1}{\sigma_1} \right) \tag{6-22}$$

In order to estimate the covariance matrix $\Sigma$ from the observation, we resort to the maximum likelihood estimation via the expectation-maximization algorithm proposed in [155].

## 6.3 Experimental Results

Experiments are performed using a set of color images including Kodak and standard, e.g., *Lena* and *Baboon* images, each resized to 256×256 pixels. The RGB color channels are first decomposed using the contourlet transform into two scales and eight directions in each scale. The watermark bits are embedded in each color channel in a multiplicative manner resulting in a higher robustness with respect to single channel [24], [146], or additive watermarking algorithms [153]. In Figure 6.1, some of the original and watermarked *Kodak* images are illustrated. The images are indistinguishable with high PSNR values obtained by averaging over 10 runs with 100 different watermark sequences and a watermark weighting factor $\zeta = 0.5$, thus showing the effectiveness of the proposed scheme in terms of the invisibility of the watermark. In order to show the capability of the proposed watermark detector in detecting the desired watermark among a set of known marks, we obtain the log-likelihood ratio, ln ($\Lambda_{\text{det}}$), for each of the marks and the decision threshold $\tau$ for a given false alarm probability, to obtain the detector response for a given image. Figure 6.2 shows the detector responses as a function of watermark for some of the test images. It is seen from this figure that the proposed

detector can perfectly detect the watermark among 1001 random marks since the log-likelihood ratio is greater than the threshold value. It should be noted that the desired watermark is placed in 500$^{th}$ place, i.e., the authorized user knows the secret key.

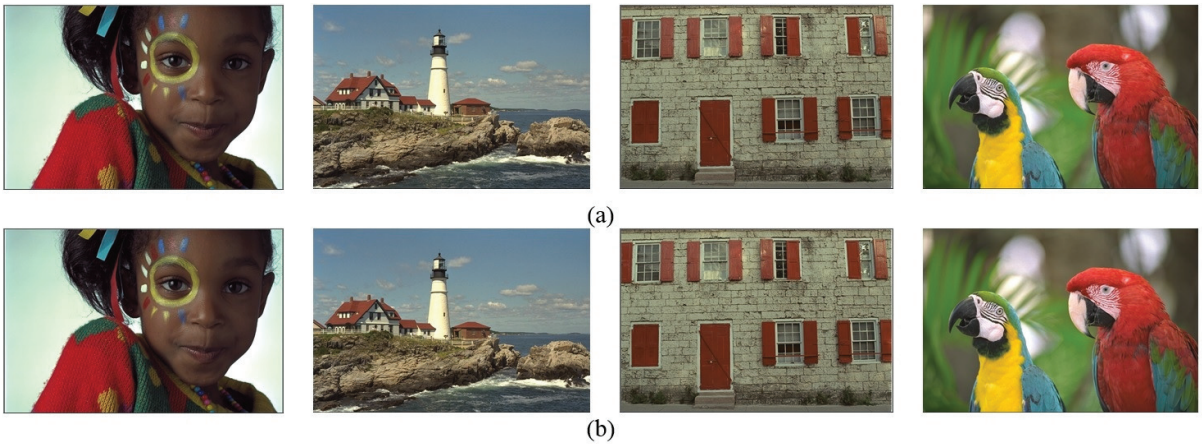


Figure 6.1. (a) Original and (b) watermarked images, from left to right: *Girl*, *Headlight*, *Window* and *Parrots* with PSNR values 68.08, 64.16, 63.45 and 69.57 dB, respectively.

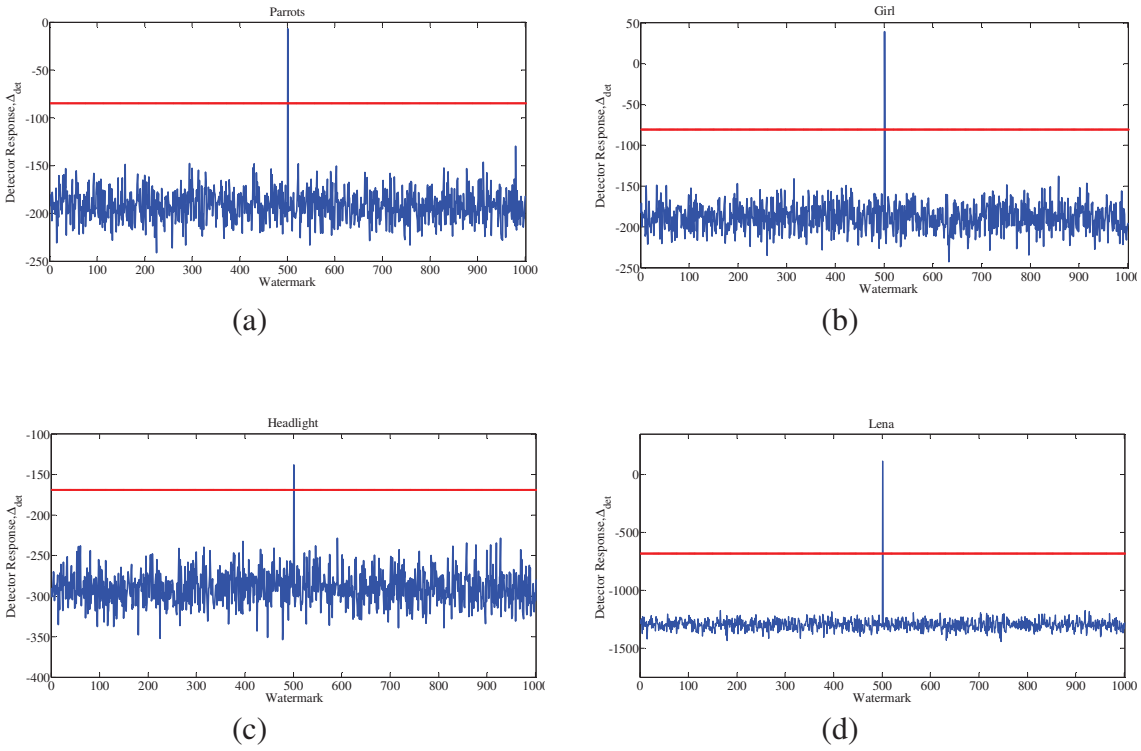


Figure 6.2. Detector response of the proposed watermark detection scheme for some of the test images, namely, (a) *Parrots* (b) *Girl* (c) *Headlight* and (d) *Lena*.

In order to evaluate the performance of the proposed watermark detector, we examine the closeness of the theoretical and experimental ROC curves for the proposed detector. The experimental results are obtained by using a Monte Carlo simulation with 1000 randomly generated watermark sequences. Figure 6.3 shows the experimental and theoretical ROC curves averaged over a set of color images. It is seen from this figure that the theoretical ROC curves are close to the empirical ones indicating the accuracy of the closed-form expressions in (6-15) and (6-20) for the mean and variance of the log-likelihood ratio.

We then compare the detection performance of the proposed blind watermark detector to that of the RGB-joint correlator [146], luminance-GG/Cauchy [24] and RGB-MPE [152]. Figure 6.4 shows the ROC curves of various detectors averaged over a set of color images. It is seen from this figure that the proposed multiplicative watermark detector yields a performance which is substantially better than that of the other detectors as evidenced by a higher probability of detection for any given value of false alarm probability. It is also seen that the proposed multiplicative watermark detector provides a 15% gain over its additive counterpart. The performance of the proposed watermark detector against some of the commonly-used attacks, namely, JPEG compression, AWGN, median filtering, Gaussian filtering and salt and pepper noise are then examined.

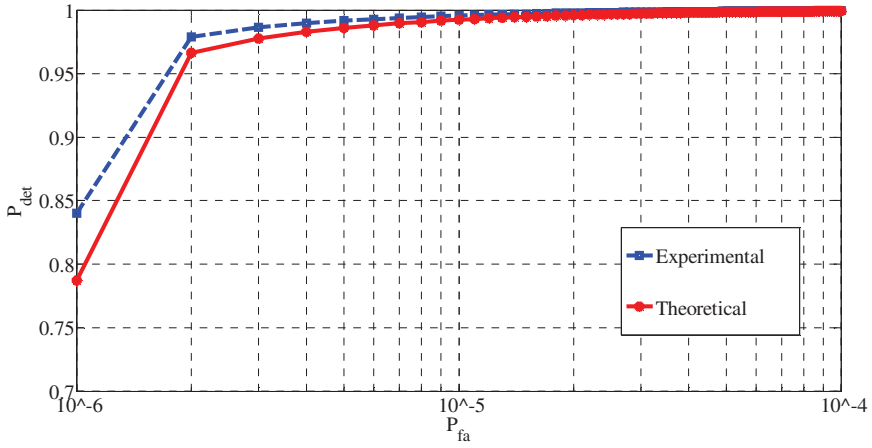


Figure 6.3. Experimental (dashed) and theoretical (solid) ROC curves averaged over a set of color images obtained using the proposed detector.

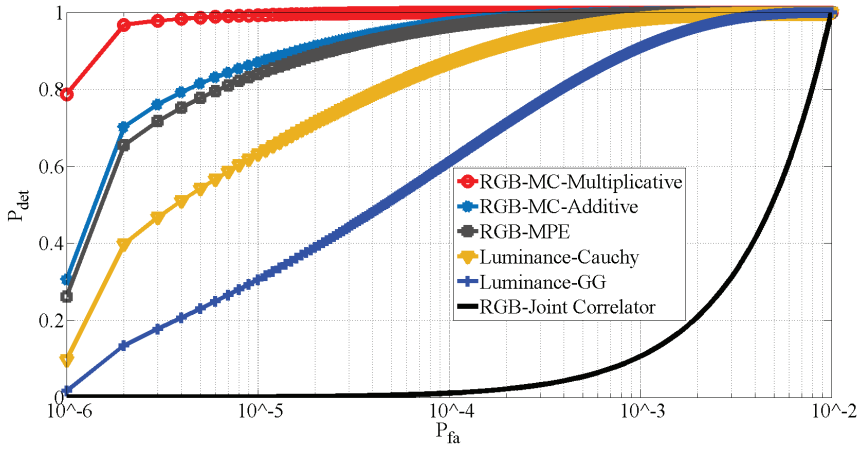


Figure 6.4. ROC curve obtained using the proposed detector (multiplicative and additive) as well as that of the RGB-joint correlator, luminance-GG/Cauchy and RGB-MPE.

Figure 6.5 shows the ROC curves obtained using the proposed watermark detector averaged over a set of color images when the watermarked images are JPEG-compressed with quality factor (QF) = 5, 15 and 35. From this figure, it can be seen that the proposed detector is highly robust against JPEG compression attack. More specifically, the detector is capable of detecting the presence of the watermark with the highest possible detection rate for a given $P_{fa}$ when QF > 35.

To study the robustness against noise, the watermarked images are corrupted by AWGN with standard derivation $\sigma_\eta$ varying from 0 to 40. Figure 6.6 shows the averaged ROC curves obtained using the proposed detector when the watermarked images are contaminated by Gaussian noise. It is seen from this figure that the proposed detector is highly robust against AWGN even under high-strength noise, i.e., $\sigma_\eta = 40$.

Figure 6.7 shows the ROC curves obtained using the proposed watermark detector averaged over a set of color images when the watermarked images are under median filter with mask of sizes 3×3, 5×5 and 7×7. From this figure, it is seen that the proposed detector is highly robust against median filter attack. Figure 6.8 shows the ROC curves averaged over a set of images when the watermarked images are filtered by the Gaussian filters with mask sizes of 3×3, 5×5 and 7×7. It is seen from this figure that the proposed detector is highly robust against Gaussian filtering.

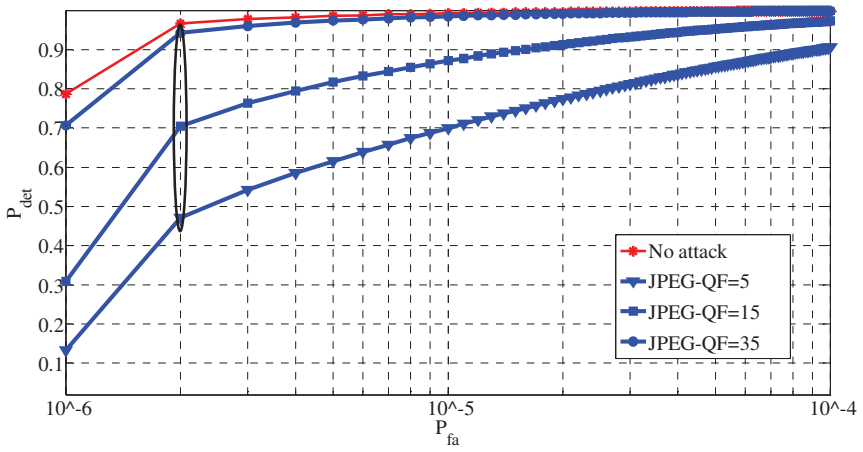


Figure 6.5. ROC curves obtained using the proposed detector averaged over a set of color images when the watermarked images are JPEG-compressed with various QFs.

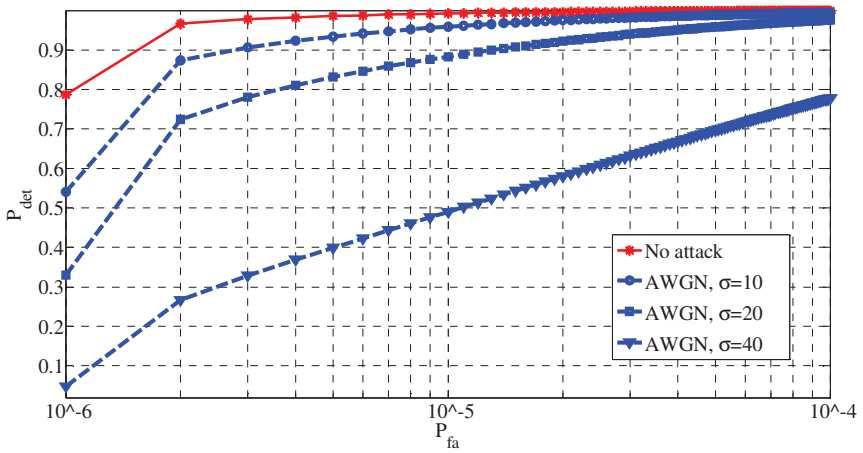


Figure 6.6. ROC curves obtained using the proposed detector averaged over a set of color images when Gaussian noise with various $\sigma_\eta$ is added to the watermarked images.

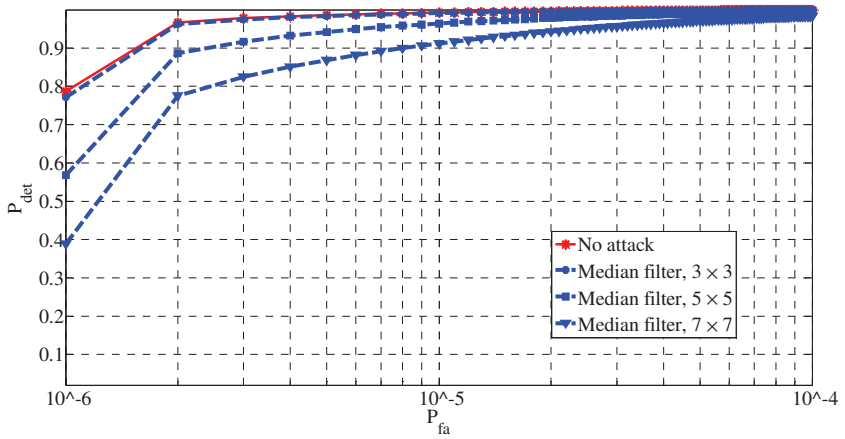


Figure 6.7. ROC curves obtained using the proposed detector averaged over a set of color images when the watermarked images are under median filter with different mask sizes.

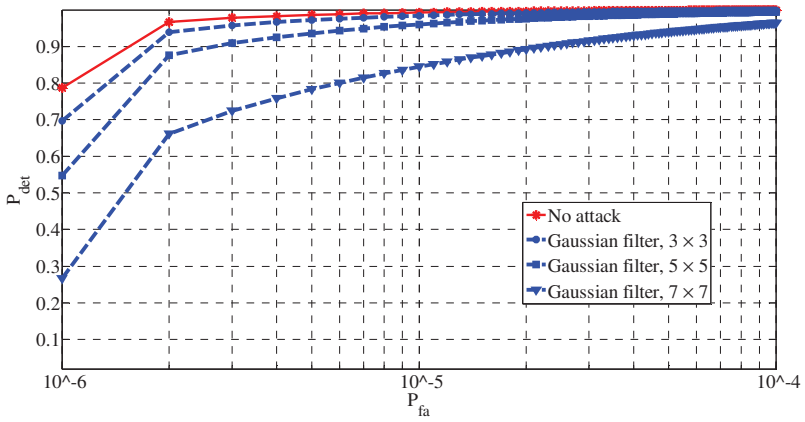


Figure 6.8. ROC curves obtained using the proposed detector averaged over a set of color images when the watermarked images are under Gaussian filter with various mask sizes.

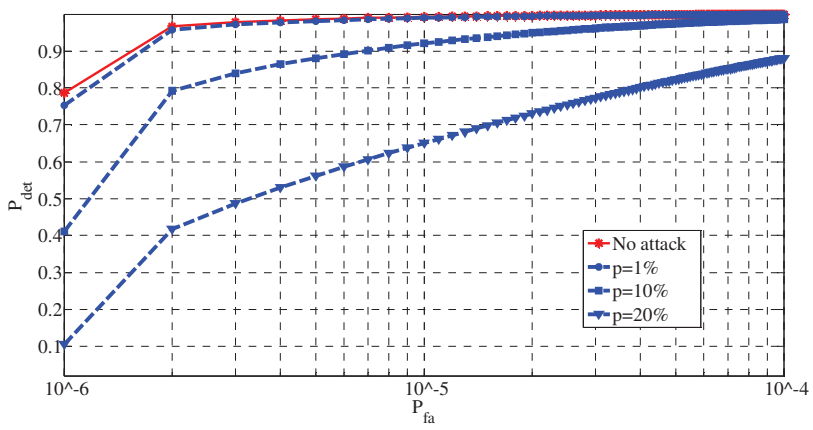


Figure 6.9. ROC curves obtained using the proposed detector averaged over a set of color images when the watermarked images are under salt and pepper noise with various probability of noisy pixels. *p* denotes the percentage of corrupted pixels.

Figure 6.9 shows the ROC curves averaged over a set of images when the watermarked images are contaminated by the salt and pepper noise attack with equal probability. It is seen from this figure that the proposed watermark detector is robust against salt and pepper noise especially when the noise levels are less than 10 %.

In terms of complexity, the proposed multiplicative detector is computationally efficient, since it requires 0.89 and 7.42 seconds CPU time for the lightweight, i.e., with predefined parameters, and regular versions averaged over a set of images on an Intel Core *i7* 2.93 GHz personal computer with 8 GB RAM.

## 6.4 Summary

In this chapter, a blind multichannel multiplicative watermark detector in contourlet domain for watermarking of color images has been proposed. To efficiently exploit the statistical dependencies between the color channels in designing the watermark detector, the contourlet domain coefficients of the channels have been modeled by the multivariate Cauchy distribution. By employing this model, the statistical watermark detector has been designed through the Bayesian log-likelihood ratio test and closed-form expressions for the mean and variance of the log-likelihood ratio have been derived. Experiments have been carried out using standard color images to evaluate the performance of the proposed watermark detector. It has been shown that the performance of the proposed multiplicative watermark detector for color images is substantially superior to that of the other detectors in providing a higher detection rate. It has also been shown that the proposed detector is highly robust against JPEG compression, salt and pepper noise, median filtering, Gaussian filtering and Gaussian noise attacks.

# CHAPTER 7

# Conclusion

## 7.1 Concluding Remarks

This thesis has been concerned with the statistical modeling of images in the contourlet domain and in developing detection and estimation techniques using these models for applications in image denoising and watermarking. The modeling of images in the contourlet domain has been first investigated. It has been shown that the distributions of the contourlet subband coefficients of natural images are highly non-Gaussian. The suitability of different non-Gaussian distributions to model the contourlet coefficients has been comprehensively studied. It has been shown that the alpha-stable distribution is more accurate in modeling the contourlet coefficients of images than other distributions are.

Motivated by the capability of the alpha-stable family of distributions in modeling the contourlet coefficients of images, new image denoising methods in the contourlet domain for grayscale and color images have been designed. Bayesian minimum mean absolute error and maximum *a posteriori* estimators have been developed using the alpha-stable family of distributions to estimate the noise-free contourlet coefficients. Extensive experiments have been conducted using a wide variety of natural images from a number of image databases. It has been shown that the denoising scheme based on the alpha-stable distribution outperforms the other existing methods in terms of the peak

signal-to-noise ratio and mean structural similarity index, as well as in terms of visual quality of the denoised images.

The univariate and bivariate alpha-stable distributions, including its Cauchy member, have been used in designing blind multiplicative watermark detectors for grayscale images. The proposed detectors have been designed based on the Bayesian log-likelihood ratio criterion for the watermark detection. The performance of the detectors designed have been evaluated through extensive experiments. It has been shown that the detectors based on these distributions have rates of detection for a given probability of false alarm higher than that of the other detectors. The robustness of the proposed detectors against various attacks has been studied and shown to be superior to that of the other detectors. A blind multichannel multiplicative watermark detector in the contourlet domain for watermarking of color images has also been proposed. In order to efficiently exploit the statistical dependencies of the color channels in designing the watermark detector, the contourlet domain coefficients of the channels have been modeled by the multivariate Cauchy distribution. By employing this model, the statistical watermark detector has been designed based on the Bayesian log-likelihood ratio test and closed-form expressions for the mean and variance of the log-likelihood ratio have been derived. It has been shown that the performance of the proposed multiplicative watermark detector for color images is substantially superior to that of the other detectors in providing a higher detection rate for both with and without attacks on the watermarked images.

## 7.2 Contributions

Multiscale representation of images is almost indispensable to image processing tasks. Contourlet transform provides an efficient representation of images with smooth contours. This representation not only has the multiscale and time-frequency localization features of the wavelet transform, but it also offers higher degrees of directionality and sparseness and recognizes the smoothness of the image contours. In almost all applications, an effective and accurate modeling of the underlying signals in the original domain or in a transformed domain is a prerequisite. The success of an image denoising or watermarking scheme greatly depends on the use of a statistical model of the image that can accurately capture its characteristics and inter- and intra-scale dependencies using a small number of parameters so that the model can be used as a prior information in such a task. This thesis has investigated the modeling problem of the contourlet coefficients from the standpoint of image denoising and watermarking and has proposed a number of novel and efficient denoising and watermarking algorithms. In a nutshell, the contributions of the investigation undertaken can be described as follows.

1. A comprehensive study has been undertaken for the modeling of the contourlet coefficients of images [15], [89], [132]. It has been established that the empirical distributions of images can be characterized by the heavy-tailed alpha-stable family of the distributions. Through this study, it has been shown that a univariate member of this family can accurately fit the marginal distributions of the empirical data and that a bivariate member can accurately characterize the inter-scale dependencies of the image contourlet coefficients.

2. The alpha-stable models for contourlet coefficients have been used to design new Bayesian maximum *a posteriori* and minimum mean absolute error estimators for the denoising of grayscale and color images [64], [89]. The effectiveness of the denoising schemes developed can be attributed to the use of the univariate alpha-stable distribution in capturing the statistical behavior of the contourlet subband coefficients, the use of the bivariate distribution in capturing the across-scale dependencies, and the use of trivariate alpha-stable distribution in capturing the cross-correlations between the RGB color channels. A new scheme has also been proposed for despeckling of SAR images by modeling the contourlet coefficients of the log-transformed SAR images using the symmetric alpha-stable distribution in a Bayesian MAP estimation framework [129].
3. New multiplicative blind watermark detectors for grayscale images using the univariate and bivariate alpha-stable distributions in the framework of the Bayesian log-likelihood ratio criterion with closed-form expressions for the mean and variance of the log-likelihood ratio have been designed [132]. A multichannel multiplicative watermark detector for color images using multivariate Cauchy distribution in the framework of Bayesian log-likelihood ratio test with an efficient closed-form expression for the test statistics has also been proposed [153]. It has been established that the use of the Cauchy distribution leads to significantly reduced-complexity detectors and provides a performance that is much superior to that using other distributions.

## 7.3 Scope for Future Work

While the research work undertaken in this thesis has focused on developing efficient and cost-effective techniques for various estimators and detectors, there are a number of additional studies that can be undertaken along the ideas developed in this thesis. Some of the possible studies are as follows:

- The proposed image denoising scheme in this thesis can be applied to video frames in intra-coding mode, wherein, the alpha-stable family of distributions can capture the high dependency of the contourlet coefficients of the neighboring frames.
- Short video clips are being shared widely on the Internet. In order to protect video contents and to verify the ownership, one can employ the proposed watermarking schemes for video contents in intra-coding mode. In this scheme, the motion compensation vectors may be modelled by using the proposed alpha-stable family of distributions for detecting the existing watermark.
- The multivariate alpha-stable distribution may be used in developing estimation and detection algorithms to take into account the inter-scale, intra-scale and inter-orientation dependencies of the contourlet coefficients of images.

# REFERENCES


[1] C. Gonzalez and E. Woods, *Digital Image Processing*. 3rd Ed, Prentice Hall, 2008.

[2] M. Vetterli and J. Kovacevic, *Wavelets and Subband Coding*. Englewood Cliffs, NJ: Prentice-Hall, 1995.

[3] M. N. Do, "*Directional multiresolution image representations*," Ph.D. dissertation, School Comput. Commun. Sci., Swiss Fed. Inst. Technol, 2001.

[4] M. N. Do and M. Vetterli, "The contourlet transform: an efficient directional multiresolution image representation," *IEEE Transactions on Image Processing*, vol.14, no.12, pp. 2091-2106, Dec 2005.

[5] I. W. Selesnick, R. Baraniuk and N. Kingsbury, "The dual-tree complex wavelet transform," *IEEE Signal Processing Magazine*, vol. 22, no. 6, pp. 123-156, Nov 2005.

[6] E. J. Candes and D. L. Donoho, "Ridgelets: A key to higher-dimensional intermittency?," *Philosophical Transactions on Royal Society of London A*, vol. 357, no. 1760, pp. 2495-2509, Sep 1999.

[7] E. J. Candes and D. L. Donoho, "Curvelets- a surprisingly effective non-adaptive representation for objects with edges," in *Curve and Surface Fitting*, C. R. A. Cohen and L. Schumaker, Eds. Nashville, TN: Vanderbilt Univ. Press, 2000.

[8] J. L. Starck, E. J. Candes, and D. L. Donoho, "The curvelet transform for image denoising," *IEEE Transactions on Image Processing*, vol. 11, no. 6, pp. 670-684, June 2002.

[9] E. J. Candes and D. L. Donoho, "New tight frames of curvelets and optimal representations of objects with piecewise $C^2$ singularities," *Communications on Pure and Applied Mathematics,* pp. 219-266, Nov 2003.

[10] A. Srivastava, A. B. Lee, E. P. Simoncelli and S.-C. Zhu, "On advances in statistical modeling of natural images," *Journal of Mathematical Imaging and Vision*, vol. 18, no. 1, pp. 17-33, Jan 2003.

[11] R. Eslami and H. Radha, "The contourlet transform for image denoising using cycle spinning," in *Proc. IEEE Asilomar Conference on Signals, Systems, and Computers*, pp. 1982-1986, Nov 2003.

[12] Sh. Xiao, W. Kai and G. Qiang, "Local thresholding with adaptive window shrinkage in the contourlet domain for image denoising," *Information Science*, vol. 56, no. 9, pp. 1-9, Sep 2013.

[13] A. Akhaee, S. M. Sahraeian, and F. Marvasti, "Contourlet-based image watermarking using optimum detector in noisy environment," *IEEE Transactions on Image Processing*, vol. 19, no. 4, pp. 700-715, Apr 2010.

[14] P. Niu, X. Wang, Y. Yang and M. Lu, "A novel color image watermarking scheme in nonsampled sontourlet domain," *Expert Systems with applications*, vol. 38, no. 3, pp. 2081-2098, Mar 2011.

[15] H. Sadreazami, M. Omair Ahmad and M. N. S. Swamy, "Contourlet domain image modeling by using the alpha-stable family of distributions," in *Proc. IEEE International Symposium on Circuits and Systems (ISCAS),* pp. 1288-1291, June 2014.

[16] S. G. Chang, B. Yu, and M. Vetterli, "Spatially adaptive wavelet thresholding with context modeling for image denoising," *IEEE Transactions on Image Processing*, vol. 9, pp. 1522-1531, Sep 2000.

[17] J. Portilla, V. Strela, M. Wainwright and E. P. Simoncelli, "Image denoising using scale mixtures of Gaussians in the wavelet domain," *IEEE Transactions on Image Processing*, vol. 11, pp. 1338-1351, Nov 2003.

[18] L. Sendur and I. W. Selesnick, "Bivariate shrinkage with local variance estimation," *IEEE Signal Processing Letters*, vol. 9, pp. 438-441, Dec 2002.

[19] M. S. Crouse, R. D. Nowak, and R. G. Baraniuk, "Wavelet-based signal processing using hidden Markov models," *IEEE Transactions on Signal Processing*, vol. 46, pp. 886-902, Apr 1998.

[20] J. M. Fadili and L. Boubchir, "Analytical form for a Bayesian wavelet estimator of images using the Bessel K form densities," *IEEE Transactions on Image Processing*, vol. 14, pp. 231-240, Feb 2005.

[21] L. Sendur and I. W. Selesnick, "Bivariate shrinkage functions for wavelet-based denoising exploiting interscale dependency," *IEEE Transactions on Signal Processing*, vol. 50, pp. 2744-2756, Nov 2002.

[22] V. Doncel, N. Nikolaidis, and I. Pitas, "An optimal detector structure for the Fourier descriptors domain watermarking of 2-D vector graphics," *IEEE Transactions on Visualization and Computer Graphics*, vol. 13, no. 5, pp. 851-863, Sep-Oct 2007.

[23] Q. Cheng and T. S. Huang, "Optimum detection and decoding of multiplicative watermarks in DFT domain," in *Proc. IEEE International Conference on Acoustics, Speech, Signal Processing (ICASSP)*, pp. IV-3477-IV-3480, May 2002.

[24] J. R. Hernández, M. Amado, and F. P. González, "DCT-domain watermarking techniques for still images: Detector performance analysis and a new structure," *IEEE Transactions on Image Processing*, vol. 9, no. 1, pp. 55-68, Jan 2000.

[25] A. Briassouli, P. Tsakalides, and A. Stouraitis, "Hidden message in heavy-tails: DCT-domain watermark detection using alpha-stable models," *IEEE Transactions on Multimedia*, vol. 7, no. 4, pp. 700-715, Aug 2005.

[26] A. Nikolaidis and I. Pitas, "Asymptotically optimal detection for additive watermarking in DCT and DWT domains," *IEEE Transactions on Image Processing*, vol. 12, no. 5, pp. 563-571, May 2003.

[27] M. M. Rahman, M. O. Ahmad, and M. N. S. Swamy, "A new statistical detector for DWT-based additive image watermarking using the Gauss-Hermite Expansion," *IEEE Transactions on Image Processing*, vol. 18, no. 8, pp. 1782-1796, Aug 2009.

[28] T. M. Ng. and H. K. Garg, "Maximum- likelihood detection in DWT domain image watermarking using Laplacian modeling," *IEEE Signal Processing Letters*, vol. 12, no. 4, pp. 285-288, Apr 2005.

[29] M. Barni, F. Bartolini, and A. Piva, "Improved wavelet-based watermarking through pixel-wise masking," *IEEE Transactions on Image Processing*, vol. 10, no. 5, pp. 783-791, May 2001.

[30] B. C. Mohan, and S. S. Kumar, "Robust digital watermarking scheme using contourlet transform", *Journal of Computer Science and Network Security*, vol. 40, no. 2, pp. 43-51, Feb 2008.

[31] M. Jayalakshmi, S. N. Merchant, and U. B. Desai, "Digital watermarking in contourlet domain," in *Proc. IEEE International Conference on Pattern Recognition (ICPR)*, pp. 861-864, 2006.

[32] C. V. Narasimhulu and K. S. Prasad, "A hybrid watermarking scheme using contourlet transform and singular value decomposition," *International Journal of Computer Science and Network Security, (IJCSNS)*, vol. 10, no. 9, Sep 2010.

[33] H. Song, S. Yu, and C. Wang, "Contourlet-based Image adaptive watermarking," *Signal Processing, Image Communication*, vol. 23, pp. 162-178, Mar 2008.

[34] S. Ghannam and F. Abou-Chadi, "Enhancing robustness of digital image watermarks using contourlet transform", in *Proc. IEEE International Conference on Image Processing (ICIP)*, pp. 3645-3648, Nov 2009.

[35] M. Jayalakshmi, S. N. Merchant, and U. B. Desai, "Blind watermarking in contourlet domain with improved detection," in *Proc. IEEE International Conference on Intelligent Information Hiding and Multimedia Signal Processing,* pp. 449-452*,* Dec 2006.

[36] A. K. Mairgiotis, G. Chantas, and Y. Yang, "New detectors for watermarks with unknown power based on Student-t image priors," in *Proc. IEEE International Workshop on Multimedia Signal Processing*, pp. 353-356, Oct 2007.

[37] Q. Cheng and T. S. Huang, "Robust optimum detection of transform domain multiplicative watermarks," *IEEE Transactions on Signal Processing*, vol. 51, no. 4, pp. 906-924, Apr 2003.

[38] H. Qu, and Y. Peng, "Contourlet coefficient modeling with generalized Gaussian distribution and application" in *Proc. IEEE International Conference on Audio, Language and Image Processing (ICALIP)*, pp. 531-535, July 2008.

[39] E. P. Simoncelli, W. T. Freeman, E. H. Adelson, and D. J. Heeger, "Shiftable multiscale transforms," *IEEE Transactions on Information Theory*, vol. 38, no. 2, pp. 587-607, Mar 1992.

[40] F. G. Meyer and R. R. Coifman, "Brushlets: A tool for directional image analysis and image compression," *Journal of Applied Computational Harmonic Analysis*, vol. 5, pp. 147-187, 1997.

[41] D. D.-Y. Po and M. N. Do, "Directional multiscale modeling of images using the contourlet transform," *IEEE Transactions on Image Processing*, vol. 15, no. 6, pp. 1610-1620, June 2006.

[42] M. Allili, N. Baaziz and M. Mejri, " Texture modeling using contourlets and finite mixtures of generalized Gaussian distributions and applications, *IEEE Transactions on Multimedia*, vol. 16, no. 3, pp. 772-784, Apr 2014.

[43] Q. Guo, F. Dong, S. Sun, B. Lei and B. Gao, "Image denoising algorithm based on contourlet transform for optical coherence tomography heart tube image," *IET Image Processing*, vol. 7, no. 5, July 2013.

[44] P. J. Burt and E. H. Adelson, "The Laplacian pyramid as a compact image code," *IEEE Transactions on Communications*, vol. 31, no. 4, pp. 532 -540, Apr 1983.

[45] M. N. Do and M. Vetterli, "Framing pyramids," *IEEE Transactions on Signal Process*ing, vol. 51 no. 9, pp. 2329-2342, Sep 2003.

[46] R. H. Bamberger and M. J. T. Smith, "A filter bank for the directional decomposition of images: Theory and design," *IEEE Transactions on Signal Processing,* vol. 40, no. 4, pp. 882-893, Apr 1992.

[47] S. Park, M. J. T. Smith, and R. M. Mersereau, "Improved structures of maximally decimated directional filter banks for spatial image analysis," *IEEE Transactions on Image Process*ing, vol. 13, no. 11, pp. 1424-1431, Nov 2004.

[48] A. B. Watson, "The cortex transform: Rapid computation of simulated neural images," *Computer Vision, Graphics, and Image Processing*, vol. 39, no. 3, pp. 311-327, 1987.

[49] A. Papoulis, *Probability, Random Variables, and Stochastic Processes*. New York: McGraw-Hill, 1991.

[50] [Online]. Available: http://decsai.ugr.es/cvg/dbimagenes/index.php.

[51] R. Prasad, H. Saruwatari, and K. Shikano, "Estimation of shape parameter of GGD Function by Negentropy Matching," *Neural Processing Letters* , vol. 22, no. 3, pp. 377-389, Dec 2005.

[52] B. Aiazzi, L. Alparone, and S. Baronti, "Estimation based on entropy matching for generalized Gaussian PDF modeling," *IEEE Signal Processing Letters*, vol. 6, no. 6, pp.138-140, June 1999.

[53] R. Krupinski and J. Purczynski, "Approximated fast estimator for the shape parameter of generalized Gaussian distribution," *Signal Processing*, vol. 86, no. 2, pp. 205-211, Feb 2006.

[54] M. Varanasi, and B. Aazhang, "Parametric generalized Gaussian density estimation," *Journal of Acoustical Society of America*, vol. 86, no. 4, pp. 1404-1415, Oct 1989.

[55] K. Sharifi, and A. Leon Garcia, "Estimation of shape parameter for generalized Gaussian distributions in subband decompositions of video," *IEEE Transactions on Circuits and Systems for Video Technology*, vol. 5, no. 1, pp. 52-56, Feb 1995.

[56] M. Pi, "Improve maximum likelihood estimation for subband GGD parameters", *Pattern Recognition Letters*, vol. 27, no. 14, pp. 1710-1713, Oct 2006.

[57] C. Nikias and M. Shao, *Signal Processing With Alpha-Stable Distributions and Applications*. New York: Wiley, 1995.

[58] W. H. Du Mouchel, "*Stable Distributions in Statistical Inference*," Ph.D. dissertation, Dept. Statist. Yale Univ., New Haven, CT, 1971.

[59] R. Adler, R. Feldman and M. Taqqu, *A Guide to Heavy Tails; Statistical Techniques ad Applications*. Boston, MA: Birkhauser, 1998.

[60] F. Fama and R. Roll, "Parameter estimates for symmetric stable distribution," *Journal of the American Statistical Association,* vol. 66, pp. 331-338, June 1971.

[61] B. Brorsen and S. Yang, "Maximum likelihood estimates of symmetric stable distribution parameters," *Communications in Statists-Simulation and Computation,* vol. 19, pp. 1459-1464, 1990.

[62] J. Nolan, "*Maximum likelihood Estimation and Diagnostics for stable distributions*," dissertation, Dept. Math. Statist. American Univ., Tech. Rep., 1999.

[63] S. Mittnik, S. Rachev and T. Doganoglu, "Maximum likelihood estimation of stable paretian models," *Mathematical and Computer Modeling*, vol. 29, pp. 275-293, May-June 1999.

[64] H. Sadreazami, M. Omair Ahmad and M. N. S. Swamy, "Contourlet domain image denoising using the alpha-stable distribution," in *Proc. IEEE International Midwest Symposium on Circuits and Systems (MWSCAS),* pp. 141-144, Aug 2014.

[65] I. Koutrouvelis, "Regression-Type Estimation of the Parameters of Stable Laws," *Journal of American Statistical Association,* vol. 75, pp. 918-928, Dec 1980.

[66] J. Ilow and D. Hatzinakos, "Applications of the empirical characteristic function to estimation and detection problems," *International Journal of Signal Processing,* vol. 65, pp. 199-219, Mar 1988.

[67] J. H. McCulloch, "Simple consistent estimators of stable distribution parameters," *Communications in Statistics*, *Simulation and Computation*, vol. 15, no. 4, pp. 1109-1136, 1986.

[68] S. M. Koyon and D. B. Williams, "On the characterization of impulsive noise with alpha-stable distributions using Fourier techniques," in *Proc. IEEE Asilomar Conference on Signals, Systems and Computers*, pp. 787-791, Oct-Nov 1995.

[69] Z. Sun and Ch. Han, "Parameter estimation of positive alpha-stable distribution based on negative-order moments*,"* in *Proc. IEEE International conference on Acoustics, Speech and Signal processing (ICASSP)*, pp. 1409-1412, Apr 2007.

[70] A. Achim, C. Canagarajah and D. Bull, "Complex wavelet domain image fusion based on fractional lower order moments,*"* in *Proc. IEEE International conference on Information Fusion (ICIF)*, pp. 515-521, July 2005.

[71] D. L. Donoho, "Denoising by soft thresholding," *IEEE Transactions on Information Theory*, vol. 41 no. 3, pp. 613-627, May 1995.

[72] D. L. Donoho and I. M. Johnstone, "Ideal spatial adaptation by wavelet shrinkage," *Biometrika*, vol. 81, no. 3, pp. 425-455, 1994.

[73] L. Zhang, W. Dong, D. Zhang, and G. Shi, "Two-stage image denoising by principal component analysis with local pixel grouping," *Pattern Recognition*, vol. 43, no. 4, pp. 1531-1549, Apr 2010.

[74] M. Elad and M. Aharon, "Image denoising via sparse and redundant representations over learned dictionaries," *IEEE Transactions on Image Processing*, vol. 15, pp. 3736-3745, Dec 2006.

[75] M. Yin, W. liu, X. Zhao, Q. Guo and R. Bai, "Image denoising using trivariate prior model in nonsubsampled dual-tree complex contourlet transform domain and non-local means filter in spatial domain," *Optik*, vol. 124, pp. 6896-6904, Dec 2013.

[76] C. Sutour, Ch. A. Deledalle, and J. F. Aujol, "Adaptive regularization of the NL-means: application to image and video denoising," *IEEE Transactions on Image Processing*, vol. 23, no. 8, pp. 3506-3521, Aug 2014.

[77] J. Ren, J. Liu and Z. Guo, "Nonlocal hierarchical dictionary learning using wavelets for image denoising*," IEEE Transactions on Image Processing*, vol. 22, no. 12, pp. 4689-4788, Dec 2013.

[78] J. Mairal, F. Bach, J. Ponce, G. Sapiro, and A. Zisserman, "Nonlocal sparse models for image restoration," in *Proc. IEEE International Conference on Computer Vision (ICCV)*, pp. 2272-2279, Sep-Oct 2009.

[79] R. Yan, L. Shao and Y. Liu, "Context-aware sparse decomposition for image denoising and super-resolution," *IEEE Transactions on Image Processing*, vol. 22, no. 4, pp. 1456-1469, Apr 2013.

[80] X. Zhang, X. Feng and W. Wang, "Two-direction nonlocal model for image denoising," *IEEE Transactions on Image Processing*, vol. 22, no.1, pp. 408-412, Jan 2013.

[81] W. Dong, L. Zhang, G. Shi, and X. Li, "Nonlocally centralized sparse representation for image restoration," *IEEE Transactions on Image Processing*, vol. 22, no. 4, pp. 1620-1630, Apr 2013.

[82] K. Dabov, A. Foi, V. Katkovnik, and K. Egiazarian, "Image denoising by sparse 3-D transform-domain collaborative filtering," *IEEE Transactions on Image Processing*, vol. 16, no. 8, pp. 2080-2095, Aug 2007.

[83] P. Chatterjee and P. Milanfar, "Patch-based near-optimal image denoising," *IEEE Transactions on Image Processing*, vol. 21, no. 4, pp. 1635-1649, Apr 2012.

[84] W. Dong, G. Shi, and X. Li, "Nonlocal image restoration with bilateral variance estimation: A low-rank approach," *IEEE Transactions on Image Processing*, vol. 22, no. 2, pp. 700-711, Feb 2013.

[85] A. Fathi and A. Naghsh-Nilchi, "Efficient image denoising method based on a new adaptive wavelet packet thresholding function," *IEEE Transactions on Image Processing*, vol. 21, no. 9, pp. 3981-3990, Sep 2012.

[86] J. Yang, Y. Wang, W. Xu and Q. Dai, "Image and video denoising using adaptive dual-tree discrete wavelet packets," *IEEE Transactions on Circuits and Systems for Video Technology*, vol. 19, no. 5, pp. 642-655, May 2009.

[87] A. A. Bharath and J. Ng, "A steerable complex wavelet construction and its application to image denoising," *IEEE Transactions on Image Processing*, vol. 14, no. 7, pp. 948-959, July 2005.

[88] H. Sadreazami, M. Omair Ahmad and M. N. S. Swamy, "Image denoising utilizing the scale-dependency in the contourlet domain," in *Proc. IEEE International Symposium on Circuits and Systems (ISCAS),* pp. 2149-2152, May 2015.

[89] H. Sadreazami, M. Omair Ahmad and M. N. S. Swamy, "A study on image denoising in contourlet domain using the alpha-stable family of distributions," *Signal Processing, 2016.*

[90] R. R. Coifman and D. L. Donoho, "Translation-invariant denoising," *Lecture Notes in Statistics*, vol. 103, pp. 125-150, 1995.

[91] J. Ilow, "*Signal processing in alpha-stable noise environments: noise modeling, detection and estimation*," PhD Thesis, University of Toronto, 1995.

[92] Z. Sun and Ch. Han, "Parameter estimation of positive alpha-stable distribution based on negative-order moments," in *Proc. IEEE International Conference on Acoustics, Speech and Signal Processing (ICASSP)*, pp. 1409-1412, Apr 2007.

[93] J. Nolan, "*Maximum likelihood Estimation and Diagnostics for stable distributions*," dissertation, Dept. Math. Statist. American Univ., Tech. Rep., 1999.

[94] [Online]. Available: http://academic2.american.edu/_jpnolan/stable/stable.html.

[95] E. E. Kuruoglu, "*Signal processing in alpha-stable noise environments: a least $L_p$-norm approach*," PhD Thesis, University of Cambridge, 1998.

[96] G. Samorodnitsky and M. S. Taqqu, "*Stable Non-Gaussian Random Processes: Stochastic Models with infinite variance*," New York: Chapman and Hall, 1994.

[97] G. Tsihrintzis and C. L. Nikias, "Fast estimation of the parameters of alpha-stable impulsive interference," *IEEE Transactions on Signal Processing*, vol. 44, no. 6, pp. 1492-1503, June 1996.

[98] [Online]. Available: http://bows2.ec-lille.fr/

[99] [Online]. Available: http://sipi.usc.edu/database/

[100] F. Luisier, T. Blu and M. Unser, "A new SURE approach to image denoising: interscale orthonormal wavelet thresholding," *IEEE Transactions on Image Processing*, vol. 16, pp. 593-606, Mar 2007.

[101] D. Cho and T. Bui, "Multivariate statistical approach for image denoising," in *Proc. IEEE International Conference on Acoustics, Speech and Signal Proc. (ICASSP)*, pp. 589-592, Apr 2005.

[102] D. L. Donoho and I. M. Johnstone, "Adaptating to unknown smoothness via wavelet shrinkage," *Journal of the American Statistical Association*, vol. 90, no. 432, pp. 1200-1224, 1995.

[103] Y. Rakvongthai, A. Vo and S. Oraintara, "Complex Gaussian scale mixtures of complex wavelet coefficients," *IEEE Transactions on Signal Processing*, vol. 58, no. 7, pp. 3545-3556, July 2010.

[104] A. L. DaCunha, Z. Jianping and M. N. Do, "The nonsubsampled contourlet transform: theory, design, and applications," *IEEE Transactions on Image Processing*, vol. 15, no. 10, pp. 3089-3101, Oct 2006.

[105] G. Chen, W.-P. Zhu and W. Xie, "Wavelet-based image denoising using three scales of dependency," *IET Image Processing*, vol. 6, no. 6 pp.756-760, Aug 2012.

[106] Y. Shi, X. Yang and Y. Guo, "Translation invariant directional framelet transform combined with Gabor filters for image denoising," *IEEE Transactions on Image Processing*, vol. 23, no. 1, pp. 44-55, Jan 2014.

[107] M. K. Mihcak, I. Kozintsev, K. Ramachandran and P. Moulin, "Low complexity image denoising based on statistical modeling of wavelet coefficients," *IEEE Signal Processing Letters*, vol. 7, no. 6, pp. 300-303, Dec 1999.

[108] J. Saeedi and M. Moradi, "A new wavelet-based fuzzy single and multi-channel image denoising," *Image and Vision Computing*, vol. 28, no. 12, pp. 1611-1623, Dec 2010.

[109] G. Gao, "Image denoising by non-subsampled shearlet domain multivariate model and its method noise thresholding," *Optik*, vol. 124, pp. 5756-5760, Nov 2013.

[110] H. Om and M. Biswas, "MMSE based map estimation for image denoising," *Optics and Laser Technology*, vol. 57, pp. 252-264, Apr 2014.

[111] C. Knaus and M. Zwicker, "Progressive image denoising," *IEEE Transactions on Image Processing*, vol. 23, no. 7, pp. 3114-3125, Apr 2014.

[112] C. Knaus and M. Zwicker, "Dual-domain image denoising," in *Proc. IEEE International Conference on Image Processing (ICIP)*, pp. 440-444, 2013.

[113] M. Lebrun, A. Buades and J. Morel, "A nonlocal Bayesian image denoising algorithm," *SIAM Journal on Imaging Sciences*, vol. 6, no. 3, pp. 1665-1688, Sep 2013.

[114] D. Zoran and Y. Weiss, "From learning models of natural image patches to whole image restoration," in *Proc. IEEE International Conference on Computer Vision (ICCV)*, pp. 479-486, Nov 2011.

[115] H. Om and M. Biswas, "A generalized image denoising method using neighboring wavelet coefficients," *Signal, Image and Video Processing*, vol. 9, no. 1, pp. 191-200, Jan 2013.

[116] W. Zhou, A. C. Bovik, H. Sheikh, and E. P. Simoncelli, "Image Quality Assessment: From Error Visibility to Structural Similarity," *IEEE Transactions on Image Processing*, vol. 13, no. 4, pp. 600-612, Apr 2004.

[117] A. Pizurica and W. Philips, "Estimating the probability of the presence of a signal of interest in multiresolution single- and multiband image denoising," *IEEE Transactions on Image Processing*, vol. 15, no. 3, pp. 645-665, Mar 2006.

[118] F. Luisier and T. Blu, "SURE-LET multichannel image denoising: Interscale orthonormal wavelet thresholding," *IEEE Transactions on Image Processing*, vol. 17, no. 4, pp. 482-492, Apr 2008.

[119] K. Dabov, A. Foi, V. Katkovnik, and K. Egiazarian, "Color image denoising via sparse 3D collaborative filtering with grouping constraint in luminance-chrominance space," *in Proc. IEEE International Conference on Image Processing (ICIP)*, pp. 313-316, Sep-Oct 2007.

[120] C. Oliver and S. Quegan, *Understanding Synthetic Aperture Radar Images*, Artech House, Boston, MA, 1998.

[121] Y. Bian, "Polarimetric SAR statistical analysis using alpha-stable distribution and its application in optimal despeckling," *International Journal of Remote Sensing*, vol. 34, no. 19, 6796-6836, June 2013.

[122] A. Achim, E. Kuruoglu, and J. Zerubia, "SAR image filtering based on the heavy tailed Rayleigh model," *IEEE Transactions on Image Processing*, vol. 15, no. 9, pp. 2686-2693, Sep 2006.

[123] M. I. H. Bhuiyan, M. Omair Ahmad, and M. N. S. Swamy, "Spatially adaptive wavelet based method using the Cauchy prior for denoising the SAR images," *IEEE Transactions on Circuits and Systems for Video Technology*, vol. 17, no. 4, pp. 500-507, Apr 2007.

[124] J. J. Ranjani and S. J. Thiruvengadam, "Dual-tree complex wavelet transform based SAR despeckling using interscale dependence," *IEEE Transactions on Geoscience and Remote Sensing*, vol. 48, no. 6, pp. 386- 397, June 2010.

[125] F. Argenti, T. Bianchi, A. Lapini, and L. Alparone, "Fast MAP despeckling based on Laplacian-Gaussian modeling of wavelet coefficients," *IEEE Transactions on Geoscience and Remote Sensing*, vol. 9, no. 1, pp. 13-17, Jan 2012.

[126] F. Argenti, T. Bianchi, and L. Alparone. "Multiresolution MAP despeckling of SAR images based on locally adaptive generalized Gaussian PDF modeling," *IEEE Transactions on Image Processing*, vol. 15, no. 11, pp. 3385-3399, Nov 2006.

[127] Q. Sun, L. Jiao and B. Hou, "Synthetic aperture radar image despeckling via spatially adaptive shrinkage in the nonsubsampled contourlet transform domain," *Journal of Electronic Imaging*, vol. 17, no. 1, pp. 1-13, Mar 2008.

[128] J. Sveinsson and J. Benedikisson, "Combined wavelet and contourlet denoising of SAR images," in *Proc. IEEE International Geoscience and Remote Sensing Symposium (IGARSS)*, pp. 1150-1153, 2008.

[129] H. Sadreazami, M. Omair Ahmad and M. N. S. Swamy, "Despeckling of the SAR images in the contourlet domain using alpha-Stable distribution," in *Proc. IEEE International Symposium on Circuits & Systems (ISCAS),* pp. 121-124, May 2015.

[130] F. Argenti, T. Bianchi, and L. Alparone, "SAR image despeckling in the undecimated contourlet domain: a comparison of LMMSE and MAP approaches," in *Proc. IEEE Inter. Geoscience and Remote Sensing Symposium (IGARSS)*, pp. 225-228, July 2008.

[131] [Online]. Available: NASA/JPL website (http://airsar.jpl.nasa.gov)

[132] H. Sadreazami, M. Omair Ahmad and M. N. S. Swamy, "A study of multiplicative watermark detection in the contourlet domain using alpha-stable distributions," *IEEE Transactions on Image Processing,* vol. 23, no. 10, pp. 4348-4360, Oct 2014.

[133] I. G. Karybaliand and K. Berberidis, "Efficient spatial image watermarking via new perceptual masking and blind detection schemes," *IEEE Transactions on Information Forensics and Security*, vol. 1, no. 2, pp. 256-274, June 2006.

[134] I. J. Cox, J. Kilian, F. Leighton, and T. Shamoon, "Secure spread spectrum watermarking for multimedia," *IEEE Transactions on Image Processing*, vol. 6, no. 12, pp. 1673-1687, Dec 1997.

[135] Q. Cheng and T. S. Huang, "An additive approach to transform-domain information hiding and optimum detection structure," *IEEE Transactions on Multimedia*, vol. 3, no.3, pp. 273-284, Sep 2001.

[136] A. Mairgiotis, N. Galatsanos, and Y. Yang, "New additive watermark detectors based on a hierarchical spatially adaptive image model," *IEEE Transactions on Information Forensics and Security*, vol. 3, no. 1, pp. 29-37, Mar 2008.

[137] M. Barni, F. Bartolini, A. De Rosa and A. Piva, "Optimum decoding and detection of multiplicative watermarks," *IEEE Transactions on Signal Processing*, vol. 51, no. 4, pp. 1118-1123, Apr 2003.

[138] M. Barni, F. Bartolini, A. De Rosa, and A. Piva, "A new decoder for the optimum recovery of non-additive watermarks," *IEEE Transactions on Image Processing*, vol. 10, no. 5, pp. 755-766, May 2001.

[139] B. Chen and G. Wornell, "Quantization index modulation: A class of provably good methods for digital watermarking and information embedding," *IEEE Transactions on Information Forensics and Security*, vol. 47, no. 4, pp. 1423-1443, May 2001.

[140] Y. Kim, O. Kwon, and R. Park, "Wavelet based watermarking method for digital images using the human visual system," *Electronic Letters*, vol. 35, no. 6, pp. 466-468, Mar 1999.

[141] H. Sadreazami and M. Amini, "A robust spread spectrum based image watermarking in ridgelet domain," *International Journal of Electronics and Communications*, vol. 66, no. 5, pp. 364-371, May 2012.

[142] C. Deng, H. Zhu, and S. Wang, "Curvelet domain watermark detection using alpha-stable models," in *Proc. IEEE International Conference on Information Assurance Security (ICIAS)*, pp. 313-316, Aug 2009.

[143] H. V. Poor*, An Introduction to Signal Detection and Estimation*, 2nd ed. New York: Springer-Verlag, 1994.

[144] S. M. Kay*, Fundamentals of Statistical Signal Processing, Volume II: Detection Theory*, 1st ed. Englewood Cliffs, NJ: Prentice-Hall, 1998.

[145] M. Barni, F. Bartolini and A. Piva, "Multichannel watermarking of color images," *IEEE Transactions on Circuits and Systems for Video Technology*, vol. 12, no. 3, pp. 142-156, Mar 2002.

[146] T. Tsui, X. Zhang and D. Androutsos, "Color image watermarking using multidimensional Fourier transforms," *IEEE Transactions on Information Forensics and Security*, vol. 3, no. 1, pp. 16-28, Mar 2008.

[147] X. Wang, Ch. Wang, H. Yang and P. Niu, "A robust blind color image watermarking in quaternion Fourier transform domain," *Journal of Systems and Software*, vol. 86, pp. 255-277, Feb 2013.

[148] B. Chen, G. Coatrieux, G. Chen, X. Sun, J. Coatrieux and H. Shu, "Full 4-D quaternion discrete Fourier transform based watermarking for color images," *Digital Signal Processing*, vol. 28, pp. 106-119, May 2014.

[149] E. Tsougenis, G. Papakostas and E. Karakasis, "Adaptive color image watermarking by the use of quaternion image Moments," *Expert Systems with Applications*, vol. 41, pp. 6408-6418, Oct 2014.

[150] K. Liu, "Wavelet-based watermarking for color images via visual masking," *International Journal on Electronics and Communications*, vol. 64, pp. 112-124, Feb 2010.

[151] R. Naskar and R. Chakraborty, "Histogram-bin-shifting based reversible watermarking for color images," *IET Image Processing*, vol. 7, no. 2, pp. 99-110, Mar 2013.

[152] R. Kwitt, P. Meerwald, and A. Uhl, "Color-image watermarking using multivariate power-exponential distribution," in *Proc. IEEE International Conference on Image Processing (ICIP)*, pp. 4245-4248, Nov 2009.

[153] H. Sadreazami, M. Omair Ahmad and M. N. S. Swamy, "Multiplicative watermark detector for color images in sparse domain," *IEEE Transactions on Circuits and Systems II: Express Briefs,* vol. 62, no. 12, pp. 1159-1163, Dec 2015.

[154] I. J. Cox, M. L. Miller, and J. A. Bloom*, Digital Watermarking*. San Mateo, CA: Morgan Kaufmann, 2001.

[155] S. Nadarajah and S. Kotz, "Estimation methods for the multivariate t-distribution," *International Journal on Applying Mathematics and Mathematical Applications*, vol. 102, no. 1, pp. 99-118, Feb 2008.